SPIKE TRAIN CHARACTERIZATION AND DECODING FOR NEURAL PROSTHETIC DEVICES

Thesis by

Shiyan Cao

In Partial Fulfillment of the Requirements for the

Degree of

Doctor of Philosophy

CALIFORNIA INSTITUTE OF TECHNOLOGY

Pasadena, California

2003

(Defended July 1, 2003)

ACKNOWLEDGEMENTS

First and foremost, I would like to express my deepest thanks to my advisor, Professor Joel Burdick, whose keen insight as well as great vision in science and engineering continuously provided me with invaluable advice for the work in this thesis. Undoubtedly, none of the results in this thesis would have materialized without his guidance and support. His encouragement and advising style both on and off the research subject made the last five years truly memorable. I cannot thank him enough for all he has done for me

I owe my special thanks to Professor Richard Andersen, whose knowledge and vision make this research project possible. The collaboration with the Andersen Lab in the past five years was absolutely enjoyable as I was surrounded by talented and devoted scientists and researchers. My special thanks also go to Daniella Meeker, with whom I worked closely on this research project, as her recommendation and data make this thesis possible. In addition I thank Krishna Shenoy, Hans Shoelberg, Zoran Nemadic, Chris Buneo, Aaron Batista…Betty, Kelsie…and many others in the Andersen Lab.

I am also grateful to my friends for their help throughout my ups and downs in the past five years. And finally and most importantly, I want to extend my thanks to my parents for their unconditional support, and to Lap, my wife, for everything she has done for me.

This work was funded in part by a grant from the Defense Advanced Research Projects Agency (DARPA) and the National Science Foundation.

ABSTRACT

Neural prosthetic device has the potential of benefiting millions of lock-in and spinal cord injury survivors. One branch of the ongoing research is to construct reach movement based prosthetic devices. An important research topic in this area is to accurately and efficiently extract the essential behavioral and cognitive control signals from the relevant brain area, Parietal Reach Region (PRR). This thesis proposes statistical methods based on applying the Haar wavelet packets to spike trains in order to answer some of the questions in this field.

Although spike train is the most frequently used data in the neural science community, its stochastic properties are not fully understood or characterized. Many applications simply assume it is Poisson by nature. This thesis suggests a formal spike train characterization method using the Haar wavelet packet. The Haar wavelet packet projection coefficients are first generated by projecting the observed spike train ensembles onto the Haar wavelet packet function. Then the ensuing empirical distributions of these coefficients are computed. At the same time, the projection coefficients' distribution of a Poisson process with the same rate function as the observed spike train ensembles are recursively derived. Comparison between the empirical distributions and the hypothesized ones are carried out using a χ^2 test. If the underlying process of the observed spike trains is indeed Poisson in nature, then the two distributions should have good agreement; otherwise, the deviation would be manifested by a large χ^2 variate. Because of the multi-scale property of the wavelet packet, *Poisson-ness* at different scales can be assessed. Moreover, *Poisson Scale-gram* is proposed to help visualize the characteristics of the spike train at different scales. Examples from both surrogate and actual data from PRR are subjected to the test.

Because some neurons display non-Poisson characteristics, simple mean firing rate based decoding technique does not take advantage of all the information embedded in the spike train. It is necessary to extract the relevant features in the context of decoding. The thesis suggests a feature extraction method that searches all the wavelet packet coefficients for the ones with the largest discriminability. The biological relevance of the projection

coefficients is especially appealing to the neural science community. Also in this thesis, discriminability is quantified by mutual information, an information theoretic measure. Because of the tree-like hierarchy of the projection coefficients, the extraction method prunes the tree while scoring each feature with mutual information. It returns the most informative feature(s) in the context of the Bayesian classifier. Decoding performance of this proposed method is compared against the one using mean firing rate only on both surrogate data and the actual data from PRR.

It is also crucial to decode cognitive states because they provide the extra control signals necessary for practical implementation of the prosthetic devices. This thesis proposes a simple finite state machine approach where transition occurs among *baseline*, *plan*, and *go* states. Additionally, an *interpreter* is introduced to interpret the decoding results and to regulate when the transition should occur. Also, different interpretation rules are explored. This thesis demonstrates that the finite state machine framework, when coupled with the *interpreter*, offers a simple autonomous control scheme for the neuron prosthetic system envisioned.

While the neural prosthetic system is in its infancy, many theoretical and experimental works lay the foundation for a bright future in this field. This thesis answers the spike train characterization and decoding questions in a theoretical manner. It offers several novel techniques that bring new ideas and insights into the research field. Moreover, the methods presented here can be extended to accommodate more general problems.

TABLE OF CONTENTS

LIST OF FIGURES AND TABLES

Number *Page*

Chapter 1 Introduction

People's fascination with the brain can be traced back for thousands of years to the time Hippocrates discovered that the brain was involved in sensation and was the source of intelligence. Since then numerous researchers have devoted their careers to unlocking the mystery of the brain: its organization, its functionality, and its operating mechanism. With the advance of physics and electronics in the last century, scientists were able to investigate the brain from its functionality to its microscopic organization. One direct practical result of the explosion of the neuroscience research activities is the development of brain-machine interfaces. Engineers and scientists are using these new scientific discoveries to construct devices that enable the blind to see and the deaf to hear. Another ambitious endeavor is to tap into the thoughts of millions of locked-in patients who are deprived of any motor functions, while their cognitive processing abilities are still functional. With the recent advance of micro-scaled fabrication, probing and recording techniques, reading people's thoughts has become more than just science fiction.

Neural prosthetic systems are invented under the above premises. They are systems that connect the brain to external devices so that the user can operate the device merely by *thinking* about it. Specifically, a neural prosthetic arm system is a system that connects prosthesis directly to motor or pre-motor area of the brain so that thoughts of movement can be used to drive the system. In other words, one can control peripheral devices just by thinking where to reach. Figure 1.1 illustrates an idealized prosthetic system to command arm-reaching motions.

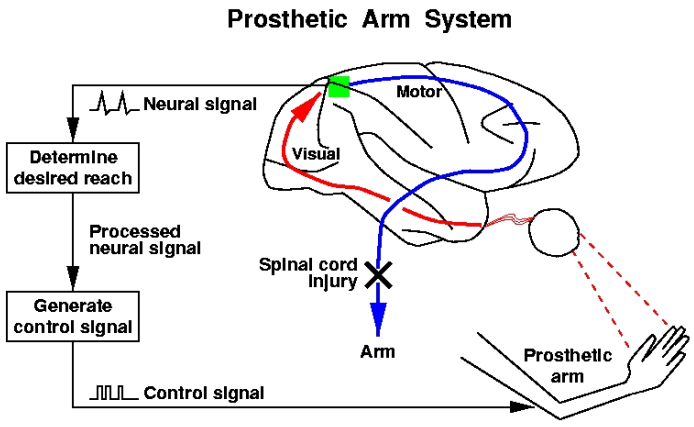

Figure 1-1 Idealized neural prosthetic system

In this figure, a patient with spinal cord injury, or lesion, or motor cortex damage is deprived of any limb movement. However, because the functional area in the brain that plans and commands arm-reaching motions is still intact, a neural prosthetic system can extract the thoughts/intentions from this brain area in order to form control signals. Then the signals are relayed directly to a prosthetic arm in order to achieve the desired movement. Visual feedback of the arm's movement "closes the loop".

Various research groups have actively constructed virtual or mechanical systems, which are different versions of the above description, in order to achieve this goal [Georgopoulos 1986, Zhang 1997, Schwartz 1988, Moran 1999, Schwartz 2000, Wessberg 2000, Issacs 2000, Donoghue 2001, Nicolelis 2001, 2002]. While other researchers mainly access motor areas in the brain in order to extract the necessary information for controlling the prosthetic devices, a research group at Caltech focuses on a pre-motor area called Parietal Reach Region (hereafter abbreviated as PRR) as a source of neuro-prosthetic command signals. It is believed that PRR forms the reaching plans which precede the actual reach [Snyder 1997, Batista 1999, Shenoy 1999, Meeker 2001].

The advantage of using such high-level cognitive brain activities is that they are more anatomically removed from regions that are damaged. While motor areas on the other hand may degenerate following spinal cord injury [Florence 1998, Kaas 2002], most cognitive areas of the brain are known to sustain even after loss of motor functions. Furthermore, the plasticity, which is the capability of learning and adaptation, of the area also holds promise that users may quickly learn to adapt to a brain machine interface [Meeker 2003].

The construction of such a neuro-prosthetic system is no small feat. The quest of designing and building the system involves disciplines ranging from neurobiology to mechanical engineering, in which each field finds its interesting application or challenging questions. Generally speaking, designing and building such a cognitively controlled system requires several large building blocks: behavior experiments and signal harvesting, learning and decoding machinery, control schemes, and system integration. We briefly define each block and its function.

The behavioral experiments are controlled experiments in which the animal performs designated behavior tasks while researchers monitor and record its brain activities. Then either online or off-line, the recorded signals are examined to determine if any possible patterns are embedded in the neural signals so that inferences can be made about the animal's behavioral states during the experiments. The procedure of inferring the animal's behaviors or sensory inputs from its recorded brain activities is termed *decoding*. Next, knowledge gained in the learning/decoding stage enables us to construct

high-level control schemes necessary for commanding prosthetic devices so that they are directed by the user's thoughts. Finally, the software and hardware package must be miniaturized for possible clinical implementation.

Among these building blocks, neural decoding is itself a very active research topic. It includes, but is not limited to, characterizing the firing process of the spike trains and estimating or predicting behavioral parameters from neural activities. A topic of ongoing debate in the community is whether spike trains are rate coded or time coded: the former refers to the assumption that the only informative feature in a spike train is the number of spike counts observed in a time window, while the latter refers to the assumption that timing between spike events also plays a role in conveying information. To answer this question, different metrics and approaches ranging from statistical tools to information theory have been proposed over the years [Teich 1986, Holt 1996, Koch 1997, Johnson 1996, Victor 1999, Johnson 2001]. In addition, the quest to promptly and accurately predict some behavioral parameters from neural activities has also attracted large amount of interest, especially in the emerging field of neural prosthetic systems [L. Abbot 1994, Zhang 1997, Schwartz 1988, Moran 1999, Schwartz 2000, Wessberg 2000, Issacs 2000, Nicolelis 2002].

In order to address the above questions, it is necessary to first understand the stochastic characteristics of the spike train. In this thesis, a novel approach to characterize spike trains is proposed. This approach determines the *Poisson-ness* of a spike train at different scales. It takes advantage of the multi-scale capability of wavelet packets, a relatively

new signal processing technique. Under this approach, the spike trains are projected onto wavelet packets and the distributions of the projection coefficients are analyzed. The coefficients whose empirical distributions significantly deviate from the theoretical distribution of a comparable Poisson process are counted. The higher the counts, the less likely the process is Poisson in nature. It allows us to assess *Poisson-ness* from different scales, thus avoiding the stationary assumptions employed in some other analysis of the spike trains [Gabbinni and Koch 1998]. Both surrogate data and the spike data collected from neurons in PRR are characterized using this approach.

With knowledge of a spike train's underlying stochastic nature, it is natural to extend the wavelet packet approach to the decoding problem described earlier. Most current decoding efforts use the mean firing rate, i.e., the number of spikes in a window to estimate the behavioral or stimulus parameters. When neurons are well characterized as a Poisson process, this decoding model is appropriate. However, using the Haar wavelet packet family, spike train features beyond mean firing rate can be exploited. In addition, these features have biological interpretations that are appealing and intuitive to researchers in the neuroscience community. Of all the features, the most informative ones are the ones with the largest power to discriminate among the behavioral or stimulus parameters; thus, decoding based on these features can potentially improve both accuracy and efficiency. In this thesis I propose an optimal feature selection technique which combines the wavelet packet framework with mutual information, an information theoretic measure. Because of the hierarchical structure of the wavelet packet and the special properties of the mutual information, this method returns the wavelet packet

projection coefficients with the largest decodability towards the decoding task. Finally, I incorporate these selected features into a Bayesian classifier to estimate the behavioral parameters, such as reach directions in the case of decoding from PRR. Again both artificial data and actual neuronal data are used and the decoding performance is compared against the ones using only mean firing rate.

Besides decoding the estimated reach directions from PRR signals, we must estimate additional parameters from neural signals in order to successfully control a robotic device using brain activities. These additional parameters are termed *cognitive parameters* in this thesis. They describe the brain's internal behavioral states. For a minimally autonomous robotic device, we define the behavior states to include a *baseline* state, reach *planning* states, and the reach execution *go* state. Because of the structure of the postulated state transitions, we cast them into a novel framework. When combined with an *Interpreter* that acts on the classification results of these states, it returns an efficient algorithm that extracts the necessary control parameters. Experimental data collected from animals performing a sequence of actions are subjected to this method while we compare different state transition rules.

The contributions of this thesis work include the following:

- A novel wavelet based spike train characterization method that assesses the underlying stochastic properties of given spike trains is introduced and studied. Traditional characterization methods have limitations or shortcoming when dealing with long term correlation or non-stationarity in the data. On the other

hand, because of the statistical properties of the Haar wavelet packet, this method provides versatility and insight into the spike train's characteristics compared to the traditional approaches.

- A wavelet packet based feature extraction method that searches for the most informative features in spike trains is introduced in this thesis. In many decoding problems, researchers automatically use firing rate as the lone feature in their decoding algorithms. Although for spike trains with Poisson nature, firing rate is indeed the only informative feature, as shown in this thesis, not all spike trains exhibit Poisson characteristics. Thus, more generally it is necessary to search for features embedded in the spike trains that are most informative towards decoding. The algorithm introduced here combines information theoretic measures with wavelet packet tree pruning techniques and returns features that offer improved decoding performance.
- Finally, this thesis offers a first look at decoding cognitive states from reach movement sequences. For practical purposes, a neural prosthetic system requires control signals beyond mere reach directions. Thus, this thesis presents a framework based on finite state machine, and different transition rules are explored. Although the framework is very simple, it is the first in the field that demonstrates the feasibility of using cognitive parameters to control autonomous prosthetic arm systems.

This thesis is organized as follows:

- Chapter 2 provides background information on the experimental paradigms used to collect neural data, and introduces the data type used in this thesis. A brief review of the wavelet and wavelet packet concepts, with a focus on Haar wavelet family, is also presented in the chapter. And finally, we review the Bayesian classifier, which is the principal estimation tool used in the thesis.

- Chapter 3 describes a method to characterize spike trains using the Haar wavelet packet function. We investigate the probabilistic properties of the wavelet packet projection coefficients of Poisson processes. From the analysis, we derive both the analytical forms of the distribution and an iterative method that approximate these distributions in practical situations. Additionally this chapter proposes a test that investigates the Poisson-ness of an unknown spike processes. This chapter concludes with applications of the test to different types of data.

- Chapter 4 presents a framework for decoding behavioral parameters from neural activities. First we review mutual information as a measure that quantifies the discriminability of each feature. Then we introduce an algorithm that uses the mutual information as the decodability score and prunes the wavelet packet tree in search of the best features for decoding. We compare the decoding performance using the optimal features to the performance obtained when using just standard firing rates with applications to surrogate data as well data from neurons in PRR. In the appendix, we also present a finite sample analysis that further justifies the use of mutual information.

- Chapter 5 presents work on decoding logic parameters and sequences of behaviors. We define the necessary states and the state transition concepts that enable a construction of an autonomous model. When coupled with an *Interpreter*, this model allows us to integrate decoding with state transition rules so that we can extract practical control signals for a prosthetic system. Several different *Interpreter* rules are explored as we compare their performance to reach sequences recorded from the animals.

Some final remarks as well as some future works are proposed in Chapter 6 to conclude this thesis.

Chapter 2 Background

This chapter provides background information on the experimental setup and the mathematical model of the neural data used in the thesis. Also, brief overviews of wavelet and wavelet packet are presented as well. Finally, we discuss relevant concepts from Bayesian classification, which is the principal classification tool used through out the thesis.

2.1 Experimental setup and data type

Most of the actual neuronal data used in this thesis are obtained from behavioral experiments that were conducted on *Rhesus* monkeys (*Macaca mulatta*) performing delayed center-out reach tasks, which are illustrated in Figure 2.1.

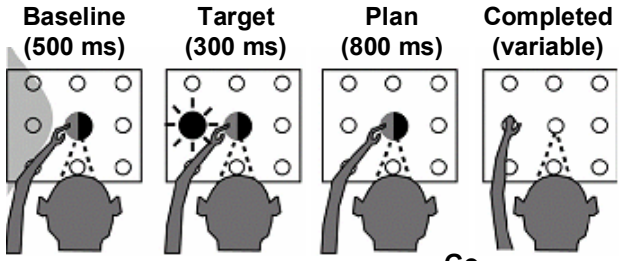

Figure 2-1 Center-out reach task

In the *physical reach* experiments, the animal is secured with the head position fixed in front of a vertical touch screen in a dark room. At the start of each trial, a fixation dot (red) is first displayed at the center of the touch screen where the animal fixates both its hand and eye. After ~500 ms of fixation, a reach target (green) is shown to the animal for 300 ms. The animal is required to memorize the reach direction and to form a reach plan in the next ~800 ms while it is still holding the arm and eye on the fixation dot. After the plan period, the fixation dot extinguishes, and the animal makes a reach to the previously

shown target location. A juice reward is administered upon a successful completion of the trial. The target locations are randomly chosen among 8 different locations, and the length of the plan period is also randomized to minimize an anticipation effect [Batista 1999, Meeker 2001].

Alternatively, a *virtual reach* experiment very similar to the *physical reach* experiment is carried out in order to simulate a neural prosthesis at work, and also to explore the learning capability of PRR. The distinction between the *physical reach* and the *virtual reach* is that in the latter, the animal does not actually perform the reach movement. Instead of moving its arm towards the target, the animal forms the intention of making the movement, which is subsequently decoded. Based on the decoded reach direction, a visual feedback (yellow dot) appears on the touch screen. The animal is given the juice award if the decoded reach direction matches the target.

The recording apparatus consists of a custom-made micro-electrode, signal amplifier, A/D converter, and spike detection and sorting software. The micro-electrode is a 10 cm long glass-coated platinum-iridium wire with the diameter 0.4 mm. The wire is insulated throughout except at the sharpened tip, thus giving it an impedance of 1.5-2 MOhm. The wire is housed in a glass guide tube of diameter 0.5 mm so that it can penetrate the dura upon insertion. The A/D converter has a sampling frequency for 40 KHz for the brain activities.

During a recording session, the electrode is first acutely inserted into the brain's functional area pre-determined using fMRI. Then using a micro-drive, the electrode is advanced incrementally at 700 microns per step in the vicinity of PRR in searching for extra-cellular neuronal activities. Once extra-cellular activities are detected, the animal is required to make a sequence of movements to the 8 different locations in order to decide the relevance of the neuron with respect to the behavior paradigm. If no identifiable correlation exists between the neural activity and the reach locations, the electrode is advanced further until new extra-cellular activities are detected; otherwise, the electrode is fixed at the position that exhibits behaviorally modulated neural activities. Figure 2-2 displays a trace of recorded PRR neural activity. The local surge of the voltage is called the *action potential* fired by the neuron.

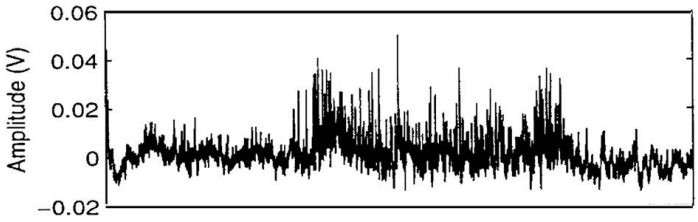

Figure 2-2 Trace of neural activities from a neuron in PRR

***X*-axis is the time and *y*-axis is the amplitude in voltage. The sudden surges of the voltage amplitude are action potentials, and the timing of the action potentials marks the occurrence of the spikes.**

The analog raw waveform is then sampled at 40KHz. Because the recorded extra-cellular neural activities may contain signals from several neighboring neurons, spike sorting is necessary in order to decipher the signals on a neuron by neuron basis [Abeles 1977]. In another word, we need to sort the spikes (action potentials) from the signal and label them with the corresponding neurons that generate the specific waveforms. The spike sorting algorithm uses either principal components analysis (PCA) based method or

template method [Lewicki 1998]. Once the spikes are sorted, the time of occurrence of each spike is recorded to a precision of 1ms. A sequence of the spikes forms a spike train, which is one of the most frequently used data types in the neuroscience community. This thesis thus places a strong emphasis on the spike train data format though some of the techniques described have broader applications. The model of the spike train will be the topic of next section.

All of the experimental neural signals used in this thesis are recorded from the Parietal Reach Region (PRR), a sub-region of Posterior Parietal Cortex. PRR is believed to be responsible for reach intentions or planning. A series of papers on this area suggest that it not only encodes the reach plan in the retinotopic coordinates, but also codes the next movement target in a sequential reach task [Snyder 1997, Batista 1999]. Therefore, unlike motor areas, PRR encodes relatively simple movement parameters in a straightforward coordinate frame. In addition, the posterior parietal cortex bridges the sensory-motor transformation areas, which may be important for the type of learning necessary for the proper alignment of sensory maps with motor maps, as demonstrated in some recent works [Meeker 2003]. The learning ability of the area is especially appealing for neural prosthetic applications because PRR may retain or quickly re-establish the reach planning ability. Taking advantage of its learning ability thus may prove necessary for optimizing the performance of a neural prosthesis.

2.2 Spike train representation

In the previous section, a brief description on the data collection apparatus is introduced. The over-sampled analytical signals as seen in Figure 2.2 are further processed to generate spike trains. The two basic pre-processing steps are spike detection and spike sorting. The spike detection step separates the action potentials from background noises such as thermal noise of the recording equipment and the average response from neighboring neurons. There are many detection methods in existence, and the one applied in this thesis is the thresholding method [Humphrey 1979, Abels and Goldstein 1977, Nenadic 2003]. It indicates the presence of a spike when a local peak of the raw analytical signal passes a threshold. As a stream of spikes is recorded, the next step is to classify the spikes to their respective source neurons because not all observed spikes are originated by the same neuron. Many times two or three neighboring neurons may be responsible for some of the spikes. The spike sorting technique used in this thesis is the template method [Lewicki 1998]. Because the spike waveforms (128 data points of the raw data centered around a peak) are markedly different given different neurons while remaining homogeneous for the same neuron, the template method matches different templates to all the observed spike waveforms. The ones exhibit similarities are classified as being from the same neuron; and vice versa. Thus, the raw analytical signal is deciphered into several data streams, each with spikes believed to be generated from different neurons. In addition, because the spike waveforms for a given neuron are very homogeneous, only the timings of the spikes are retained [Rieke 1997]. Finally, because the refractory period physically limits a neuron's ability to fire consecutive spikes within

2 ms, the processed and sort signals are down sampled to 1 kHz. This processed version of the spike will be used throughout this thesis.

We employ a standard representation of a spike train as a binary function with 0's and 1's. We assume that the onset of a spike can be localized at best to a sampling interval of length δT. Moreover, we assume that spikes are sampled over an interval of length T, where $T=2^m\delta T$ for some integer m. With this assumption, a spike train, s, can be described as

Equation 2.1
$$s(t)=\begin{cases}1 & in\ \ I_k=[k\delta T,(k+1)\delta T]\ \ \ if\ there\ is\ a\ spike\ in\ I_k,\\ 0 & in\ \ I_k=[k\delta T,(k+1)\delta T]\ \ \ if\ there\ is\ no\ spike\ in\ I_k,\end{cases}.$$

Equivalently, a spike train can be interpreted as a T-dimensional vector (where $T=2^m$ for some integer m), whose k^{th} element is determined as

Equation 2.2
$$s_k=\begin{cases}1 & if\ \ there\ \ exists\ \ a\ \ spike\ \ in\ \ I_k=[k\delta T,(k+1)\delta T]\\ 0 & otherwise\end{cases},$$

where $k=0,\ldots,T-1$. For some analyses, we further assume that there exists an ensemble of N spike trains gathered under repeated behavioral, stimulus, and recording conditions. Conceptually, these different spike trains are different samples of the same underlying stochastic process. A superscript will index the members of the ensemble: $\{s(t)\}^{i=1,..,M}$. In all the computational examples of this paper, the sampling interval δT is taken to be *1*ms because of the *refractory period*. It is the physiological limit on the time intervals between two consecutive spikes fired by the same neuron. Generally the refractory period is taken to be 2ms, meaning a neuron can not fire a spike within the 2ms following an earlier firing [Rieke 1997].

2.3 Haar Wavelet Packet Projection

We now review the Haar wavelet packet, its waveform, and its construction. Details are outlined in several standard textbooks on wavelet theory [Daubechies 1992, Wickhauser 1994, Mallat 1999, Percival and Walden 2000]. This section also establishes our notation for the projection coefficients of the spike trains. Knowledgeable reader may skip this section and proceed directly to Section 2.4.

2.3.1 Haar Wavelet Review

A wavelet basis is a set of orthonormal functions that partition the time-frequency domain in a dyadic fashion. As shown below, wavelets are constructed from a choice of scaling function and a set of filters. In one sense, a filter can be interpreted as a set of coefficients that are applied to a data stream in order to reveal meaningful features. That is, let a filter be defined by a set of coefficients, $\{h_k\}$, $k=1,..,L$. The filter output is given by

$$v_i = \sum_k h_k \, x_{i+k} \ ,$$

where x_k represents the raw data stream, the h_k's are the filter coefficients, and v_i is the filter output, or feature. From another perspective, filters are usually described by their frequency domain characteristics because the filtering operation resembles convolution, which is equivalent to multiplication in the frequency domain [Oppenheim 1999]. Some basic types of filters include low pass (attenuates high frequency) and high pass (attenuates low frequency). In this section we describe a filter by its filter coefficients.

We begin with the continuous wavelet function. First we define a low pass filter H by coefficients $\{h_k\}$ and a complementary high pass filter G by coefficients $\{g_k\}$, where the coefficients $\{g_k\}$ and $\{h_k\}$ are required to have the following relationship: $g_k = (-1)^k h_{L-k}$, L being the number of filter coefficients. These filters are generally termed Quadrature Mirror Filters (QMF) [Percival 2001]. Next define a *scaling function*, $\phi(t)$, that satisfies the following conditions,

Equation 2.3
$$\phi(t) = \sqrt{2}\sum_{k=1}^{L} h_k \phi(2t-k), \qquad \int_{-\infty}^{\infty} \phi(t)\, dt = 1.$$

For simplicity, we denote the analogous operations of convolution and scaling by a factor of two ("decimation") with respect to the filter pair $\{h_k\}$ and $\{g_k\}$ by H and G, i.e.,

$$Hf = \sum_k h_k f(2t-k) \qquad Gf = \sum_k g_k f(2t-k)\ .$$

Now construct a function, $\psi(t)$, complimentary to $\phi(t)$, such that

Equation 2.4
$$\psi(t) = \sqrt{2}\sum_k g_k\, \phi(2t-k) \qquad \int_R \psi(t)\, dt = 0,$$

where $\psi(t)$ is termed the *wavelet function*. For the Haar wavelet function, the low pass filter and the high pass filter coefficients are *{1 1}* and *{-1 1}*, respectively. The associated scaling function and wavelet functions are plotted in Figure 2.3.

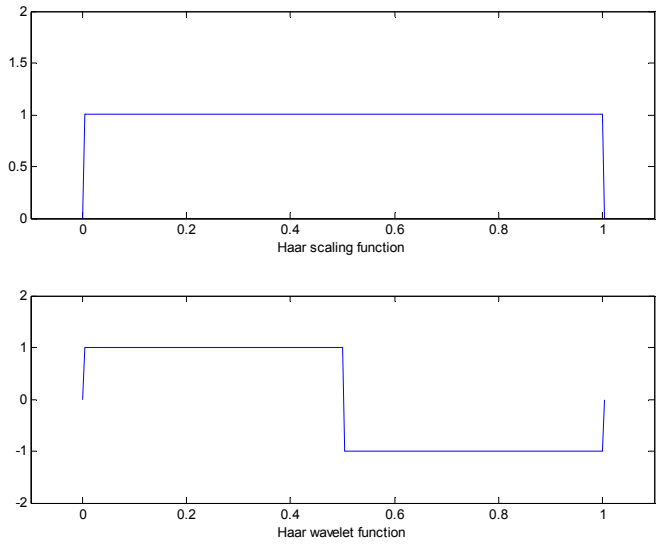

Figure 2-3 Haar scaling function and Haar wavelet Function on the interval *[0 1]*.
***X*-axis is the time in ms and *y*-axis is the value of the functions.**

The strength of wavelet-based analysis for this application resides in both its multi-resolution analysis (MRA) capability and the computational efficiency of the associated numerical algorithms. To understand MRA, consider a nested sequence of subspaces $\{V_j\}_{j\in Z}$ of $L_2(R)$, where Z is the set of integers and $L_2(R)$ is the space of all square integrable functions. These nested subspaces satisfy the following conditions:

C1 $\cdots \subset V_{j-1} \subset V_j \subset V_{j+1} \subset \cdots \subset L_2$ for all $j \in Z$,

C2 $\lim_{j\to\infty} V_j = L_2$,

C3 $\lim_{j\to-\infty} V_j = \{0\}$.

Further, define another complementary set of subspaces $\{W_j\}_{j\in Z}$ such that

$$V_{j+1} = V_j \oplus W_j .$$

Combining the above definitions, the space $L_2(R)$ can be expressed as

$$L_2(R) = \bigoplus_{j=-\infty}^{\infty} W_j .$$

This relation is termed a Multi-Resolution Analysis [Mallat 1999]. Using the actions of translation and dilation, one can construct the following indexed version of the wavelet function, $\psi(t)$,

$$\psi_{j,k}(t) = 2^{j/2}\psi(2^j t - k),$$

where j is the scale (or dilation) index and k is the location (or translation) index. Because for a fixed integer j^*, the set of functions $\{\psi_{j^*,k}(t) \mid k = 1,....\}$ forms a basis for the subspace W_{j^*}, the set of functions $\{\psi_{j,k}(t) \mid j = 1,...; k = 1,...\}$ forms a basis for $L_2(R)$ with different resolutions indexed by j [Percival 2001]. Hence any signal $f(t) \in L_2(R)$ can be represented as a weighted sum of the wavelet bases:

$$f(t) = \sum_{j,k} v_{jk}\, \psi_{j,k}(t),$$

where the weighting coefficients v_{jk} are obtained by projection onto the wavelet basis via the regular inner product on $L_2(R)$,

$$v_{jk} = \int f(t)\, \psi_{j,k}(t)\, dt .$$

Even though the MRA is defined for the continuous function space, $L_2(R)$, its construction can be easily generalized to the domain of discrete data. Consider a vector X in R^T, the space of all T-dimensional vectors, where $T = 2^m$ with m an integer. We can interpret X as a discrete sampling of a continuous function at sampling interval δT. With this interpretation in mind, the scaling function $\phi(t)$ is scaled and adapted to each

sampling interval of the discrete data. We denote the resulting set of adapted scaling functions as $\phi_{0k}(t)$, whose support is $[k\delta T,(k+1)\delta T]$ for *k=0,...,T-1*. Now apply the low pass filter $\{h_k\}$ and the high pass filter $\{g_k\}$ to the set of adapted scaling functions $\phi_{0k}(t)$ so that,

Equation 2.5 $$\phi_{1k} = \sum_l h_{l-2k}\phi_{0l} \ ,$$

Equation 2.6 $$\psi_{1k} = \sum_l g_{l-2k}\phi_{0l} \ .$$

We note the support of the functions $\phi_{1k}(t)$ and $\psi_{1k}(t)$ is $[2k\delta T,2(k+1)\delta T]$ for $k = 0,...,\frac{T}{2}-1$. Moreover, the sets of functions $\phi_{1k}(t)$ and $\psi_{1k}(t)$ are called the scaling function and the wavelet functions at scale *j=1*. We can extend Equation 2.3 and Equation 2.4 recursively for all j such that

Equation 2.7 $$\phi_{jk} = \sum_l h_{l-2k}\phi_{j-1l} \ ,$$

Equation 2.8 $$\psi_{jk} = \sum_l g_{l-2k}\phi_{j-1l} \ ,$$

where the sets of functions $\phi_{jk}(t)$ and $\psi_{jk}(t)$ are called the scaling function and the wavelet functions at scale *j*, and their support is $[2^j k\delta T,2^j(k+1)\delta T]$. The recursion stops at scale $j=log_2T$, where both the wavelet function and the scaling function have support [*0 T*], with *T* being the presumed length of the spike train data sequence. For the Haar wavelet function, the low pass filter and the high pass filter are $\{h_0=1\ h_1=1\}$ and $\{g_0=-1\ g_1=1\ \}$ respectively. The scaling and wavelet function up to scale *j=2* are plotted in the following tree diagram (Figure 2.4),

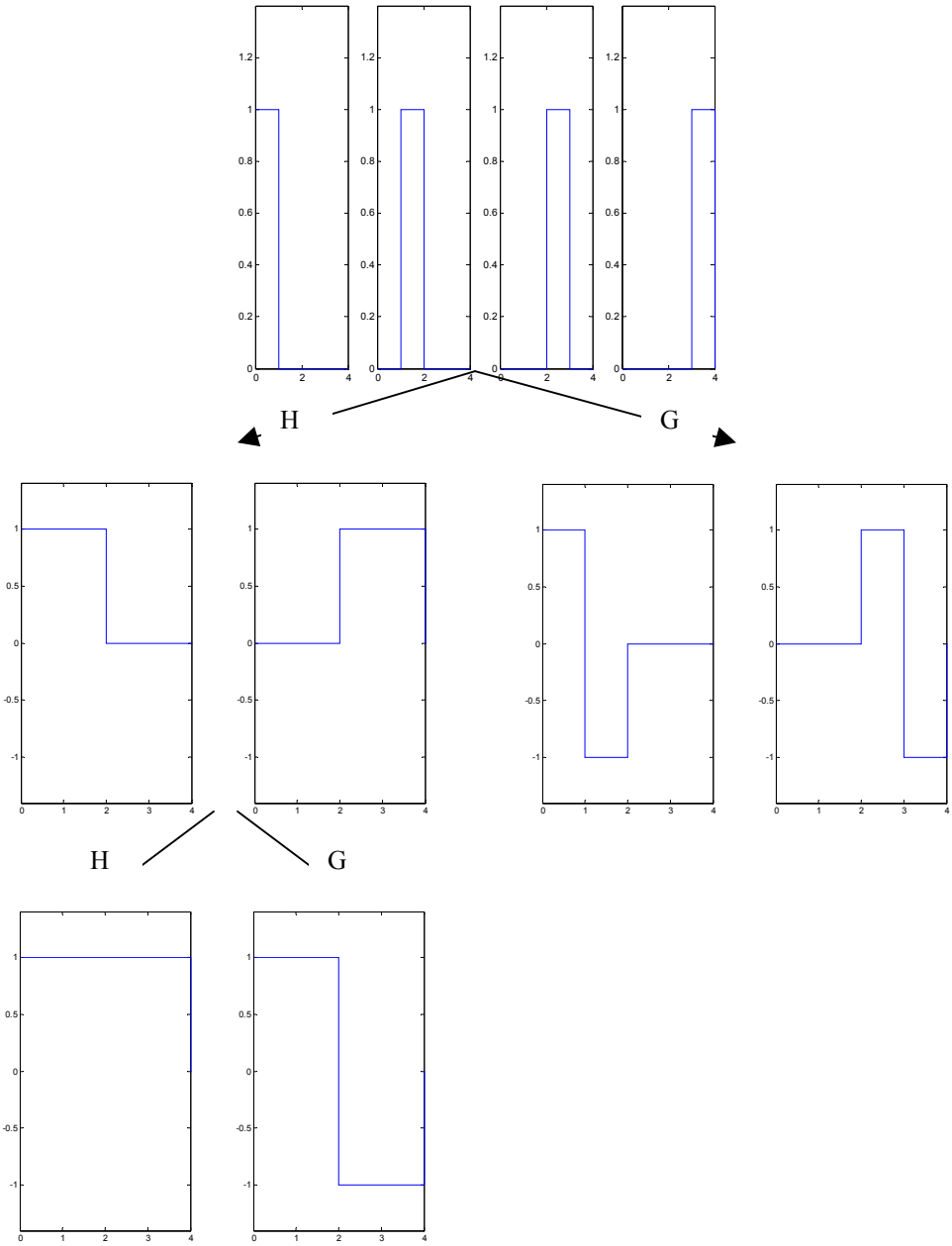

Figure 2-4 Haar wavelet and scaling functions up to scale *j=2*.

The top panel contains the scaling functions at scale j=0, for this example, *k=1,2,3,4*. The middle left panel contains the scaling function at scale j=1, and the middle right panel contains the wavelet function at scale j=1. The bottom left panel is the scaling function at scale j=2, and the bottom right panel is the wavelet function at scale j=2. The symbols H and G indicate the filtering operation that generates these functions. Notice the support at each scale increases dyadicly.

This recursive relationship also enables MRA in the discrete context.

The above application of the wavelet functions to the discrete data inspires the so-called *Pyramid Algorithm* [Mallat 1999], an efficient method for computing the wavelet projection coefficients of discrete data. Again we take a vector $X=\{x_0,\ldots,x_{T-1}\}$ in R^T, the space of all T-dimensional vectors, where T is a power of 2. Similarly, we interpret the vector X as a piece-wise constant continuous function with constant values x_k over the sampling interval $[k\delta T,(k+1)\delta T]$ for $k=0,\ldots,T-1$. The projection coefficients of X onto the 0^{th} scale scaling functions are,

$$u_{0k} = \int X(t)\phi_{0k}(t)dt .$$

Because $X(t)$ is a piece-wise constant function with piecewise support coinciding with the support of $\phi_{0k}(t)$, and by Equation 2.3,

$$u_{0k} = x_k .$$

Therefore, the finest scale coefficients are exactly the input data itself. Now we can use the low pass filter $\{h_k\}$ and the high pass filter $\{g_k\}$ to recursively compute the wavelet coefficients at each scale. The governing equations for the Pyramid Algorithm are

Equation 2.9 $$u_{jk} = \sum_l h_{l-2k} u_{j-1,l} ,$$

Equation 2.10 $$v_{jk} = \sum_l g_{l-2k} u_{j-1,l} ,$$

where the $\{v_{jk}\}$ are the wavelet projection coefficients and the $\{u_{jk}\}$ are the scaling projection coefficients, an intermediate set of coefficients that are derived by projecting the signal $f(t)$ onto the scaling function $\phi_{jk}(t)$. In addition, the cardinality of the sets $\{v_{jk}\}$

and $\{u_{jk}\}$ at each scale are $\frac{T}{2^j}$. For the Haar wavelet, we can illustrate the idea behind the Pyramid algorithm using a decomposition tree similar to the one illustrated in Figure 2.4, where each node at level j in the tree represents a set of wavelet coefficients at scale level j (Figure 2.5).

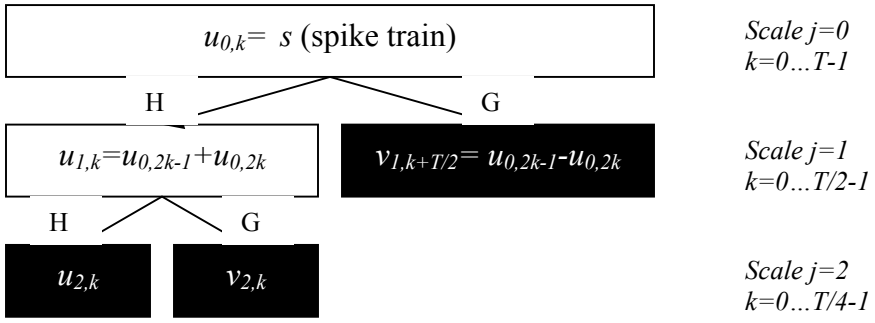

Figure 2-5 Pyramid Algorithm for the special case of Haar wavelet decomposition

At scale *j=0*, the scaling coefficients $u_{0,k}$ are the input data sequence whose length is *T*. At scale *j = 1*, we obtain the scaling coefficients $u_{1,k}$ and wavelet coefficients $v_{1,k}$ by performing the convolution-decimation operation with *H* and *G*, respectively. Note the cardinality of the coefficient set is now *T/2* because of the decimation. The two nodes at *j=1* are termed *children* of the parent node at *j=0* because they are derived from that parent node. Similarly, the scaling coefficients $u_{2,k}$ and wavelet coefficients $v_{2,k}$ at scale *j=2* are generated from the parent node at scale *j=1*, and their corresponding cardinality is *T/4*. Using this algorithm, we can proceed to calculate the wavelet coefficients at all scales until the size of the coefficient set equals 1.

2.3.2 Haar Wavelet Packet

The *wavelet packet* is an extension of the basic wavelet construction described above. Because wavelet packets are a super-set of wavelets, they offer a richer selection of basis functions. In the context of the spike train classification problem, this added richness yields a more refined analysis of the spike train. The construction of the continuous Haar wavelet packet basis functions again involves a low pass filter $\{h_k\} = \{1,1\}$ and a complementary high pass filter $\{g_k\} = \{1,-1\}$. Assuming that the wavelet functions $\psi(t)$

defined below have support on the real interval [*0 1*], we can again apply the convolution and decimation operation recursively to define the set of functions,

$$\psi_{2n}(t) = \sum_k h_k \psi_n(2t-k)$$
$$\psi_{2n+1}(t) = \sum_k g_k \psi_n(2t-k)$$,

where the sum is over the cardinality of the filter coefficients h_k and g_k, and for the Haar wavelet,

$$\psi_0 = \begin{cases} 1 & if \quad t \in [0 \quad 1) \\ 0 & otherwise \end{cases}.$$

Note that ψ_0 is the same as the Haar wavelet scaling function, and ψ_1 is the Haar wavelet described above.

Like wavelets, wavelet packets can be extended to the discrete MRA using the double index of scale *j* and location *k*. Consider a vector *X* in R^T, the space of all *T*-dimensional vectors, where *T* is again a power of 2. With the interpretation of the piece-wise constant function in Section 2.3.1, the scaling function $\phi(t)$ is first scaled and adapted to each sampling interval of the discrete data. We denote the resulting set of adapted scaling functions as $\psi_{0k}(t)$, where

Equation 2.11
$$\psi_{0k}(t) = \begin{cases} 1 & if \quad t \in [k\delta T, (k+1)\delta T] \\ 0 & otherwise \end{cases},$$

whose support is $[k\delta T, (k+1)\delta T]$ for *k=0,...,T-1*. Now we apply the low pass filter $\{h_k\}$ and the high pass filter $\{g_k\}$ for all *j* such that

Equation 2.12
$$\psi_{jk} = \sum_l h_{l-2k} \psi_{j-1l}$$

Equation 2.13

$$\psi_{jk+\frac{T}{2^j}} = \sum_l g_{l-2k}\psi_{j-1l},$$

where the sets of functions $\psi_{jk}(t)$ have support $\left[2^j k\delta T, 2^j(k+1)\delta T\right]$, and the limit of the summation is the cardinality of the filter coefficients H and G. The recursion stops at scale $j=log_2 T$, where both the wavelet packet functions have support [*0 T*]. For the Haar wavelet function, the low pass filter and the high pass filter are $\{h_0=1\ h_1=1\}$ and $\{g_0=-1\ g_1=1\}$ respectively, thus the relationship becomes

$$\psi_{j,k}(t) = \psi_{j-1,2k-1}(t) + \psi_{j-1,2k}(t), \text{ if low pass}$$

$$\psi_{j,k+\frac{T}{2^j}}(t) = \psi_{j-1,2k-1}(t) - \psi_{j-1,2k}(t), \text{ if high pass}$$

where *j* is the scale index, *k* is the position index, and *T* is the length of support of the filter at the largest scale, as defined above. An example of Haar wavelet packets and their recursion relationship is shown graphically in Figure 2-6.

A

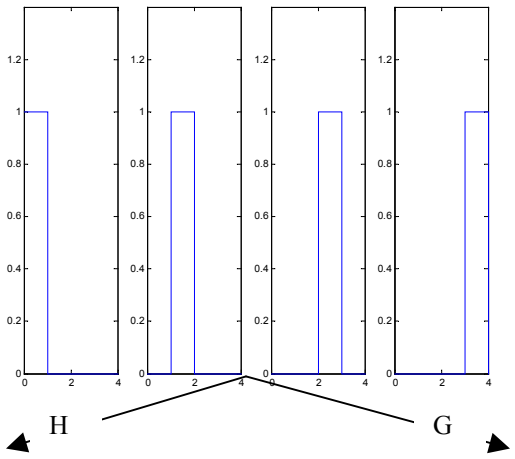

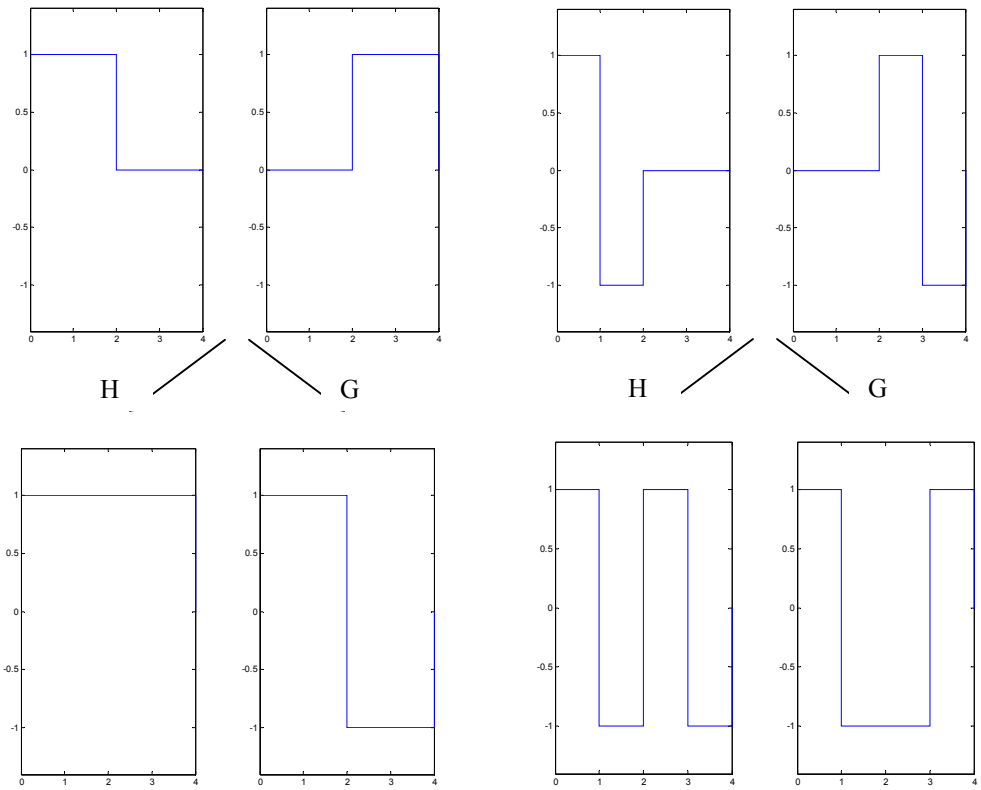

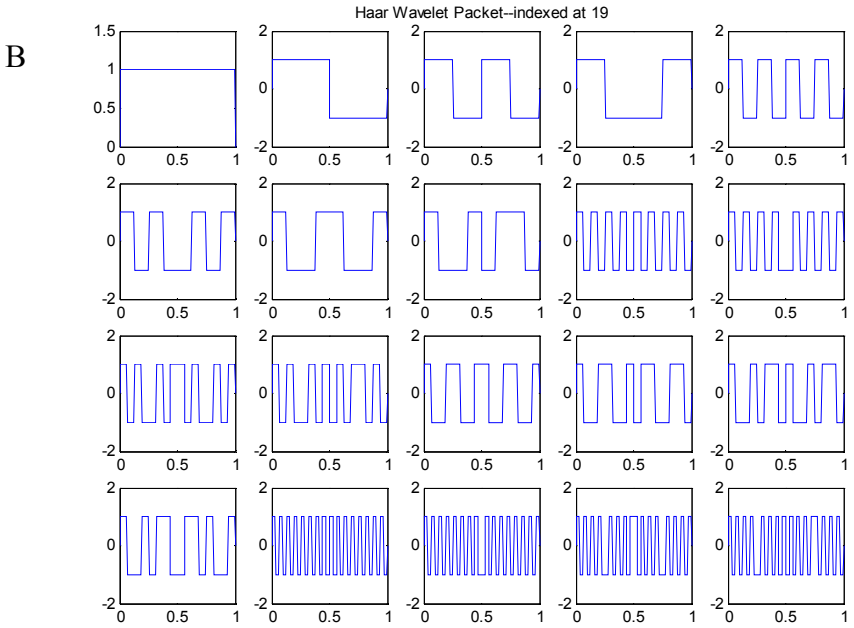

Figure 2-6 Haar wavelet packet functions up to scale *j=2.*

A) **The top panel contains the wavelet packet functions at scale j=0. It is identical to the scaling function. The middle left panels contain the wavelet packet functions at scale j=1 as a results of the low pass filtering, and the middle right panels contain ones as a results of high pass filtering. The two bottom left panels contain the wavelet packet functions that are children of the two middle left ones, and similarly the two bottom right ones are children of the two middle right ones. The H and G indicate the filtering operation towards these functions. Notice the support at each scale increases dyadicly. B) The Haar wavelet packet functions on [0 1] up to the 19th iteration.**

In particular, we notice that the set of Haar wavelet functions is the left vertical branch in the packet tree (Figure 2.6A).

An interesting property of the Haar wavelet packet functions is the orthogonal relationship between all of the packet functions. Before describing the orthogonality in detail, we first define several relevant terms. A *tree* is an arrangement of the wavelet packet functions such that they are structured in a branching fashion. A *node* N_{jl} is either a tree branches or a tree leaf, and at a given scale j there are 2^j nodes. In the above example, there are 1 node N_{01} at scale $j=0$, 2 nodes at scale $j=2$, and 4 nodes at scale $j=3$. Moreover, the *member functions* of a node are defined as the wavelet packet functions related to each node. The relationship is the constructive iteration shown in Figure 2.6. The number of member functions for any node at scale j is $T/2^j$, where T is the length of the input vector under investigation. Now we are in position to discuss the orthogonality property.

Proposition 2.1 *Member functions of each node are orthogonal to the member functions of any nodes residing on a different branch of the dyadic tree.*

For example, in the above figure, the member functions of N_{21} are orthogonal to the members of N_{22}, N_{23}, and N_{24}. Likewise, it is also orthogonal to the parent node of N_{23} and N_{24}, namely N_{12} because N_{21} and N_{12} do not share a branch.

Proof:

Note that the member functions of any two child nodes derived from the same parent are orthogonal. To show this, directly integrate the functions:

$$\int \psi_{jk_1}(t)\psi_{jk_2}(t)dt,$$

where $\psi_{jk_1}(t)$ is a member function of N_{jl_1} and $\psi_{jk_2}(t)$ is a member function of N_{jl_2}. There are two possibilities for the above integration:

1) If $k_2 \neq k_{1+2^{J-j}}$, then $\int \psi_{jk_1}(t)\psi_{jk_2}(t)dt = 0$ because by construction, ψ_{jk_1} and ψ_{jk_2} have non-overlapping support.

2) If $k_2 = k_{1+2^{J-j}}$, then

$$\begin{aligned}
&\int \psi_{jk_1}(t)\psi_{jk_2}(t)dt \\
&= \int [\psi_{j-1,2k_1-1}(t) + \psi_{j-1,2k_1}(t)][\psi_{j-1,2k_1-1}(t) - \psi_{j-1,2k_1}(t)]dt \\
&= \int \psi^2_{j-1,2k_1-1}(t) - \psi^2_{j-1,2k_1}(t)dt \\
&= 0
\end{aligned}.$$

In addition, the wavelet packet functions contained in the branches derived from the two child nodes are also orthogonal. To see this, we observe that the space spanned by the first child node is orthogonal to the one spanned by the second child, i.e.,

$$S_1 = Span\{\psi_{jk_1}\},\ k_1 \in child\quad node\ \ 1$$

$$S_2 = Span\{\psi_{jk_2}\},\ k_2 \in child\quad node\ \ 2$$

$$S_1 \perp S_2$$

because the member functions, $\{\psi_{jk_1}\}$ and $\{\psi_{jk_2}\}$ are orthogonal as shown earlier. Moreover, the wavelet packets contained in the branches of the two child nodes are linear combinations of the ones in $\{\psi_{jk_1}\}$ and $\{\psi_{jk_2}\}$ by construction. Hence they are also orthogonal to one another.

Therefore, we have shown that the wavelet packet functions in any node are orthogonal to the ones in nodes that are a member of a different branch. □

Similarly, we can adopt the *Pyramid Algorithm* to efficiently compute the projection coefficients of the wavelet packets. The algorithm is almost identical to the one used for wavelets, with the only difference being that the branching of the wavelet packet tree occurs at every node, while branching occurs only in the first node of its wavelet counterpart. We can likewise devise a tree diagram to illustrate the decomposition of a *T*-dimensional vector (Figure 2-7)

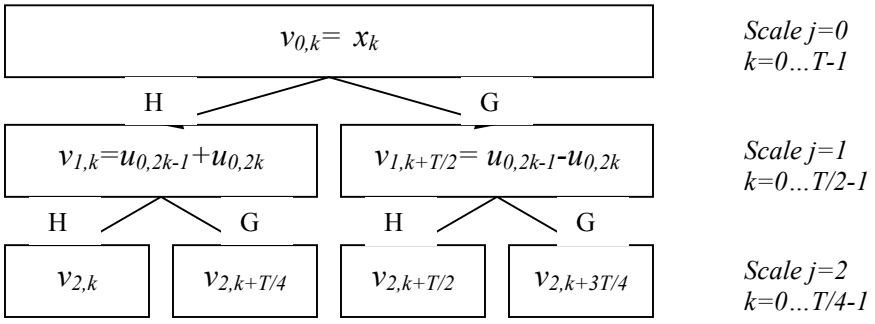

Figure 2-7 Pyramid Algorithm for the Haar wavelet packet decomposition

At scale *j=0*, the coefficients $v_{0,k}$ are the input data sequence whose length is *T*. At scale *j = 1*, we obtain the coefficients $v_{1,k}$ and $v_{1,k+T/2}$ by performing the convolution-decimation operation with *H* and *G*, respectively. Note the cardinality of the coefficient set is now *T/2* because of the decimation. The two nodes at *j=1* are termed *children* of the parent node at *j=0* because they are derived from

that parent node. Similarly, the same relationship is observed at scale *j=2*, in which the cardinality of the coefficients in each node becomes *T/4*.

Using this version of the Pyramid Algorithm, we can efficiently compute all the wavelet packet coefficients up to scale $j=log_2T$. In all, the wavelet packet decomposition of a vector of length T returns $TlogT$ wavelet packet coefficients, compared to the T coefficients by wavelet decomposition.

2.3.3 Computing the Projection Coefficients

Using the concepts and the background presented in the previous sections, the T-dimensional spike train, $\boldsymbol{s}=\{s_0,\ldots,s_{T-1}\}$ can be projected onto the Haar wavelet packets using the aforementioned Pyramid Algorithm.

Based on spike train model shown in Section 1, the 0^{th} scale wavelet packet coefficients $v_{0,k}$ are precisely the original spike train s_k,

Equation 2.14
$$v_{0k} = s_k .$$

For the Haar wavelet packet, the recursive relations for the remaining coefficients then become

$$v_{j,k}(t) = v_{j-1,2k-1}(t) + v_{j-1,2k}(t) \text{ , if low pass}$$

$$v_{j,k+\frac{T}{2^j}}(t) = v_{j-1,2k-1}(t) - v_{j-1,2k}(t) \text{ , if high pass.}$$

2.4 Biologically Relevant Properties of the Haar Wavelet Packet

Although there are many possible choices of wavelet functions, the Haar wavelet packet carries some special properties which make it an appealing choice for projecting, analyzing, and interpreting spike trains. As seen in Section 2.3, the Haar wavelet packet functions have compact support in the time domain. This bodes well with the fact that spike trains consist of spike signals with support as small as the sampling interval δT. In other words, Haar wavelet packet functions completely capture the discrete nature of the spike trains. On the other hand, other basis functions such as trigonometric functions would produce undesirable artifacts because of Gibb's phenomenon. Furthermore, some of the Haar wavelet packet projection coefficients have intuitive interpretations that relate them to measures widely recognized in neuroscience. For example, the coefficient v_{j1} at a scale j corresponds to the number of spikes in a window of length $T/2^j$, with which we can express the mean firing rate in that window as $2^j v_{j1}/T$. In other words, the v_{j1} corresponds to the mean firing rate in an associated time interval, or window (see Figure 2-8a). Furthermore, coefficients such as v_{j2} are closely tied to the local change of firing rate, often observed in the case of changing stimulus (see Figure 2-8b), i.e., this coefficient corresponds to a localized slope in the Post-Stimulus Time Histogram (PSTH) [Rieke 1997]. Finally one can describe bursting, a local consecutive firing of spikes, using highly oscillatory wavelet packet functions that reside in a small time window (Figure 2-8c). Some other advantages of Haar wavelet packet will be evident in the subsequent sections.

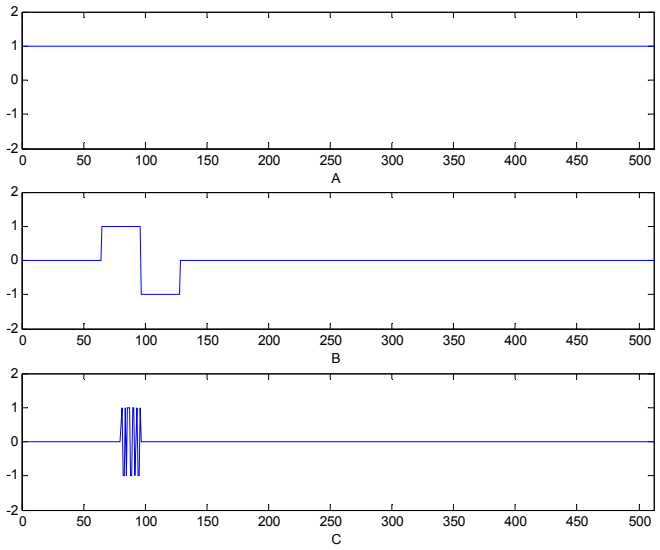

Figure 2-8 Haar wavelet packet function at different scale and locations over 512 units of the basic sampling period δT

A. $j=9$, $k=1$, the wavelet packet function corresponds to a window that spans the whole 512 units. Consequentially, the resulting coefficient $v_{9,1}$ correlates to the mean firing rate in the sampling window of length 512 δT. B. $j=6$, $k=10$, the wavelet packet function corresponds to one up-down cycle over 64 units. The resulting coefficient $v_{6,10}$ in this case represents the difference of the firing rate in two consecutive 32 units windows. C. $j=4$, $k=300$, the wavelet packet function corresponds to high frequency oscillation in a 16 units window. The resulting wavelet coefficients $v_{4,300}$ have direct implication on local bursting activities.

2.5 Bayesian classifier

This section reviews basic concepts about the Bayesian classifier, a widely used classification method. It classifies an unlabeled observation by estimating its probability associated with each different class. More rigorously, denote the stimulus parameter (class label) as X and the feature (unlabeled observation) as v, both are random variables. Then the ubiquitous Bayes' rule states that

Equation 2.15

$$P(X \mid v) = \frac{P(v \mid X)P(X)}{P(v)},$$

where X is the class label, v is the feature, $P(X|v)$ is the posterior probability, $P(X)$ is the prior probability of X, and $P(v|X)$ is the likelihood of v given X. In this thesis X is interpreted as the reach direction, and v as the neural signals. Bayesian classification is based on the principle,

Equation 2.16
$$\tilde{X} = \arg\max_{X} \{P(X \mid v)\},$$

the estimated class or reach direction $\tilde{X}$ is the one that maximizes the posterior probability $P(X|v)$.

Since the conditional probability $p(v|X)$ must be estimated, this thesis estimates the conditional densities using the Parzen window method [Parzen 1965]. The Parzen window approach applies Gaussian kernels to the observed data and returns density estimation in the form of the normalized sum of Gaussians centered at each data point. We can write the resulting density function as

$$p(v \mid X = c) = \frac{1}{N_c} \sum_{i=1}^{N_c} G(v - v_i, \sigma),$$

where $G(v, \sigma)$ is a Gaussian kernel with standard deviation σ, and N_c is the total number of trials in class X_c. Clearly $p(v|X=c)$ is a density function because it integrates to 1 over all values of v. Therefore, we can use the Parzen window approximation in place of the true conditional density functions (which is unavailable) to estimate the mutual information. The choice of σ controls the smoothness of the probability density.

A special case of the classification problems is the binary classification problem. Because of its simplicity, many well-established theories of pattern recognition are built upon the binary classification problem. Let the two classes be $X_1=1$ and $X_2=0$. The Bayesian classification rule can be defined as

Equation 2.17

$$g^*(x) = \begin{cases} 1 & if\ P(X=1 \mid v) > 1/2 \\ 0 & otherwise \end{cases}.$$

Interestingly this simple classification rule turns out be the optimal binary classifier. Define the classification error E as

Equation 2.18

$$\begin{aligned} E &= P(\widetilde{X} \neq X) \\ &= \sum_{v} P(\widetilde{X} \neq X \mid v) P(v). \end{aligned}$$

Theorem 2.1: [Devroye 1998] Let the Bayesian classification error be E^*. That is, E^* is the error in the estimate produced by Equation 2.16, then $E^* \leq E$ for all E.

The above theorem shows that the Bayesian classifier minimizes the classification error amongst all binary classifiers. This thesis thus uses Bayesian classifier as the principal classification strategy.

Chapter 3 Characterizing spike train processes using Haar wavelet packet

3.1 Introduction

A sequence of spikes forms a *spike train*, which is often modeled as a random process [F. Rieke 1997]. It is the most widely used data type in the neuroscience community. Problems, such as neural encoding and decoding given spikes, have been studied extensively [Gabbiani and Koch 1998, Rieke 1997, Victor 1997, Strong 1998, Johnson 1996, 2001]. However, the precise characteristics of this random process are still an open question. Researchers have proposed different models to capture the statistical characteristics of spike trains while the debate over the correctness of rate coding or temporal coding of spike trains has been on going for some years [Johnson 1996, 2001, Reich 2000, Steveninck, 2002]. Here rate coding refers to the assumption that information is only conveyed in the firing rate of the spike train, and time coding refers to the assumption that precise timing of the spikes also codes information. Schemes that better characterize the firing process will help to understand the underlying neural code.

Often, the statistical behavior of a spike train is modeled as a homogeneous or inhomogeneous Poisson process. A homogeneous Poisson process is completely quantified by its mean firing rate, λ, which is equivalent to the number of spikes observed in a fixed time period [Abbott 1994, Zhang 1998, Brown 1998]. Several approaches to characterize a Poisson process have been proposed. The simplest approach is based on counting the number of spikes in a window of length T, as the probability of observing n spikes in the window is

$$p(n) = \frac{(\lambda T)^n}{n!} e^{-\lambda T}.$$

Thus, for a homogeneous Poisson process the mean and variance of the spike counts up to time T are both λT. The ratio of the variance to the mean is termed the Fano factor. A unit value of this factor can indicate the presence of a Poisson process [Rieke 1997]. However, the Fano factor only focuses on the first two moments of a spike train's statistical characterization, while discarding the remaining higher ones. One can also measure the coefficient of variation (*COV*), which is the ratio of the standard deviation to the mean of the inter-spike intervals [Gabbiani and Koch 1998]. In the case of a Poisson process, the *COV* is 1, which exemplifies one of the properties of a Poisson process: the inter-spike intervals are exponentially distributed. However, using the *COV* as a measure discards the possibility of discovering any possible patterns embedded in the spike trains [Gabbiani and Koch 1998]. Another approach is to project the auto-correlation function of a spike train onto a Fourier basis, and examine the resulting power spectral function [Gabbiani and Koch 1998]. For a Poisson process, the power spectrum should be flat everywhere except at the origin. Yet, the use of the auto-correlation function assumes by default that the underlying spike generation process is stationary. When this assumption is violated, blindly applying the power spectrum may produce artifacts in the frequency domain [Mallat 1999]. The method described in this chapter can be applied to mildly nonstationary signals.

This chapter introduces a new method to characterize spike trains based on wavelet analysis. Particularly, it examines the projection of spike train ensembles onto a Haar wavelet packet basis. If the spike generating process is stochastic by nature, the

coefficients obtained by projecting ensembles of the spike trains onto the wavelet packets are random variables themselves. The statistical properties of the projection coefficients shed light on the statistical nature of the spike train. This thesis shows that the distribution of the projection coefficients for both homogeneous and inhomogeneous Poisson processes can be well characterized. Using hypothesis testing on the coefficient statistics, one can determine if a spike train is well characterized as a homogeneous or inhomogeneous Poisson process. If the spike train is not deemed to be a Poisson process, then this method also suggests the degree of non-Poisson-ness, and also highlights the spike train's characteristic time scales at which the spike train exhibits non-Poisson behavior. To help visualize the degree of non-Poissonness at different scale, the *Poisson scale-gram* is introduced. Taken together, these analyses provide guidance for further investigations of a neural process in the case that it is significantly non-Poisson.

Furthermore, the characteristics of a spike train have important implications in the *neural decoding* context. Decoding is the task of inferring external stimulus or behavioral parameters given neural activities, or more precisely the spike trains in this thesis. If a spike train is indeed Poisson by nature, then the stochastic properties of a Poisson process suggests that mean firing rate is the only feature that carries information about the stimulus parameter [Ross 1994], in which case decoding based on the mean firing rate captures all the essential information content in the spike trains. On the other hand, if the spike trains are not Poisson, then special treatment has to be applied in order to extract the informative features embedded in the spike trains. Chapter 3 investigates the decoding problem and the feature extraction approach in depth.

Generally, wavelet-based analysis is more suitable than Fourier analysis when dealing with non-stationarity and specifically locally stationary processes [Mallat, 1998]. Power spectrum based characterization method often encounters Gibbs phenomenon in which local discontinuity of the signal produces bleeding of power into the higher frequency domain, thus creating artifacts in the spectral-gram [Mallat 1999]. By using wavelet-based methods, the spike train characterization technique presented here overcomes some of the disadvantages of the methods reviewed above. Moreover, the multi-resolution analysis feature of wavelets provides additional versatility in handling possible patterns embedded in the spike trains. In this chapter, a wavelet basis consisting of the Haar wavelet packet, which is an extension of the Haar wavelet [Wickerhauser 1994, Mallat 1999, Percival and Walden 2000], is the basis of the computational test. Some of the Haar wavelet packet's special properties, such as compactness and biologically intuitive interpretations of the projection coefficients (see Section 2.2), make it an ideal candidate for decomposing spike trains. Note that others have explored the possibility of using wavelet packets as a mean of processing spike data [Kralik 2001, Oweiss 2001, 2002]. Yet, the work in this thesis appears to be the first to use wavelet methods for formal characterization of spike trains.

This chapter is organized as follows. Section 2 analyzes the distribution of the wavelet packet projection coefficients. Particular emphasis is placed on the special cases of homogenous and inhomogeneous Poisson processes. In the case of the homogeneous process, the probabilities of the projection coefficients are obtained analytically. Finally,

in Section 4 we integrate these ideas into a methodology that characterizes spike train modeled as stochastic point processes. Several examples illustrate the main points in Section 5.

3.2 Statistics of projection coefficients

Chapter 2 reviewed the concepts underlying the construction of Haar wavelet packets, and introduced the projection coefficients arising from a binary spike train. This section investigates the statistics of these coefficients when the given firing process is a homogeneous or inhomogeneous Poisson process. Using a hypothesis testing methodology based on a χ^2-statistic applied to the coefficient distributions, one can then check if a given spike train is statistically close to a Poisson process by comparing the statistics of the projected data against the formulas derived below. This hypothesis testing approach is developed in the next section.

3.2.1 Homogeneous Poisson Process

For simplicity, let us first analyze the case of a homogeneous Poisson process with a constant firing rate λ. Poisson processes have three relevant properties:

P1. Each non-overlapping time increment of a Poisson process is independent and identically distributed with the probability, *P(.)* of a spike occurring in the interval [t,t+Δt] given by

$$P(N_{t+\Delta t} - N_t = 1) \approx \lambda \Delta t ,$$

where *N(t)* is the counting process that counts the number of spikes up to time *t*.

P2. When conditioned on a fixed number of spikes, a Poisson process uniformly distributes all the spikes in a window of length T. We can formulate this mathematically as

$$P(t' < t < t'+\Delta t \mid N = 1) = \frac{\Delta t}{T},$$

i.e. given that only 1 spike occurs somewhere in a window of length T, the probability of observing that spike in a any interval of length Δt is $\frac{\Delta t}{T}$.

P3. The probability of observing *n* spikes in a window of length *T* given the firing rate λ is

$$P(n) = \frac{(\lambda T)^n}{n!} e^{-\lambda T}.$$

Now we derive the probability distributions of wavelet packet coefficients generated by the projection of an ensemble of spike trains that arises from a homogeneous Poisson process with fixed firing rate λ onto the Haar wavelet packet. First, notice that the resulting projection coefficients are integer valued because the Haar wavelet packets are functions that assume the value -1 and 1 only; and the spike trains are similarly binary valued. Also, recall from Equation 2.2 that the integrals of wavelet packet functions at all scales are 0. This symmetry of the wavelet packet, when coupled with property P2, implies that when a single spike is projected onto the support of a wavelet packet function, the probabilities of the resulting coefficient being 1 or -1 are the same, namely ½. Based on this observation, we can write the conditional probabilities of the projection coefficients as follows: given *N* spikes in a window of length *T*,

$$P(v = N - 2n \mid N) = \left(\frac{1}{2}\right)^N \binom{N}{n}, \quad n = 0,1,\ldots,N$$

where $P(v = k \mid N)$ is the probability that coefficient *v* takes the integer value *k* when *N* spikes occur in the support of the wavelet packet function associated with coefficient ν. In addition, we can write

$$P(v) = \sum_N P(v, N) = \sum_N P(v \mid N) P(N),$$

where *P(N)* is the probability of finding *N* spikes in the time interval of length *T*, expressed by property P3. Thus, the probability of observing a projection coefficient of integer value *n* is

Equation 3.1 $$P(v = n) = \sum_{N=0}^{\infty} \left(\frac{1}{2}\right)^{2N} \binom{2N}{N + n/2} \frac{\lambda T^{2N}}{(2N)!} e^{-\lambda T}, \quad \textbf{if n is even}$$

Equation 3.2 $$P(v = n) = \sum_{N=0}^{\infty} \left(\frac{1}{2}\right)^{2N} \binom{2N}{N + \frac{n+1}{2}} \frac{\lambda T^{2N}}{(2N)!} e^{-\lambda T}, \quad \textbf{if n is odd.}$$

The above analysis offers the theoretical distributions for wavelet packet coefficients that result from an ensemble of spike trains arising from a given a homogeneous Poisson process with constant firing rate λ. In practice, spike trains are sampled discretely. Let the finest sampling resolution be δT. For such discretely sampled data, the probability distributions given above become approximations that only work well when the finest sampling period, δT, is sufficiently small as compared to the length of the sampling window T. In other words, property P2 is approximated in practice because the probability distribution of *N* spikes conditioned on *N* is only uniform when δT is infinitesimally small, which is not possible in actual applications. To better understand this subtlety, consider the simple case where two spikes are to be placed in a sampling window that is subdivided into two sampling periods, Δt_1 and Δt_2. If one spike is placed

in the interval Δt_1 with probability ½, then the second spike has to reside in Δt_2 with probability 1. Therefore, we see that the approximation breaks down in this case. In the next section, where the more general case of inhomogeneous Poisson processes are considered, I propose a computational approach that approximates those probabilities so that they are not susceptible to discretization errors. In addition, the computational approach can be generalized to inhomogeneous Poisson processes. The theoretical derivations of this section provide a standard against which we can check our computational theory in the simple case of a purely homogeneous Poisson process.

3.2.2 Inhomogeneous Poisson Process

An inhomogeneous Poisson process is a Poisson process with a variable firing rate λ(t). Even though it's not stationary like a homogeneous Poisson process, it retains the same memoryless property, P2, namely that disjoint increments of an inhomogeneous Poisson process are independent.

Due to the variable firing rate, the approach outlined in the previous section becomes unfeasible for inhomogeneous Poisson processes because the probability of observing *n* spikes in an interval of duration T is now a combinatorial problem that depends on the cardinality of the different firing rates present in this interval. Fortunately, a simpler alternative to the computation of the coefficient distributions exists by utilizing the Pyramid Algorithm and the memory-less property of an inhomogeneous Poisson process. Recall that an inhomogeneous Poisson process has independent disjoint increments, i.e.,

$$P(v_{0,k}, v_{0,k+1}) = P(v_{0,k})P(v_{0,k+1}),$$

where,

Equation 3.3 $$P(v_{0,k} = 0) = e^{-\lambda_k \Delta T}$$

Equation 3.4 $$P(v_{0,k} = 1) \approx 1 - e^{-\lambda_k \Delta T},$$

where that $v_{0,k}$ is the 0^{th} level wavelet packet projection of the point process at location k. It is a random variable indicating whether a spike is present in the k^{th} time increment. Equation 3.3 is the direct result of property P3, while Equation 3.4 is a reasonable approximation when the time interval ΔT is small. Also recall that the Pyramid Algorithm for the Haar wavelet consists of a low-pass filter $\{h_k\}$ with coefficients {1 1} and a high-pass filter $\{g_k\}$ with coefficients {1 -1}. Therefore, by applying the pyramid algorithm to the inhomogeneous Poisson process at the finest scale ($j=1$), we obtain new random variables of the form

$$\begin{aligned} v_{1,k} &= v_{0,2k-1} + v_{0,2k} \\ v_{1,k+\frac{T}{2}} &= v_{0,2k-1} - v_{0,2k} \end{aligned}, \text{ for } k = 1,2,...,\frac{T}{2} \quad .$$

The following proposition illustrates the independence of these wavelet packet coefficients.

Proposition 3.1: For a given homogeneous or inhomogeneous Poisson process, the wavelet packet coefficients contained in any node of the wavelet packet tree, namely $\{v_{jk}\}_{k=1+lT/2^j}^{(l+1)T/2^j}$, $l = 0,1,...,2^j - 1$, are independent. $\{v_{jk}\}_{k=1+lT/2^j}^{(l+1)T/2^j}$ is the set of wavelet packet coefficients in the j^{th} scale and l^{th} node of the wavelet packet tree. Once again, the index j and k are reserved as the scale and location index. T is

the length of the spike train in multiples of δt. And l indexes the nodes at a particular scale.

The proof of this proposition can be found in Appendix 1.

Based on the structural independence established by Proposition 3.1, the respective probabilities of the coefficients $v_{l,j}$ then become

Equation 3.5 $$P(v_{1,k} = v) = \sum_n P_{v_{0,2k-1}}(n) P_{v_{0,2k}}(v-n) \qquad \textbf{if } k \le T/2$$

Equation 3.6 $$P(v_{1,k} = v') = \sum_n P_{v_{0,2k-1}}(n) P_{v_{0,k+2k}}(v'+n) \qquad \textit{otherwise},$$

which are the convolutions between the probabilities of the parent random variables $v_{0,k}$ and $v_{0,k+1}$, a consequence of the above proposition.

The above equations can be extended to the wavelet packet coefficients at any scale. For consistency we keep the same notation. We define the random variable obtained through the wavelet packet projection at scale j position k as v_{jk}. Then by the Pyramid Algorithm,

$$v_{j,k} = v_{j-1,k'} + v_{j-1,k'+1}, \text{ if } \underline{\underline{k/2^{N-j}}} \text{ even}$$

$$v_{j,k} = v_{j-1,k'} - v_{j-1,k'+1}, \text{ if } \underline{\underline{k/2^{N-j}}} \text{ odd}$$

where $\underline{\underline{x}}$ is the *floor* operation that takes x to its nearest integer from below, and k' indexes the parent nodes of k^{th} node. And the corresponding probabilities can be described using the convolutions,

Equation 3.7 $$P(v_{j,k} = v) = \sum_n P(v_{j-1,k'} = n)P(v_{j-1,k'+1} = v - n)\text{, if } \underline{\underline{k/2^{N-j}}} \text{ is even}$$

Equation 3.8 $$P(v_{j,k} = v') = \sum_n P(v_{j-1,k'} = n)P(v_{j-1,k'+1} = v' + n)\text{, if } \underline{\underline{k/2^{N-j}}} \text{ is odd.}$$

Thus, the probabilities of the projection coefficients of an inhomogeneous Poisson process at any scale and position can be calculated using the above equations. Equation 3.3 and Equation 3.4 form the initial conditions for the algorithm.

3.3 A Computational Test for Poisson Processes

Based on the results derived above, this section develops a novel method to characterize the *Poisson-ness* of an unknown stochastic point process. If the underlying process is indeed Poisson, then the method will successfully conclude so; otherwise, it will label the scales and locations where the given process deviates from a Poisson process. As discussed below and as shown in the examples, the knowledge of these deviations can be used to further characterize the spike train process. Following Section 2.2, we assume that a spike train is described by a *T*-dimensional vector $S^i = \{s_0^i,...,s_{T-1}^i\}$, and

$$s_k^i = \begin{cases} 1 & \textit{if there exists a spike in } [k\delta T,(k+1)\delta T] \\ 0 & \textit{otherwise} \end{cases}$$

where *k=0,...,T-1* and the superscript *i* indexes the i^{th} observed spike train in an ensemble of spike trains.

Our approach is based on a classical hypothesis testing paradigm applied to the coefficient distributions. First, we claim a null hypothesis stating that the given point process is indeed Poisson. To carry out the hypothesis test, as a first step the rate

function λ_k, $k=0,\ldots,T-1$ must be estimated from the spike train ensembles. Note that the estimation of λ is itself an active research area [Donoho 1994, Kolaczyk 1997, Nowak 1999] This paper adopts the wavelet thresholding method proposed by Donoho to estimate $\lambda(t)$ from the spike trains. For completeness, the algorithm and its properties are briefly reviewed. First we average the spike train ensemble over all the realizations i to obtain a noisy estimation of the rate function at each time step k,

$$\lambda_k = \frac{1}{M\delta T}\sum_{i=1}^{L} s_k^i$$

where L is the total number of spike trains of the ensemble. This computation effectively estimates the firing rate at each sampling interval at length δT. Likewise, the standard deviation of the rate function at each k can be estimated as

$$\sigma_k = \sqrt{\sum_{i=1}^{L} \frac{[\frac{s_k^i}{\delta T} - \lambda_k]^2}{L-1}}.$$

Because of the Central Limit Theorem, λ_k is asymptotically normally distributed for each k when L approaches infinity. Therefore, we can scale the noisy rate function at each time step by the quotient between $\sqrt{L}$ and the estimated standard deviation, σ_k, to produce a scaled noisy rate function at each k,

$$\lambda_k^{ns} = \lambda_k \frac{\sqrt{L}}{\sigma_k},$$

note that λ_k^{ns} is normally distributed with variance 1 at each k again because of the Central Limit Theorem. Now decompose the T-dimensional vector λ_k^{ns} into wavelet coefficients, α_{jk}, using the Pyramid Algorithm described earlier

$$\alpha_{jk} = \sum_{l=0}^{T-1} \lambda_l^{ns} \psi_{jk}^{db}(l).$$

The family of wavelet functions, ψ_{jk} of choice here is Daubechie's 4 wavelet (DB4) [Percival 2001]. Note other wavelet built for de-noising also works in this context. Following Donoho (1994), we threshold the wavelet coefficients using a threshold value

$$\varepsilon = \sqrt{\frac{2\log(T)}{T}}.$$

The thresholding rule is the so-called soft threshold, where the coefficients α_{jk}^* are adjusted by the rule

$$\alpha_{jk}^* = \begin{cases} sign(\alpha_{jk})\left|\alpha_{jk} - \varepsilon\right| & if \quad \left|\alpha_{jk}\right| > \varepsilon \\ 0 & otherwise \end{cases}.$$

Finally, we invert the thresholded wavelet coefficients to recover the de-noised rate function $\lambda=\{\lambda_k, k=0,...,T-1\}$ using the following inversion formula:

$$\lambda = \sum_{jk} \alpha_{jk}^* \psi_{jk}^{db}(t).$$

Certainly the robustness of the rate estimation process will affect any further analysis on the Poisson nature of the spike train. However, as we will see below, the effect of rate function estimation error vanishes exponentially with respect to the amount of data in this characterization method.

Given the estimated rate function, the theoretical probabilities of each wavelet packet coefficient can then be derived, i.e., the distribution of the projection coefficients under the hypothesis that the process is an inhomogeneous Poisson process with rate function $\lambda(t) = \{\lambda_k\}$, $k=0,...,T-1$. Again, because the rate function λ is a T-dimensional vector

with $\{\lambda_k\}$, $k=0,\ldots,T-1$, the theoretical probabilities of the wavelet packet projection coefficients are computed as

$$P^*(v_{0,k}=0)=e^{-\lambda_k \delta T}$$

$$P^*(v_{0,k}=1)\approx 1-e^{-\lambda_k \delta T}$$

and

$$P^*(v_{j,k}=v)=\sum_n P^*(v_{j+1,k'}=n)P^*(v_{j+1,k'+1}=v-n)$$

$$P^*(v_{j,k}=v')=\sum_n P^*(v_{j+1,k'}=n)P^*(v_{j+1,k'+1}=v'+n)$$

The notation P^* represents the theoretical probability distribution given the spike generation process is indeed Poisson with the above estimated firing rate function, $\lambda(t)$. Notice that the uncertainty associated with the *seed* probability $P^*(v_{0k})$ is

$$\Delta P^* \approx e^{-(\lambda_k \pm \varepsilon)\delta T},$$

where ε is proportional to the standard deviation of λ_k and to $1/\sqrt{L}$, the cardinality of the ensemble. The error on the P^* therefore is

$$E=e^{-\lambda \delta T}\left|1-e^{\mp \varepsilon \delta T}\right|,$$

which approaches *0* exponentially fast as the number of available data sets, L increases. Hence, errors in the estimation error of λ_k have little effect on the estimated coefficient probability distributions as L increases.

Meanwhile, one can also compute the respective empirical probabilities of all the wavelet packet coefficients, $P(v_{jk})$ from the data sets. Under the null hypothesis, the empirical probabilities will match the hypothesized probabilities; otherwise, they will be significantly different, indicating that the process is not Poisson. To assess the

significance of the differences between the coefficient distributions of the idealized Poisson model and the experimental data, we apply the χ^2-statistic. The χ^2 variate is calculated as following

$$\chi^2_{jk} = \sum_{v=v_1}^{v_M} \frac{[P^*(v_{jk} = v) - P(v_{jk} = v)]^2}{P^*(v_{jk})},$$

where the summation is over all possible values of the random variable v_{jk}. Because the sample space of v_{jk} has cardinality M depending on the scale j, the degree of freedom (DOF) of the χ^2 variate is $M-1$. For example, when $j = 1$, $M = 3$ since v_{1k} can only equal $\{0, 1, 2\}$ for the case $k=0...T/2-1$ and {-1, 0, 1} for the case $k = T/2...T-1$. Thus, the DOF both of cases is 2. Using the χ^2 and *DOF* pair, we can finally infer a *p*-value that signifies the difference between the empirical probability and that coming from the ideal Poisson process. In this paper, a *p*-value that is greater than *0.95* signals a statistically significant discrepancy between the two. Note that studies on the χ^2-statistics suggest the minimal number of observations required for a reliable test is 20 [Greenwood 1996].

For a true Poisson process, we expect the *p*-values to remain small for all the wavelet packet coefficients at any given j and k. However, when the *p*-values exceed 0.95 at one or more scales, we can no longer conclude having a Poisson process at hand. To address this case, we examine the number of wavelet packet coefficients that are significantly different from its Poisson counterpart. For a fixed scale j^*, we first identify all the wavelet packet coefficients with large *p*-values. Because the comparison is made against a process with independent increments, the large p-values suggest that correlations exist in the spike train on the scale of j^*. To quantify the level of correlation, we introduce η_j

Equation 3.9

$$\eta_{j^*} = \frac{\#\{v_{j^*k} \mid p \cdot value(v_{j^*k}) > 0.95\}}{T},$$

where T is the length of the spike train, i.e., the same as the number of wavelet packet functions at a given scale. η_j marks the fraction of all the wavelet packet coefficients at scale j that exhibits correlation. If η_j is small, then the correlation at that scale is minimal, in which case we may label the process as *approximately Poisson* at that scale; else if η_j is large, the process is deemed to be *non-Poisson* at that scale. When a given scale is *non-Poisson*, it may be desirable to further investigate the dependence between the wavelet packet coefficients residing in that scale in order to fully understand the spike train process. In Section 3.4 we introduce the *Poisson scale-gram* as a simple graphical technique to represent the non-Poissonness of a neural process.

3.4 Examples

To illustrate the utility of our approach, and to additionally show how the method can be used to characterize spike trains, this section applies the methods described in the previous sections to different data sets. In order to have a concrete understanding of the ideas presented in Section 3.2, we first give an example of the coefficients' distribution when the underlying process is either a homogeneous or an inhomogeneous Poisson process. Next we apply the spike characterization method outlined in Section 3.3 to a number of different simulated and actual neural processes. The empirical distributions throughout this section are computed using the histogram method.

Moreover the surrogate data used to produce the histograms in the simulation examples below are generated using the following simple technique. For each *1*ms window, we compute the probability of not observing a spike as

$$P(s_k = 0) = e^{-\lambda_k 0.001}$$

and observing a spike as

$$P(s_k = 1) \approx 1 - e^{-\lambda_k 0.001}.$$

Now we generate a uniform random number *r* using a generic random number generator. If $r>P(s_k=0)$, we register a *1* at time *k* in the artificial spike train; otherwise, we register a *0* at time *k*. Thus, using this method we can generate spike trains of any given length that model a Poisson process with rate function $\{\lambda_k\}$.

Example 1: The Coefficient Distributions of Poisson Processes

Before applying the characterizing method directly, we first study the distributions of the projection coefficients in the case of idealized Poisson processes. As will be seen, the nature of the coefficient distributions can shed light on the nature of the underlying process. Consider the following three cases: 1) a homogeneous Poisson processes whose constant firing rate is λ=20Hz; 2) an inhomogeneous Poisson process whose firing rate function is a concatenation of two homogeneous Poisson processes, i.e., a Poisson process with an abrupt change in firing rate

$$\lambda(t) = \begin{cases} 10 & t \le 256 \\ 20 & t > 256 \end{cases};$$

and 3) an inhomogeneous Poisson process with a linear firing rate function

$$\lambda(t) = mt + b,$$

where $m = 1$ and $b = 1$. In all three cases, the sampling interval δT is 1ms and the length of the artificial spike train T is 512ms. Figure 3.1 displays the selected wavelet packet projection coefficients for all three cases. The theoretical distributions were obtained from the formulas derived above, while the "empirical" distributions were obtained using the method described above to simulate a Poisson process. Each ensemble contains 2000 spike trains. The close match between the theoretical values of the distributions and the values obtained from the simulations confirms the theoretical calculations of Section 3.3.

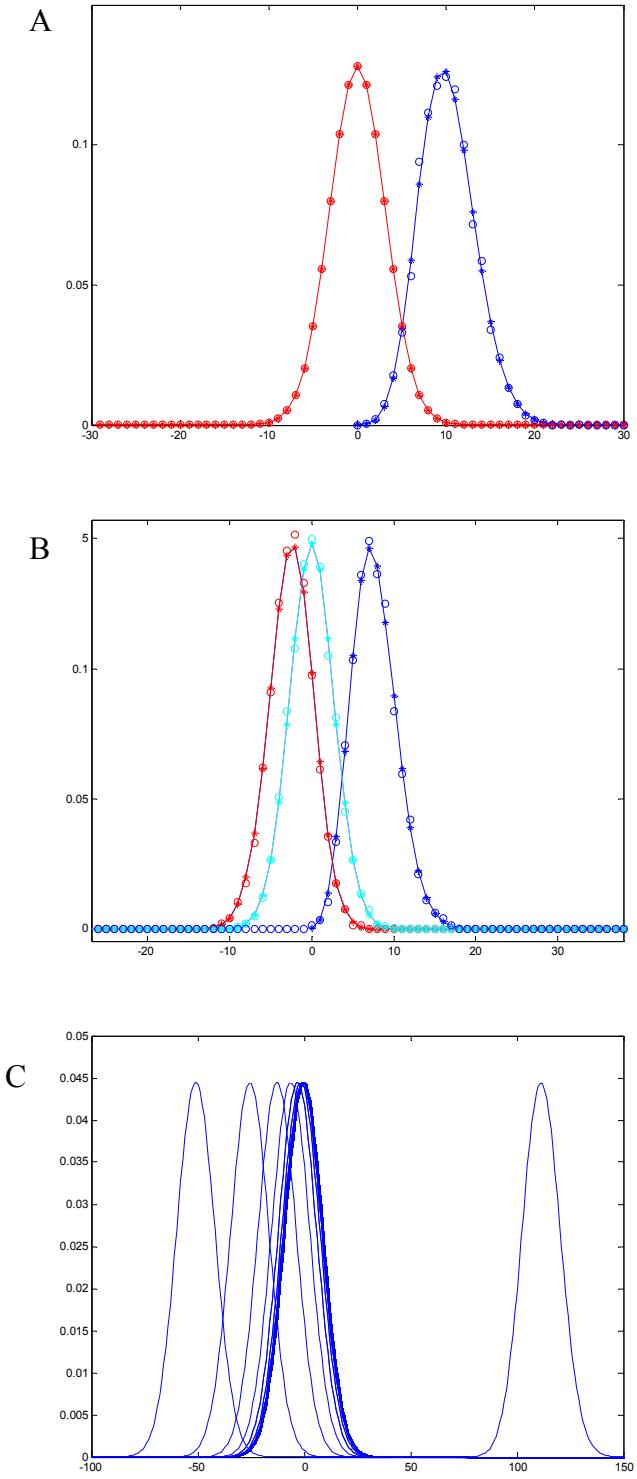

Figure 3-1 Distribution of wavelet packet projection coefficients of Poisson processes

A) Homogeneous Poisson process with constant firing rate 20Hz. The blue curve connects the discrete probability of coefficient v_{90} at different values. It corresponds to the mean firing rate over

the whole window. The red curve corresponds to the coefficients v_{9k}, $k=1,\ldots,511$. The theoretical probabilities value are shown in circles *'o'* and the empirical values are indicated by '*'. B) Inhomogeneous Poisson process with a step firing rate. The blue curve connects the discrete probability of coefficient v_{90} at different values, the red curve corresponds to the coefficient v_{91}, and the cyan curve relates to the coefficients v_{9k}, $k=2,\ldots,511$. C) Inhomogeneous Poisson process with a linearly increasing firing rate. The probability distributions for coefficients v_{9k}, $k=0,\ldots,511$ are shown. In all the figures *x*-axis marks the value of the coefficient and *y*-axis indexes the corresponding probabilities.

Notice that for the homogeneous Poisson process, the coefficient distributions at all locations ($k= 2,\ldots,128$) at scale $j=9$ are identical. This agrees with our analysis in Section 4. Additionally, the coefficient distributions resemble a zero-mean Gaussian distribution because of the Central Limit Theorem, which states that the distribution of the sum of independent random variables asymptotically approaches a Gaussian distribution [S. Ross 1994]. As seen in Figure 3.1B, for the inhomogeneous Poisson process with step firing rate function, only the first two coefficients ($k=0,1$) have associated distributions whose centers are not at zero. This arises because the support of these two wavelet packets straddles the point of rate discontinuity. All the remaining wavelet packet functions ($k=2,..,511$) have associated coefficients that sum to 0 over the two half-windows in which the two homogeneous Poisson processes reside, i.e.

$$\sum_{t=1}^{256} \psi_{9k}(t) = \sum_{t=257}^{512} \psi_{9k}(t) = 0 \qquad k = 2,..,511\,,$$

by the construction of the Haar wavelet packet reviewed in Section 2.2. Thus, their projection coefficients have zero-centered distributions. More generally, *a non-zero-centered distribution is an indication of a firing rate change in the support interval of the associated wavelet packet.* Finally, we observe that the distributions of the wavelet packet coefficients for the inhomogeneous process with linearly increasing rate are more complex and span a wide range of centers because the rate function $\lambda(t)$ differs

substantially from a constant. Therefore, we see that increasing complexity in the firing rate function leads to increasingly complicated coefficient distributions.

Example 2: An Inhomogeneous Poisson Process

Next the characterizing procedure described in Section 3.4 is applied to a known inhomogeneous Poisson process with rate function $\lambda(t) = A\sin(4\pi\frac{t}{T}) + B$, where A is 10 Hz, B is 15 Hz, and T is 512 ms. The surrogate data are generated using the aforementioned numerical method. Both the actual and estimated rate functions are plotted in Figure 3-2. The estimation of the rate function is carried out using the soft-thresholding method presented in Section 3.3.

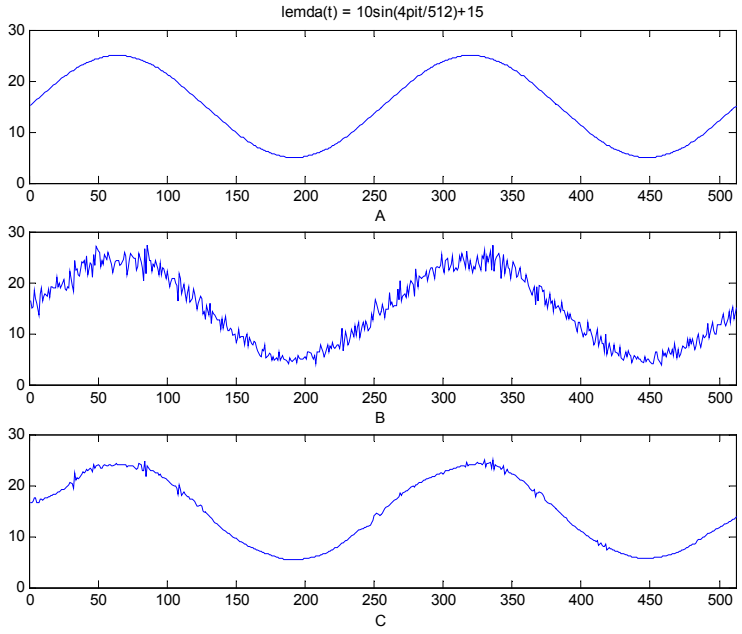

Figure 3-2 Actual and estimated firing rate function with length *T* being 512 ms.

A) The actual firing rate function, B) The noisy estimation of the firing rate by averaging the spike trains, C) The denoised estimation of the firing rate function using soft-thresholding with Daubechies 4 wavelet family. X-axis is the time in millisecond and y axis is the frequency on the firing rate function in Herz.

At each level, the number of coefficients that are significantly different from a Poisson process (P>0.95), η_j, in terms of percentage of all the wavelet packet coefficients at that scale (*T=512* in this case) summarized in Table 3.1. For a true Poisson process, the coefficient distributions at all scales indeed match well with an idealized Poisson process.

	WP1	WP2	WP3	WP4	WP5	WP6	WP7	WP8	WP9
Inhomogeneous Poisson Process	0.39%	1.95%	1.95%	1.56%	0.39%	0%	0.2%	0.39%	0%

Table 3.1 Percentage of wavelet packet coefficients that is different from an ideal Poisson process for the simulated system of Figure 3.2.

Example 3: Algorithm Performance on a Cyclic Poisson Process

We next show how our method can pick up potential correlations in spike train data that can be missed by traditional COV techniques. A *cyclic Poisson process* can be created from the simulated data of the last inhomogeneous Poisson process example as follows. Copy a portion of a spike train from an interval $[t_1,t_2]$, and replace a portion of the same spike train with this copy starting at a point that is one period away, i.e.

$$s(t) = s(t - \frac{T}{2}) \ , \ \text{for } \frac{T}{2} \le t_1 \le t \le t_2 \le T \ ,$$

where *s(t)* is the spike train signal, and where t_1 and t_2 bound the width of the replaced data. A cyclic Poisson process is not strictly a Poisson process when considered at the time scale T, as it violates the independent increments property. To test the effectiveness of our procedure, we constructed cyclic Poisson processes with different repetitive widths: $\Delta t = t_2 - t_1 = 32,\ 64,\ 96$ msec when the simulated Poisson spike train is of

length 512ms, with the sampling interval being 1ms. Figure 3.3 illustrates a graphical example of the construction of the cyclic Poisson process.

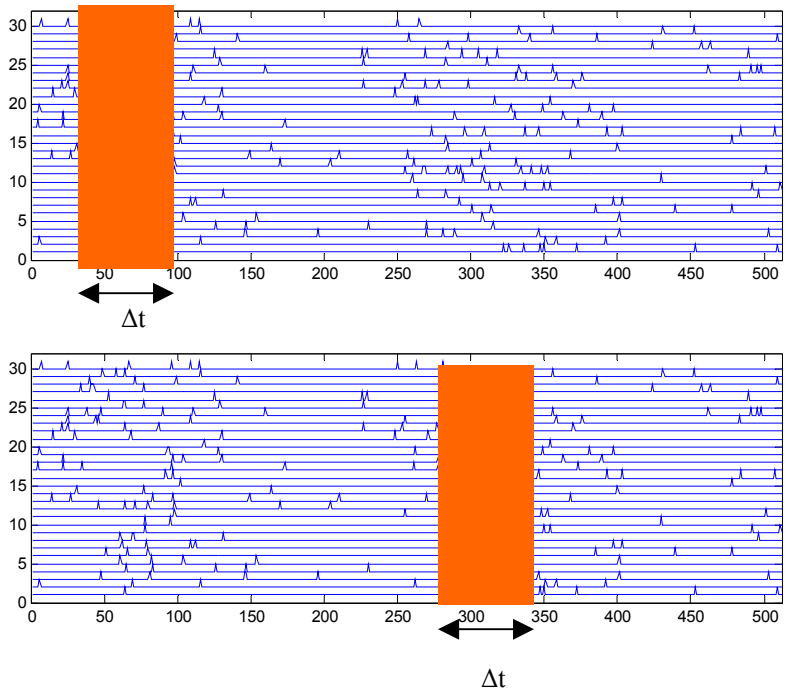

Figure 3-3 Construction of cyclic Poisson spike trains.

A) The original inhomogeneous spike trains. The shadowed region, a window of length 64 ms, is copied. B) The copied portion of the data is then inserted and replaces the stretch of data 256 ms downstream. *X*-axis is the time in ms and *y*-axis marks the trial number.

The resulting numbers of significantly non-Poisson wavelet packet coefficients (P>0.95), η_j in terms of percentage over all wavelet packet coefficients at that scale (512 in this case) are summarized in Table 3.2.

	WP1	WP2	WP3	WP4	WP5	WP6	WP7	WP8	WP9
Cyclic Poisson Process 1 $\Delta t = 32$	0.39%	1.95%	2.34%	1.37%	0.2%	0%	0.39%	0.2%	1.95%
Cyclic Poisson Process 2 $\Delta t = 64$	0.39%	1.76%	2.34%	1.37%	0.2%	0%	0.2%	0.39%	100%

Cyclic Poisson Process 3 $\Delta t = 96$	0.39%	1.76%	2.34%	1.56%	0.2%	0%	0.78%	0.39%	100%

Table 3.2 Percentage of wavelet packet coefficients that are significantly different (P>0.95) from a Poisson process, η

For each scale *j*, the numbers of wavelet packet coefficients that are significantly different from the ones generated by a Poisson process are first counted, where the significance test is the proposed χ^2 test. There are a total of 512 wavelet packet coefficients for each *j*, thus the percentage is calculated as η=#{*significant*}/512.

Note that at scale $j=9$ (where the interval of support spans the entire 512 length cycle), the number of significantly non-Poisson wavelet packet coefficients increases dramatically as the length of the *repetition window* (the section of data copied and pasted) Δt increases. An intuitive explanation is that the length of the repetition window is proportional to the non-Poisson characteristics introduced in the process. In addition, η_j at $j=1,\ldots,8$ remains steadily small for all the experiments because all wavelet packet functions at these scales have supports that are too short to simultaneously cover the two identical stretches of data. Therefore, for scales $j=1,\ldots,8$ the process appears Poisson while at scale $j=9$, our method suggests that the data are not really Poisson due to the correlations in the data that violate the independent increment assumption. On the other hand, the COV analysis returns 1 for the cyclic Poisson processes because the repetition in spike trains does not alter the inter-spike interval distribution.

Example 4: The Brandman and Nelson Non-renewal Model

We also apply the Poisson test to a known non-renewal process. Brandman and Nelson (2002) proposed an adaptive linear threshold model neuronal firing model that generates spike trains with non-renewal, specifically long-term regularization, properties. The model has three parameters a, b, and σ, with a being proportional to the firing rate, and

σ/b being proportional to the COV as well as the scale of regularization. Here we generate spike trains of 512 unit times with $a=30$, $\sigma=1$ and $b \in [0.1,1]$. The fractions of non-Poisson coefficients, η_j, determined by our technique are summarized in Table 3.3. The total number of wavelet packet coefficients in this case is also 512 because the data string is of the same length.

	WP1	WP2	WP3	WP4	WP5	WP6	WP7	WP8	WP9
Nelson1 ($b=1$)	0%	5.86%	72.9%	100%	100%	94.9%	45.9%	1.95%	1.37%
Nelson2 ($b=0.5$)	0%	0.79%	6.84%	63.9%	95.3%	4.88%	0.98%	0.79%	0.59%
Nelson3 ($b=0.25$)	0.2%	0.39%	1.56%	2.73%	3.32%	1.56%	0.79%	0.39%	0.39%
Nelson4 ($b=0.1$)	0.2%	0.59%	1.76%	0.39%	0.59%	0%	0.39%	0.39%	0.2%

Table 3.3 Percentage of significantly non-Poisson wavelet packet coefficients at each scale, η_j Significant is determined by the proposed χ^2 test. There are a total of 512 wavelet packet coefficients for each j, thus the percentage is calculated as #{significant}/512. Brandman and Nelson (2002) model is used to generate the test spike trains; $a=30$, $\sigma=1$, and $b=1, 0.5, 0.25, 0.1$.

As b decreases, the scale of regularization increases [Brandman & Nelson 2002]. In another words, locally in time the spike trains become more Poisson-like as b decreases. Therefore, with $b=1$, the scale regularization is small, which means most of the wavelet packet coefficients at smaller scales would exhibit non-Poisson characteristics. As b decreases, this effect becomes less influential and spike trains would resemble Poisson processes when viewed at a short time scale. Table 2 validates the above argument as we observe large numbers of significantly non-Poisson wavelet packet coefficients when b is large. We notice as b decreases, η_j also decreases at each scale j, signaling that the process becomes more and more Poisson-like.

Example 5: Characterizing Monkey Parietal Reach Region Neuronal Spike Trains (the Poisson Scale-gram)

Signals from fifteen neurons were recorded in this experimental setting, each with 2 different reach conditions. Thus, we have a total of 30 distinct spike processes. The number of spike train trials available for analysis ranges from 25 to 144 for each of the 30 conditions. Without loss of generality, we focus on a particular 512ms window which occurs 400ms after the cue onset [Shenoy 2003]. Since the spike train is sampled at 1ms, the processed spike data is a 512 point binary string with a unit value at the estimated times of spike onsets, and zero otherwise. The values of η_j, $j=1,\ldots,9$ obtained by applying our procedure are summarized in Figure 3.4.

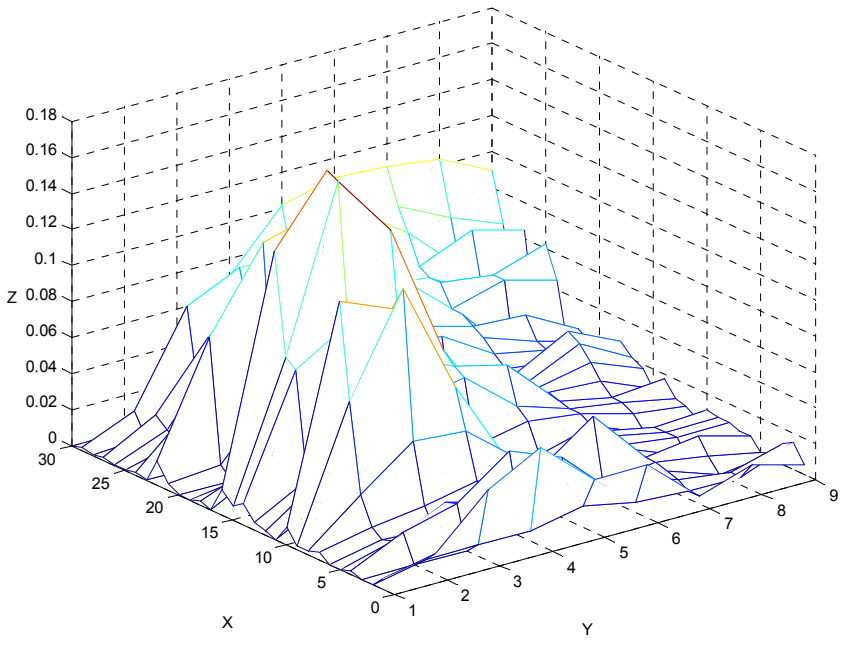

Figure 3-4 Fraction of significantly non-Poisson wavelet packet coefficients, η_j for the 30 neuronal/behavioral combinations from PRR recordings

The *X*-axis indexes the behavior/neuron combination, the *Y*-axis indexes the wavelet packet scale, and the *Z*-axis marks the value of η_j. A true Poisson process would return near-0 η_j at all scales *j*.

The figure shows that of the 30 processes, about 1/3 displays characteristics that resemble Poisson processes, i.e. η_j is small for all j. Another 1/3 displays small-scale non-Poisson properties, i.e. on a short time scale (~8 ms) $j=1,...,3$, the spike trains contain correlations that give rise to large p-values. The remaining 1/3 of the recorded neurons have mid to large scale non-Poisson properties, which mean the spike trains have dependent structures over longer time periods (~100-200 ms), $j=4,...,9$.

The Poisson Scale-gram.

More generally, the Poisson or non-Poisson characteristics of a spike train process can be conveniently depicted by the *Poisson Scale-gram*. In this visualization scheme, each pixel in a grid of $\log_2 T \times T$ pixels is associated with a specific wavelet packet coefficient. That is, the pixel in the (j,k) grid location represents the p-value of v_{jk}. The p-values of the coefficients at scales $j = 1,...,n$ (where $n=9$ for the data set under discussion) are color-coded. At the 0^{th} scale, the horizontal axis (or location index, k) can be directly associated with time in the spike train. At larger scales, the horizontal axis is still time-like, but with time smeared across increasingly larger windows while finer frequency resolutions are introduced. Along the vertical axis, the wavelet scale increases in the downward direction. Analogously, the characteristic time scale (frequency) increases (decreases) in the downward direction. Graphically, the following figure (Figure 3.5) illustrates the main idea.

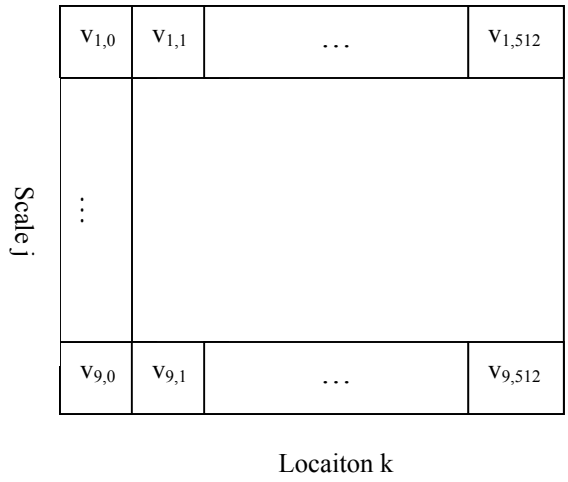

Figure 3.5 Illustration of the Poisson Scale-gram

Each pixel represents the p-value of the χ^2 variate associated with the wavelet coefficient v_{jk}. The scale *j* decreases from *1* to $log_2 T$, and the location *k* increases from *0* to *T-1*. There are a total of $T\log_2 T$ pixels in the image. At the smaller scales, the location index k is strongly related to time increments. But at larger scales, the temporal resolution is traded off by the frequency resolution, as k indexes frequency increments.

We have chosen a color scale based on blue being a 0 p-value (not significantly different from a Poisson process) and red being the p-value of 1 (significantly different from a Poisson process). In the case of an ideal Poisson process, the *Scale-gram* should display dark blue color at every pixel.

For the same PRR neurons presented earlier, the associated p-value color is plotted in Figure 3.6 for the coefficient at all available scale *j* and location *k*..

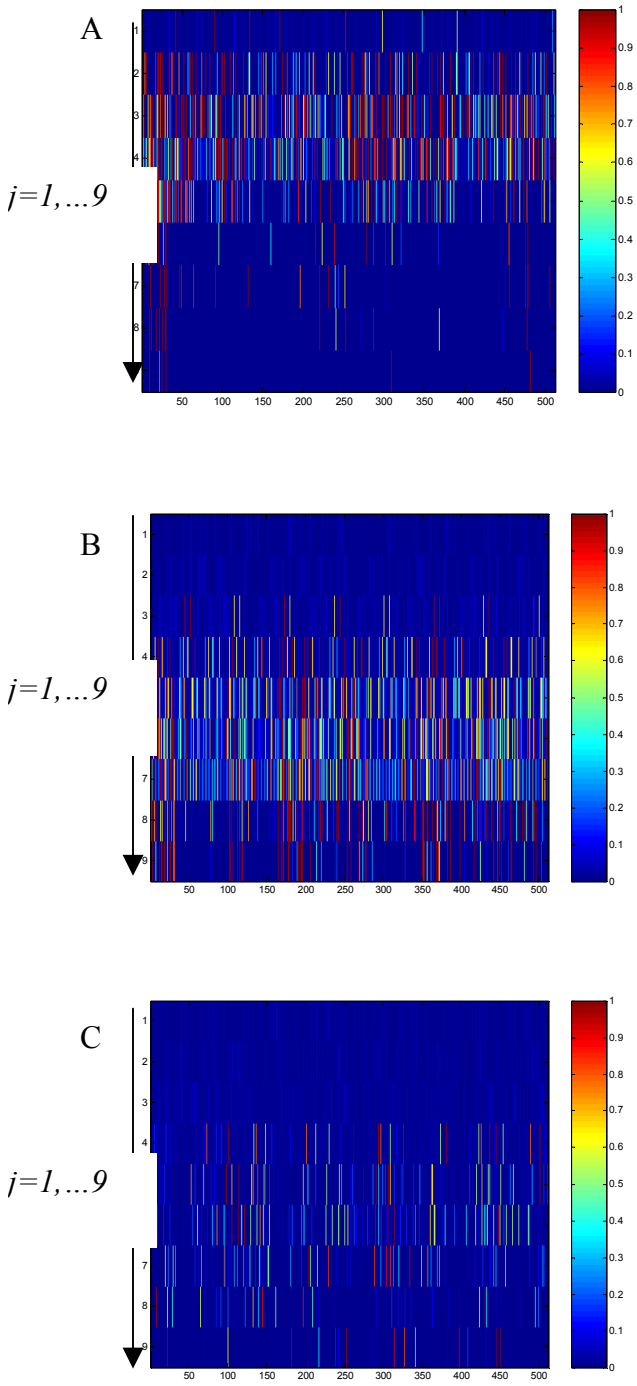

Figure 3-6. ***Poisson Scale-grams:*** **Images of the P-values at different scales.**

The color bar indicates the *P*-value with red being 1 (significantly different from Poisson) and blue being 0 (not different from Poisson). The Y-axis indexes the wavelet packet scales, *j=1,..,9*, and the X-axis indexes the 512 wavelet packet coefficients (or locations) at each scale.

A) *P*-values from a neuron/behavior condition with dominant short-scale non-Poisson characteristics. Most of the large P-values are concentrated at small scales, j = 1,...,3. B) *P*-values from a

neuron/behavior condition with dominant mid to large-scale non-Poisson characteristics. Most of the large P-values are concentrated at scales, j = 5,...,8. C) *P*-values from a neuron/behavior condition with relatively little non-Poisson characteristics. Most of the *P*-values at different scales are small.

It plots the Poisson scale-gram for one neuron/behavior combination that is representative of the three types of behavior that we found in this set of PRR neurons. Evidently, different neuron displays different characteristics on the Poisson *Scale-gram*. Some resembles a Poisson process on a shorter time scale (10 ms); some have longer time Poisson characteristics (200ms); others are Poisson over all time scales. This can be completely captured by the Poisson Scale-gram as shown in Figure 3.7.

3.5 Conclusion

Understanding the statistical nature of a neuron's spike generating processes is a crucial step towards better understanding of the underlying neural code and constructing more reliable neural controlled devices. In this chapter, a technique is proposed such that the Haar wavelet packet projection is used to characterize the spike firing process because the Haar wavelet packet carries some interesting properties that are particularly suitable for strings of binary data. This approach, which is analogous to the *Pyramid Algorithm*, computes the probabilities of wavelet packet projections given either homogeneous or inhomogeneous Poisson process. Then it characterizes a spike train process by comparing its wavelet packet coefficients' probability distributions to the distributions of a Poisson process with identical rate function. If the underlying process is indeed Poisson, then the coefficients have distributions very close to its Poisson counterpart; otherwise, significant deviation may be observed. Moreover, a *Poisson scale-gram*

(visualization method) is presented so that extra insight about the process' scale of Poisson-ness can be investigated. It allows us to infer the *Poisson-ness* of the process by assessing at which scale it resembles a Poisson process. This chapter concludes with several applications of the technique to both surrogate data and actual spike data from PRR.

Chapter 4 Decoding Reach Direction Using Wavelet Packet

4.1 Introduction

In Chapter 1, we defined decoding as the task of inferring or estimating external stimuli or behavioral states from neural signals [Abbot 1994, Rieke 1997]. Depending on the specific problem at hand, the technical approaches to the decoding problem may vary substantially. In one class of problems, a continuous stimulus parameter must be decoded. In these cases, functional approximation techniques are exploited [Rieke 1997, Brown 1998, Frank 2000]. At the other end of the spectrum lies the problem of decoding discrete stimuli. For such problems, pattern recognition methods are employed frequently [Georgopoulos 1986, Zhang 1997, Moran 1999, Schwartz 2000, Wessberg 2000, Issacs 2000, Nicolelis 2002]. Methods that accurately and efficiently decode stimulus parameters given neural signals not only advance the state of bio-engineering research, but also shed light on how the brain encodes information [Rieke 1997].

Pattern recognition, which is synonymous to classification, is the action of predicting or classifying an unknown observation into predefined classes based on historical data. In particular, decoding of a discretely valued stimulus using spike trains has been investigated extensively in the context of pattern recognition. Researchers have applied various pattern recognition techniques to treat the decoding problem. More importantly, most of the current work uses the mean firing rate, the number of spike counts in a fixed window, as the sole *feature* for decoding [Abbott 1994, Sanger 1996, Zhang 1998, Brown 1998, Johnson 1996, Reich 2000, Johnson 2001]. Here, *feature* refers to the patterns

embedded in the spike trains (e.g., mean firing rate, change of firing rate, and precise timing of a particular spike) that are correlated to the stimulus parameter. However, decoding based on firing rate alone assumes that no additional patterns exist in the spike train, an oversimplified assumption [Steveninck 2002]. Thus, we ask whether any improvements over either accuracy or resolution may be achieved when additional features besides firing rate are included in the decoding task. The key issue thus becomes that of finding the optimal feature(s) that ensure the best decoding performance.

To address this question, this chapter presents an adaptive scheme that searches for the optimal feature(s) based on wavelet and information theory. Because different pattern recognition methods behave differently even on the same set of data, in order to ensure the comparability between the different features, we fix our classification tool to be the Bayesian classifier introduced in Section 2.4. Under this scheme, a naïve feature set is first generated using Haar wavelet packet decomposition of the spike trains. Because of the recursive construction of wavelet packets, these features form a tree structure called the wavelet packet coefficient tree. Then we suggest a tree pruning strategy that searches for the most informative feature(s) along the coefficient tree with respect to the stimulus parameters. Here, informative-ness is defined by a score function that quantifies the feature's discriminability towards the stimuli. The scored function proposed here is the mutual information between the feature v and the stimuli label X because of its statistical properties as well as its close relationship with the Bayesian classifier. The technique is applied to both surrogate data and actual spike data. Decoding performance based on the

optimal feature(s) is compared against the performance obtained using mean firing rate alone as the decoding feature.

Generally, wavelet-based analysis is more suitable when dealing with non-stationarity and specifically locally stationary processes [Mallat, 1998]. As seen in Section 2.3, the multi-resolution analysis feature of wavelets efficiently decomposes the spike trains into features at different scales through projection, thus providing versatility in handling possible patterns embedded in the spike train. Again, we use the Haar wavelet packet to decompose the spike trains. Some of the Haar wavelet packet's special properties, such as compactness and biologically relevant interpretations of the projection coefficients, make it an ideal candidate for decomposing spike trains. We note that others have explored the possibility of using wavelet packet as a mean of processing spike data in the decoding context [Kralik 2001]. But we are the first to investigate the decodability for each individual wavelet packet coefficient.

When dealing with wavelet packet projection, often times the features, i.e. the projection coefficients, are organized into a tree structure using the Pyramid Algorithm explained in Section 2.3.2. *Best Basis* is an algorithm that prunes the coefficient tree in order to search for an optimal set of bases for compression or denoising purpose [WickerHauser 1994, Mallat 1999, Percival and Walden 2001]. Saito (2002) presented a *Best Basis* algorithm that searches for the most discriminating basis among the wavelet packet tree using Kullback-Liebler distance as the discriminating measure. However, in the context of decoding, the full optimal basis is less relevant as the *curse of dimensionality* results an

exponential explosion of the training data if the full basis is used for decoding. Thus, the tree pruning method proposed in this chapter, although analogous to the *Best Basis* algorithm, searches for a few features with large decodability instead of the full optimal basis. Instead of finding the optimal sub-space upon which to project data, we are looking for an optimal subset.

In Section 2, a study of the mutual information as the decodability score function is presented. Then the wavelet packet tree based optimal feature extraction routine is introduced. In Section 3, the technique developed earlier is applied to both surrogate data and the actual spike data from PRR. This thesis assesses the performance of the proposed method against that obtained by using mean firing rate alone. In the appendix, a theoretical exposé on the finite sample effect is carried out for the two-class case in order to further justify the use of mutual information as the score function. Even though all the examples in this chapter use spike train data, the techniques proposed can be easily generalized to other types of neural signals, such as the local field potential.

4.2 Feature extraction

As reviewed in Section 2.3, the wavelet packet decomposition returns a total of $TlogT$ features given a spike train that is quantized into T sampling periods of length δT. It is however not realistic to include all the features in the decoding process because the *curse of dimensionality* [Cherkasssky 1998] prohibits such a naïve approach. Moreover, very few of these features are practically informative. Thus, we must select a few relevant

features in order to make practical decoding feasible. The selection strategy proposed here involves a score function D, which assigns a discriminability measure to each feature. Then we couple the score function with a pruning strategy that searches the Haar wavelet packet coefficient tree while eliminating the less-informative coefficients. In the following sections, we first investigate the use of mutual information as the score function. Then we introduce the tree pruning strategy that searches for the most informative features.

4.2.1 Discriminability and score functions

In order to assess the relevance of each projection coefficient, v_{jk}, it is necessary to introduce the concept of a score function D, which characterizes each feature's decodability. The score function is defined as a map from the feature's conditional probability distributions with respect to the stimulus parameter to a positive real number, i.e.

Equation 4.1 $$D : P_1 \times P_2 ... \times P_M \rightarrow R^+ ,$$

where P_1, P_2,...,P_M are short for the conditional probabilities $P(v|X_1)$, $P(v|X_2)$,…, $P(v|X_M)$, with M being the number of stimulus classes available. Intuitively, the larger the discrepancies between the P_i's, the easier it is to classify different stimulus conditions given an observation. Therefore, the score function should summarize the discrepancies amongst all the conditional distributions with respect to the different stimulus parameters X_i into a single discriminability number. For example, the Fisher linear discriminant measure and the Kullbach-Liebler divergence are both frequently used discriminability

measures [Thomas and Cover 1991, Devroye 1996, Cherkassky 1998]. However, the Fisher linear discriminant measure implicitly assumes the conditional distributions P_1, $P_2,\ldots,P_M$ are normally distributed, which constrains the statistical analysis to mean and variance only. In addition, even though the *KL* divergence is a useful binary classification measure, it lacks a multiple-class parallel. Researchers sometimes have to resort to awkward pair-wise summations of the binary *KL* divergences between all possible pairs of classes [Saito 2002]. Mutual information on the other hand does not have the above undesirable features while possessing some nice interpretation and properties. The remainder of the section introduces mutual information in the context of decoding and assesses mutual information as the decodability measure. For interested readers, an analysis of the finite sample effect and mutual information can also be found in the appendix.

4.2.1.1 Mutual information overview

One choice of the score function is the mutual information between the features and the classes, $I(X;v)$. Mutual information characterizes the knowledge that one random variable prescribes with respect to another [Thomas and Cover 1991]. To understand the role of mutual information in the decoding context, it is necessary to define some relevant information theoretical quantities.

For class variable X and feature v, define the Shannon entropy $H(X)$ and the conditional entropy $H(X|v)$, two measures of information content as

Equation 4.2
$$H(X) = \sum_{x} P(X = X_i) \log \frac{1}{P(X = X_i)},$$

Equation 4.3
$$H(X \mid v') = \sum_{i,v'} P(X = X_i, v = v') \log \frac{1}{P(X = X_i \mid v = v')},$$

where $P(X=X_i)$ is the marginal probability of X, $P(X=X_i|v=v')$ is the conditional probability of X when another random variable v takes the value v', and $P(X=X_i,v=v')$ is the joint probability between X and v [Cover and Thomas 1991]. We further notice the following relationship between $H(X)$ and $H(X|v)$

Equation 4.4
$$\begin{aligned} & I(X;v) \\ &= H(x) - H(x \mid v) \\ &= \sum_{x,v'} P(X = x, v = v') \log \frac{P(X = x, v = v')}{P(X = x) P(v = v')} \end{aligned},$$

where $I(x,v)$ is the mutual information between the stimulus class X and the feature v.

Mutual information is also closely related to the Bayesian classifier as it can be directly derived from the Bayes' formula. Recall Equation 2.16 states that

$$P(X \mid v) = \frac{P(v \mid X) P(X)}{P(v)}.$$

Manipulating this equation yields the following expression

$$P(X \mid v) = \frac{P(v \mid X) P(X)}{P(v) P(X)} P(X).$$

Taking the *log* of the above probability and the expected value over X and v on the above equation yields the following,

Equation 4.5
$$\sum_{X,v} P(X,v) \log P(X \mid v) = \sum_{X,v} P(X,v) \log \frac{P(v,X)}{P(v) P(X)} + \sum_{X,v} P(X,v) \log P(X).$$

By the definition in Equation 4.2 and Equation 4.3, the above relationship is equivalent to

$$-H(x \mid v) = I(X;v) - H(X),$$

the same relationship as Equation 4.4 again. Furthermore, recall from Equation 2.17, the Bayesian classifier attempts to maximizes *P(X|v)* for every *v*. Thus, when taken over the negative log expected value, it also minimizes the conditional entropy *H(X|v)*, which in turn maximizes the mutual information between *X* and *v*. Thus, we see Bayesian classifier itself manifests an important information theoretical dogma: *conditioning reduces entropy*.

The above analysis suggests that mutual information is an ideal candidate for the score function *D* when the decoding tool is chosen to be the Bayesian classifier. In addition, mutual information is closely related to the Bayesian classifier error E^*, defined in Equation 2.18. Assume there is no prior knowledge on the classes, i.e. the prior probabilities on the classes are equal, then the mutual information between the classes and features are bounded by the following relationship [Devroye 1998],

$$1 + \log(1 - E^*) \geq I(v;X) \geq 1 - [E^* \log \frac{1}{E^*} + (1 - E^*) \log \frac{1}{1 - E^*}],$$

where the right-hand side inequality is the Fano inequality and the left-hand side inequality can be defined from Jensen's inequality [Devroye 1998]. Evidently, large mutual information corresponds to a smaller classification error. An in-depth investigation on the classification error and the mutual information presented in the Appendix further justifies the use of mutual information as the discriminability measure. Mutual information also carries some additional useful statistical properties.

P1 *Mutual information* $I(X;v_1,v_2,...,v_d)$ *is invariant under an orthonormal transformation,* T*, on the feature set* $V=\{v_1,v_2,...,v_d\}$.

This can be easily verified as [Sirzaker 1994],

$$P(T\,V) = P(V)\cdot|T|,$$

where $V=(v_1,v_2,...,v_d)$ and $|T|$ is the determinant of the T, which equals 1 when T is an orthonormal matrix [Ross 2000]. Therefore, the value of the mutual information is invariant under the transformation.

P2 *Mutual information is additive, i.e.*

$$I(X;v_1,v_2,...,v_d) = \sum_{i=1}^{d} I(X;v_i)$$

if the features $v_1, v_2,...v_d$ *are conditionally independent (independent conditioned on the stimulus parameter X) and unconditionally independent simultaneously (independent without conditioning). We denote the conditionally and unconditionally independence as CU-independence.*

Finally, the definition of mutual information naturally accommodates multiple-class classification problems without resorting to the awkward pair-wise sum often found in other distance measures like KL-divergence or Hellinger distance [Saito 2002]. The *conditioning reduces entropy* interpretation remains intact for multiple class applications.

4.2.1.2 Mutual information and optimal features

The above review on the mutual information *I(X;v)* not only justifies its use as a score function for measuring discriminability, but also hints at the possibility of devising a feature selection strategy. We notice that without any prior knowledge, the entropy associated with the stimulus parameters $X_1, X_2, \ldots, X_M$ is

$$H(X) = \log(M),$$

a fixed number independent of the features. Under this assumption, reducing the conditional entropy *H(X|v)* is equivalent to increasing the mutual information *I(X;v)*. As *H(X|v)* approaches 0, *X* becomes almost deterministic given *v*. Therefore, the most informative feature for the Bayesian classifier is the one that maximizes the mutual information *I(X;v)*. This important observation will be expanded and formalized in the remainder of the section.

First we revisit the neural decoding problem. The task of decoding is to infer some discrete behavior parameter *X* from an observed spike train $\boldsymbol{s}=\{s_0,\ldots s_{T-1}\}$, given historically collected spike train data under behavior states, $X_1,\ldots,X_M$. The best possible decoding strategy is to plug the whole observed spike train ***s*** into the Bayesian classifier such that Equation 2.16 becomes

$$\tilde{X} = \arg\max_{X}\{P(X \mid \boldsymbol{s})\}.$$

Here *P(X|**s**)* is the posterior probability which is proportional to the likelihood *P(**s**|X)*. In this case, no information is lost as the mutual information *I(X;**s**)* contains the full knowledge that the spike train holds about the stimulus *X*. This is a version of the *Data*

Processing Inequality outlined in Thomas and Cover [1991]. However, in practice this approach is not feasible because one needs to estimate the conditional probability $P(\mathbf{s}|X)$, i.e. $P(s_0,...,s_{T-1}|X)$. As T grows, the *curse of dimensionality* [Cherkassky 1998] demands an exponential explosion of the training data in order to construct the joint distribution $P(s_0,...,s_{T-1}|X)$. Thus, it is not practically possible to use the full spike train $\mathbf{s}$ in the Bayesian classifier.

An alternative alternative approach is to project the spike train onto some basis or feature vectors such that the projection coefficients display large decodability. Then, instead of the full spike train $\mathbf{s}$, we include those selected features into the Bayesian classifier. Formally, we denote an orthonormal transformation as $\mathtt{T}$ such that

Equation 4.6 $$\mathbf{v} = \mathtt{T} \cdot \mathbf{s},$$

where $\mathbf{v}=\{v_0,...,v_{T-1}\}$ is the projection coefficients of $\mathbf{s}$ onto the basis vectors of $\mathtt{T}$. By property P1, mutual information is invariant under this transformation,

Equation 4.7 $$I(X;\mathbf{s}) = I(X,\mathbf{v}).$$

In addition, if the components of $\mathbf{v}$, $v_0,...,v_{T-1}$ are *CU* independent, then by property P2,

Equation 4.8 $$I(X;v_o,v_1,...,v_{T-1}) = \sum_{i=0}^{T-1} I(X;v_i).$$

Thus, ideally, the suggested feature extraction method will focus on finding a transformation, $\mathtt{T}^*$, such that the following criterion is satisfied: the d *CU* independent projection coefficients $v_0^*,...,v_{d-1}^*$ preserve most of the mutual information, namely

$$\sum_{i=0}^{d-1} I(X;v_i^*) \approx I(X;\mathbf{s}).$$

Because of the independence as well as the reduction of dimensionality, estimating the corresponding conditional probabilities $P(v_i^* \mid X)$ will not result in the explosion of the number of training samples required as seen in the *curse of dimensionality*. In Section 4.2.2, we explore some techniques that extract the features $v_0,\ldots,v_{d-1}$ under the Haar wavelet packet transformation framework.

4.2.1.3 Estimating the mutual information

To compute mutual information, the conditional probability $p(v|X)$ must be estimated. As shown in Section 2.4, Parzen window method is used [Parzen 1965]. The Parzen window approach applies Gaussian kernels to the observed data and returns density estimation in the form of the normalized sum of Gaussians centered at each data point. One can write the density function estimated by his approach as

$$p(v \mid X = c) = \frac{1}{N_c} \sum_{i=1}^{N_c} G(v - v_i, \sigma)$$

where $G(v, \sigma)$ is a Gaussian kernel with mean v_i (the observed data in class $X=c$) and standard deviation σ, and N_c is the total number of trials in class X_c. Clearly $p(v|X=c)$ is a density function because it integrates to 1 over all values of v. Therefore, we can use the Parzen window approximation in place of the true conditional density functions (which is unavailable) to estimate the mutual information. The choice of σ controls the smoothness of the probability density. We observe that when σ is sufficiently small, the mutual information is equivalent to the one computed using the histogram rule, namely,

$$P(v = v_i \mid X = c) = \frac{1}{N_c} \sum_{i=1}^{N_c} In(v_i),$$

where $In(v_i)$ is the indicator function,

$$In(v_i) = \begin{cases} 1 & if \quad v = v_i \\ 0 & otherwise \end{cases}.$$

Generally, we keep the value of σ small when the scales of the wavelet coefficients are small and vice versa.

4.2.2 Wavelet packet tree pruning

The previous section defined mutual information as the score function, D, that assesses the discriminability of features, v, with respect to the stimulus parameter X. Moreover, the theoretical analysis of the mutual information $I(X;v)$ suggests a feature extraction approach that searches for an orthonormal transformation T on the spike train $\boldsymbol{s}$ such that a few independent transformed features $v_0^*,...,v_{d-1}^*$ preserve most of the mutual information $I(X;\boldsymbol{s})$. This section realizes this proposition by introducing a feature selection strategy that integrates mutual information with the Haar wavelet packet. The selection strategy adopted here is analogous to the *Best Basis* algorithm used in the signal processing and data compression community [Wickerhauser 1994, Mallat 1999, Percival and Walden 2001]. Moreover, Saito and Coifman suggested a most discriminating *Best Basis* method in a different context [Saito 2002]. However, unlike the *Best Basis* algorithm, our approach searches for the d most discriminating features instead of a full basis.

As seen in Section 2.3.3, the cardinality of the Haar wavelet packet coefficients given a spike train of length T is $TlogT$. In addition, the construction of the Haar wavelet packet

ensures that the member functions within a node and between different nodes are orthogonal (Proposition 2.1). This poses a challenge when the optimal basis for some signal processing criterion (de-noising, compression, etc.) is required because searching through all the possible collections of orthonormal functions causes a combinatorial explosion. The *Best Basis* algorithm is an efficient technique that prunes the wavelet packet tree and evaluates the applicability of each node in the tree by comparing it with its parent node, using an additive score function [Wickhauser 1994]. In the case of the most discriminating *Best Basis* algorithm [Saito 2002], the score function is chosen as the pair-wise summation of Kullbach-Liebler divergences between all the conditional probabilities $P(v|X_i)$ and $P(v|X_j)$.

Our approach on the other hand looks for the d most discriminating features instead of the full basis. Recall from Section 4.2.1.2 that we ideally seek a transformation $\mathbf{T}^*$ such that the d largest *CU*-independent projection coefficients $v_0^*,...,v_{d-1}^*$ preserve most of the mutual information, namely,

$$\sum_{i=0}^{d-1} I(X;v_i^*) \approx I(X;\mathbf{s}).$$

However, because $I(X;s)$ is difficult to compute in practice and *CU* independence is a stringent requirement, it is necessary to either use the sufficient condition for the constraints or modestly relax the above constraints for practical implementation. First, note that orthogonality is a necessary condition for the independence between the features. To see this, define two non-orthogonal random variables v_1 and v_2. Because they are not orthogonal, v_1 can be expressed as the weighted sum of v_2 and a residual term v_{res}, i.e.

$$v_1 = av_2 + bv_{res}.$$

Obviously, v_1 and v_2 are dependent and the level of dependence is determined by the weight a. Thus non-orthogonality implies non-independence, and the first modification of the constraint is that the wavelet packet functions associated with the selected features have to be mutually orthogonal. Another observation is that the mutual information of the member coefficients of the parent node N_{jl} equal that of the two children nodes $N_{(j+1)2l}$ and $N_{(j+1)(2l+1)}$,

$$I(X;[\{v_{jk} \mid v_{jk} \in N_{jl}\}]) = I(X;[\{v_{j+1k} \mid v_{j+1k} \in N_{(j+1)2l}\}, \{v_{jk} \mid v_{jk} \in N_{(j+1)(2l+1)}\}]).$$

The validity of this equation relies on the fact that the coefficients $[\{v_{j+1k} \mid v_{j+1k} \in N_{(j+1)2l}\}, \{v_{j+1k} \mid v_{j+1k} \in N_{(j+1)(2l+1)}\}]$ can be obtained via an orthogonal transformation on the coefficients $[\{v_{jk} \mid v_{jk} \in N_{jl}\}]$ as seen in the nature of the *Pyramid Algorithm* (Section 2.3) and property P1. In another words, the coefficients in the two children nodes are orthonormal transformations of the ones in the parent node; thus the associated mutual information*s* are invariant. Ideally, we would like to find a few features from either the parent node N_{jl} or the two children nodes $N_{(j+1)2l}$ and $N_{(j+1)(2l+1)}$ so that the sum of their mutual information is close to the overall mutual information, $I(X;[\{v_{jk} \mid v_{jk} \in N_{jl}\}])$. However, the node mutual information $I(X;[\{v_{jk} \mid v_{jk} \in N_{jl}\}])$ is difficult to calculate and the *CU*-independence is hard to satisfy in general. Thus our second relaxed constraint is that instead of keeping a few *CU*-independent features, $v_0^*,...,v_{m-1}^*$ i.e.

$$\sum_{i=0}^{m-1} I(X; v_i^*) \approx I(X; \{v_{jk} \mid v_{jk} \in N_{jl}\})$$

where

$$v_0^*, \ldots, v_{d-1}^* \in N_{jl} \quad or \quad \{N_{(j+1)2l,} N_{(j+1)(2l+1)}\},$$

only the one with the largest discriminability score among the parent and children nodes should be retained, namely

$$v^* = \max(v_{jk} \mid v_{jk} \in \{N_{jl}, N_{(j+1)2l,} N_{(j+1)(2l+1)}\}).$$

In summary, the two relaxed constraints are

Constraint 1: *The wavelet packet functions that correspond to the optimal features have to be orthogonal to each other.*

Constraint 2: *The single most informative feature in any pairs of parent-children nodes must be included.*

Now we are ready to describe out recursive wavelet packet pruning technique. Let the training spike train ensembles be denoted by $\{S_1^i\}, \{S_2^i\}, \ldots, \{S_M^i\}$, where the subscript corresponds to the stimulus parameters $X_1, \ldots, X_M$. Furthermore, assume the spike trains in the ensembles are of length T, where T is a power of 2. Using the *Pyramid Algorithm*, the Haar wavelet packet projection coefficients at any scale j and location k can be computed. These coefficients are called the *naïve feature set*, and they are naturally organized in the tree structure seen in Section 2.3.2. Denote the tree associated with the decomposition as the *feature tree,* `F`. Now starting from the coarsest scale, i.e.

$j = \log_2 T$, first compute the score function D for the feature set $\{v_{jk}\}$ with $j=log_2T$ whose score function for $\{v_{jk}\}$ is defined as

Equation 4.9
$$D_{jk} = \sum_{v}\sum_{X} p(v_{jk} \mid X)\, p(X) \log \frac{p(v_{jk} \mid X)}{\sum_{X} p(v_{jk} \mid X)\, p(X)}$$

and form a discriminability set $\{D_{jk}\}$ for each k. The conditional probability $p(v_{jk}|X)$ is estimated using the Parzen window method shown in Section 4.2.1.3. Also we seed the optimal feature set as

Equation 4.10
$$\{v_k^{opt}\} = \{v_{jk}\},$$

i.e. to start, the optimal feature set is initialized to be the j^{th} scale projection coefficients because they are the descendants of the rest of the coefficients. Next we proceed to the j-1^{th} scale, where we again compute the score functions D for each feature $v_{j-1,k}$ and form the discriminability set $\{D_{j-1,k}\}$. For each triplet of parent-children nodes $\{N_{(j-1),l}, N_{j,2l,} N_{j,(2l+1)}\}$, $l=0,..T/2-1$, we can find the feature v^* with the largest discriminating measure,

$$v^* = \max(v_{jk} \mid v_{jk} \in \{N_{j,l}, N_{(j+1),2l,} N_{(j+1),(2l+1)}\}).$$

Once it is located, the node that contains v^* is labeled N^* and we can replace the corresponding features in the set $\{v_k^{opt}\}$ by the ones in N^*. For example, if $N^* = N_{(j-1),l}$, then

$$\{v_k^{opt} \mid v_k^{opt} \in \{N_{j,2l}, N_{j,(2l+1)}\}\} = \{v_{(j-1),k} \mid v_{(j-1),k} \in N^*\},$$

effectively the optimal feature set $\{v_k^{opt}\}$ is updated to include all the features in N^* along with v^*. As a result, we remove the node $N_{j,2l}$ and $N_{j,(2l+1)}$ from the original feature tree,

F. On the other hand, if $N^* = N_{j,2l}$ *or* $N_{j,(2l+1)}$, then no update of $\{v_k^{opt}\}$ occurs and both $N_{j,2l}$ and $N_{j,(2l+1)}$ remains on the feature tree, F. Once the update is completed at scale *j-1*, we move up to scale *j-2* and repeat the above process by comparing the parent node $N_{j-2,l}$ with its remaining descendents. Again, the optimal feature set $\{v_k^{opt}\}$ as well the tree F is updated. This procedure terminates when the updates on $\{v_k^{opt}\}$ terminates and F is no longer modified. Also the Haar wavelet packet functions associated with the features $\{v_k^{opt}\}$ are orthogonal to each other because of Proposition 2.1. Graphically, we may express the pruning procedure in Figure 4.1:

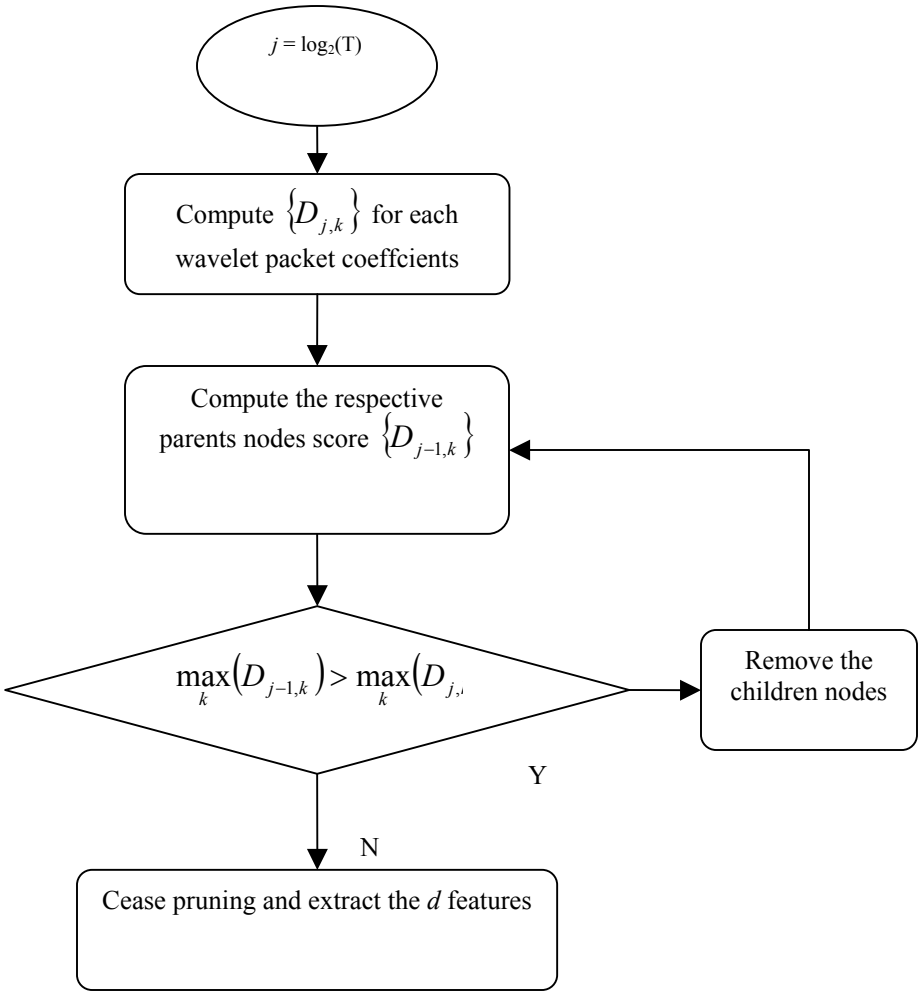

Figure 4-1 Prune the wavelet packet tree using score function D

The optimal set of features $\{v_k^{opt}\}$ comprises the wavelet packet projection coefficients from different scales and locations, and they include all the locally most discriminating features v^* as shown by the above algorithm. Finally from $\{v_k^{opt}\}$, we can select d features $v_0^{opt},...,v_{d-1}^{opt}$ to be used in the decoding of the stimulus parameter X.

In practice, the *d* features not only need to carry large discriminating scores, but also should be evaluated for conditional independence because as we pointed out earlier, orthogonality is only a necessary condition for independence. We can use hypothesis test methods (e.g., *cross-tabulation* by Mathworks) to help understand the dependence between features so that a minimal amount of redundant information is included in the decoding process. At the current stage, properties of $v_0^{opt},...,v_{d-1}^{opt}$ will be assessed on an individual basis for each application. In addition, a good way of picking the number *d* is currently lacking. Rather, it varies depending on the actual application. However, as we will see in the results section, even by letting *d=1*, the single most informative feature often outperforms the mean firing rate.

4.3 Results

This section applies the above ideas and algorithms to both surrogate data sets and actual behavior conditioned spike trains in order to illustrate the utility of the method. First examine the application of the algorithm to artificial data with different discriminating features. These simulations confirm the basic operation of the approach. Next apply the method to actual neural data recorded in PRR. In both cases, we compare the decoding performance of our method against the performance obtained using mean firing rate as the only feature.

Inhomogeneous Poisson Processes I

We first investigate the performance of the proposed decoding method on surrogate data generated from known inhomogeneous Poisson processes. The surrogate data are

generated using the technique outlined in Section 3.4. Recall that for each *1* ms window, the probability of not observing a spike is specified as

$$P(s_k = 0) = e^{-\lambda_k 0.001},$$

while the probability of observing a spike is

$$P(s_k = 1) \approx 1 - e^{-\lambda_k 0.001}.$$

Now we generate a uniform random number *r* using a generic random number generator. If $r>P(s_k=0)$, we register a *1* at time k in the artificial spike train; otherwise, we register a *0*.

The first example presents inhomogeneous Poisson processes with undistinguishable mean firing rates; however, patterns besides mean firing rate are embedded in these processes. Assume there are 4 classes, X_1, X_2, X_3 and X_4 whose firing rate function $\lambda(t)$ are the following

$$\begin{aligned}
\lambda_1(t) &= 15\mathbf{1}([1 \;\; 512]) + 4\mathbf{1}([65 \;\; 96]) - 4\mathbf{1}([97 \;\; 128]) \\
\lambda_2(t) &= 15\mathbf{1}([1 \;\; 512]) + 8\mathbf{1}([65 \;\; 96]) - 8\mathbf{1}([97 \;\; 128]) \\
\lambda_3(t) &= 15\mathbf{1}([1 \;\; 512]) - 4\mathbf{1}([65 \;\; 96]) + 4\mathbf{1}([97 \;\; 128]) \\
\lambda_4(t) &= 15\mathbf{1}([1 \;\; 512]) - 8\mathbf{1}([65 \;\; 96]) + 8\mathbf{1}([97 \;\; 128])
\end{aligned},$$

where $1([t_1 \; t_2])$ defines a constant function over the range $[t_1 \; t_2]$ and the units are in Hz. Note the value of the mean firing rate over the range *[1 512]*, namely,

$$\overline{\lambda} = \frac{\sum_t \lambda(t)}{512}$$

is 15 Hz, identical for all classes. Therefore, we expect that using the mean firing rate as the feature yields decoding performance no better than chance, which is *25%* correct. On the other hand, the difference of the firing rate over the range *[65 96]* and *[97 128]*, i.e.

$$f = \frac{\sum_{t=65}^{96} \lambda(t) - \sum_{t=97}^{128} \lambda(t)}{32},$$

yields the most discriminating feature because the firing rate at each time step is the only modulated parameter for an inhomogeneous Poisson process [Ross 1994]. The sum of the difference of the firing rates thus becomes the best discriminating feature.

The wavelet packet decoding method is applied to spike trains generated according to the above firing rate functions. For each class, the aforementioned simulation algorithm produces 500 training samples and 500 testing samples. The following test and analysis is done on the 500 testing samples and the average performance is reported. The optimal selection strategy outlined in Section 4.2.2 returns 512 features that are the projections of the spike trains onto the selected orthonormal Haar wavelet packet basis functions. The values of the mutual information associated with these features are plotted in Figure 4-2A. The wavelet packet function corresponds to the largest mutual information (red circle in Figure 4-2A) is plotted in Figure 4-2B. It indeed agrees with the aforementioned feature *f*. In addition, the distribution of mean firing rate and the optimal feature are shown in Figure 4-2C.

A

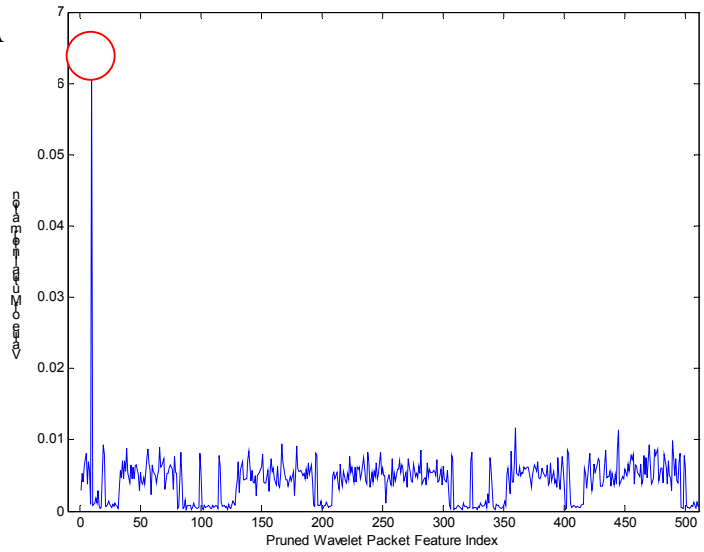
Pruned Wavelet Packet Feature Index

B

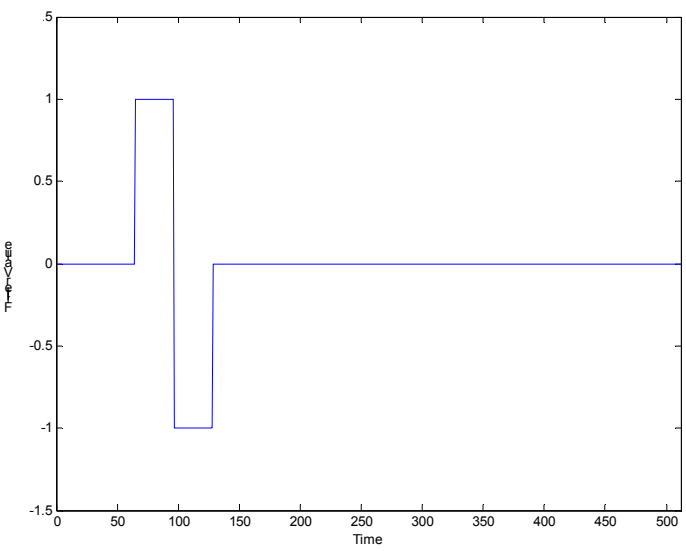
Time

C

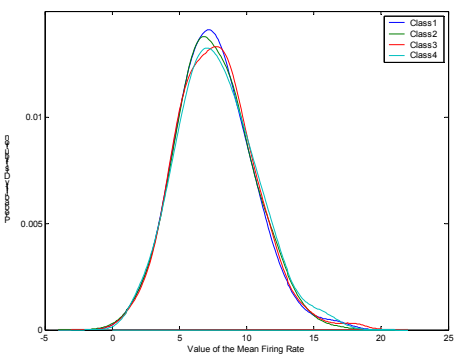
Class1
Class2
Class3
Class4
Value of the Mean Firing Rate

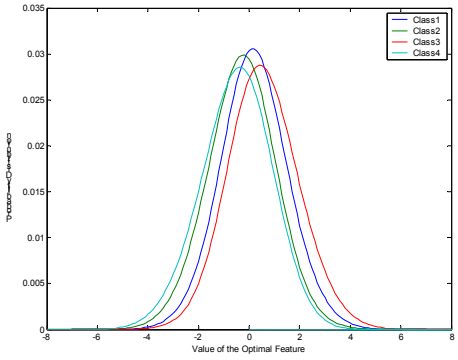
Class1
Class2
Class3
Class4
Value of the Optimal Feature

Figure 4-2 Application of the optimal wavelet packet to the surrogate data

A) The value of mutual information of the pruned wavelet packet features. The x-axis indexes the 512 wavelet packet functions, while the Y-axis indicates the value of the corresponding mutual information. B) The wavelet packet function with the largest mutual information. X-axis is time, and Y-axis is its value. C) The distribution of the mean firing rate and the optimal wavelet packet feature. The panel on the left displays the mean firing rate distribution of the training data; the panel on the right shows the optimal feature. In both figures, the x-axis is the value of the coefficients and the y-axis is its distribution. Color codes the 4 classes.

To validate the optimal feature, we apply the Bayesian classifier to the training data using both the optimal feature v_{opt} as well as the mean firing rate $\overline{\lambda}$. Not surprisingly, the one using mean firing rate returns an average correct classification of 25%, exactly on par with chance. On the hand, the optimal feature on average returns correct classification of 33%. While this result may not seem impressive, it should be recognized that these classes are extremely similar, and therefore difficult to discriminate.

Inhomogeneous Poisson Processes II

We can also augment the above firing rate function to include a discriminating feature that describes precise timing in a spike train. For each previously generated surrogate spike train, we embed a single spike at a specific location in a background of spikes generated from a Poisson process. We use the following equations to illustrate this important addition to our surrogate data,

$$s(t) \sim \lambda(t), \quad and \quad s(\tau) = 1,$$

where $s(t)$ is the spike train generated from the firing rate function $\lambda(t)$, and τ marks the location of the single precise spike. We continue the previous example and let the τ's be $\tau_1=1$, $\tau_2=5$, $\tau_3=9$, and $\tau_4=13$, the subscripts index the four classes. Once again, the surrogate data contain 500 training and testing spike trains for each reach direction. We apply the method illustrated in Section 4.2.2 to the surrogated data and obtain the optimal

feature set $\{v_k^{opt}\}, k = 1,...,512$. The values of the mutual information of the pruned wavelet packet features are plotted in Figure 4-3A. In addition to the optimal feature that appeared in the original example (red circle), several new features exhibit large values. However, a closer look at these new features using a cross-tabulation method [Matlab] reveals that the ones spaced with a period of 128 are highly statistical dependent, i.e. they carry the same information. For visualization purpose, we mark the dependent ones with the same marker. Therefore, we only need to show the wavelet packet functions associated with the independent features. In Figure 4-3B and Figure 4-3C, we sketch the wavelet packet functions that produce pair-wise independent features and the distribution of the corresponding coefficients, v_{33}^{opt} and v_{65}^{opt}.

A

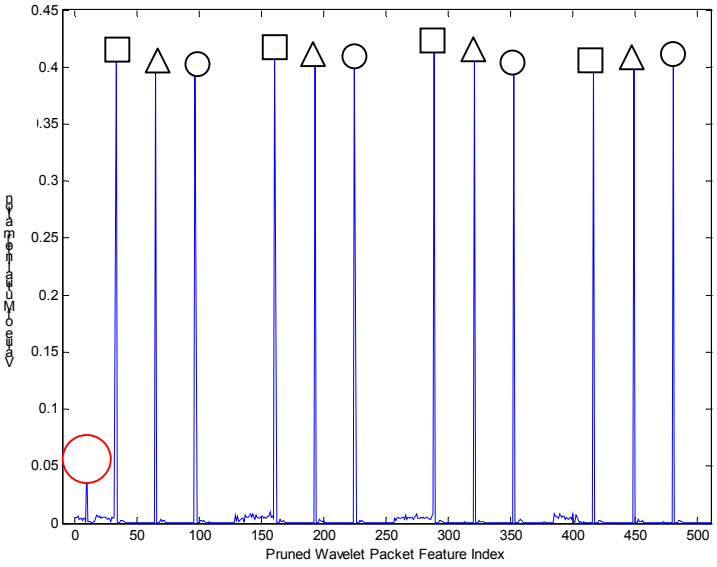

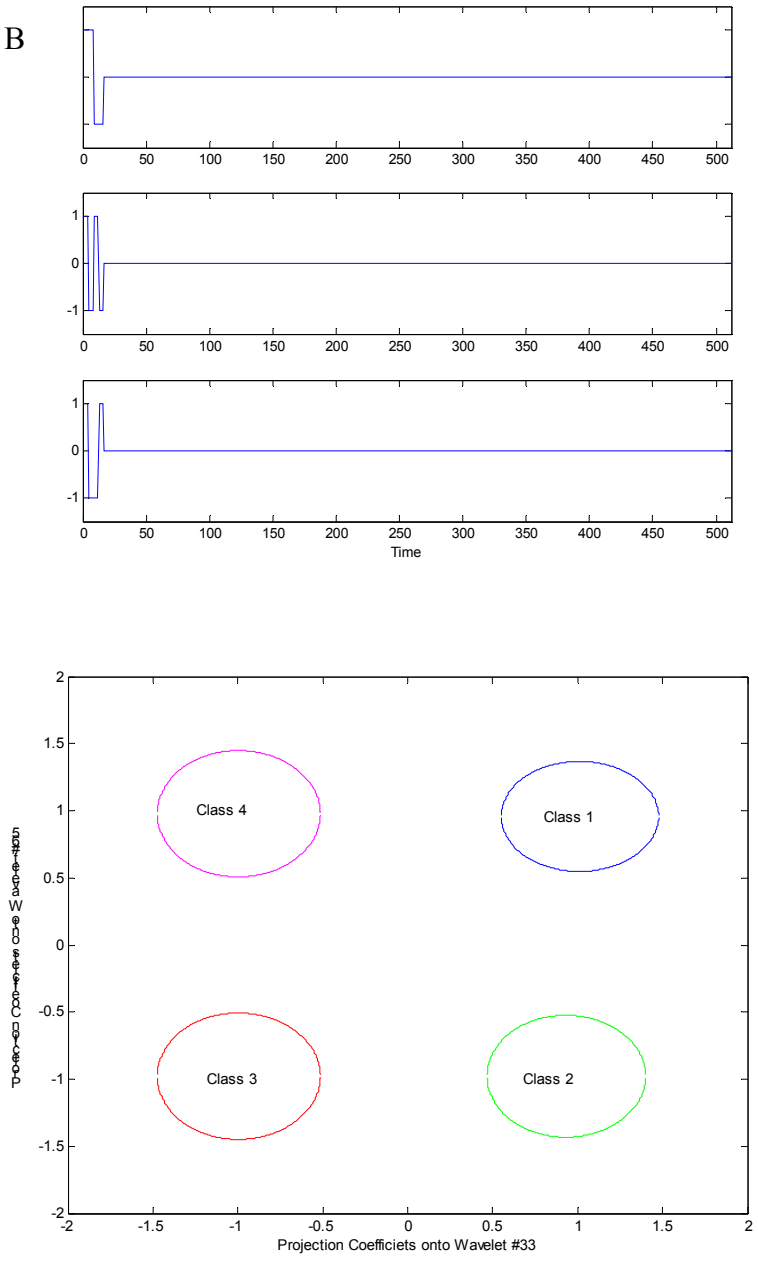

Figure 4-3 Application of the optimal selection strategy to the 2nd set of surrogate data

A) Values of the mutual information of the indexed pruned wavelet packet features. Red circle marks the feature appeared in the first example. □, Δ, and ○ each marks the features that are highly dependent. B) Waveform of the 33rd, the 65th, and the 97th wavelet packet functions. C) The distribution of the projection coefficients onto the 33rd and the 65th wavelet packet function. Different color represents different classes: blue-X_1, green-X_2, purple-X_3, and red-X_4. The ellipsoids are centered at the means of the projection coefficients, and the minor and major axis are the corresponding standard deviations.

Note that the wavelet packet functions not only cover the region of interest *[1,16]*, but also separate the 4 different classes. Observe that the separation of the classes on the two dimensional probability plane shown in Figure 4-3C allows for good classification outcome. On the contrary, using mean firing rate over the whole 512ms window in this example completely ignores the information coded in the precise spike location. Thus, just as the previous example, the decoding performance using the mean firing rate fares no better than chance while the feature extraction method displays better decoding performance. In this example, the decoding performance rises from chance (25%) to 91%, as exemplified by the separation of features among the 4 classes in Figure 4.3C.

PRR Spike Trains during Reach Task I

Next the method is applied to decode actual spike signals recorded from PRR during reach tasks. The experimental paradigm is described in Section 2.1. Here we focus on a particular 512ms window which is 300ms after the cue onset. The data is sampled at a sampling interval of 1ms. The biological importance for this particular time window is that reach intention is formed during that period [Batista 1999, Shenoy 2003]. There are a total of 15 neurons, each with 2 reach conditions, X_1 and X_2. The number of samples ranges from 25 to 115. Because of the limited samples, the classification of the reach condition given an unknown spike train uses the leave-one-out cross-validation method [Cherkassky 1998]. It singles out one sample as the test sample and use the remaining ones as the training sample to classify the test sample.

And example of the spike trains from one neuron along with the most informative wavelet packet feature is shown in Figure 4.4A.

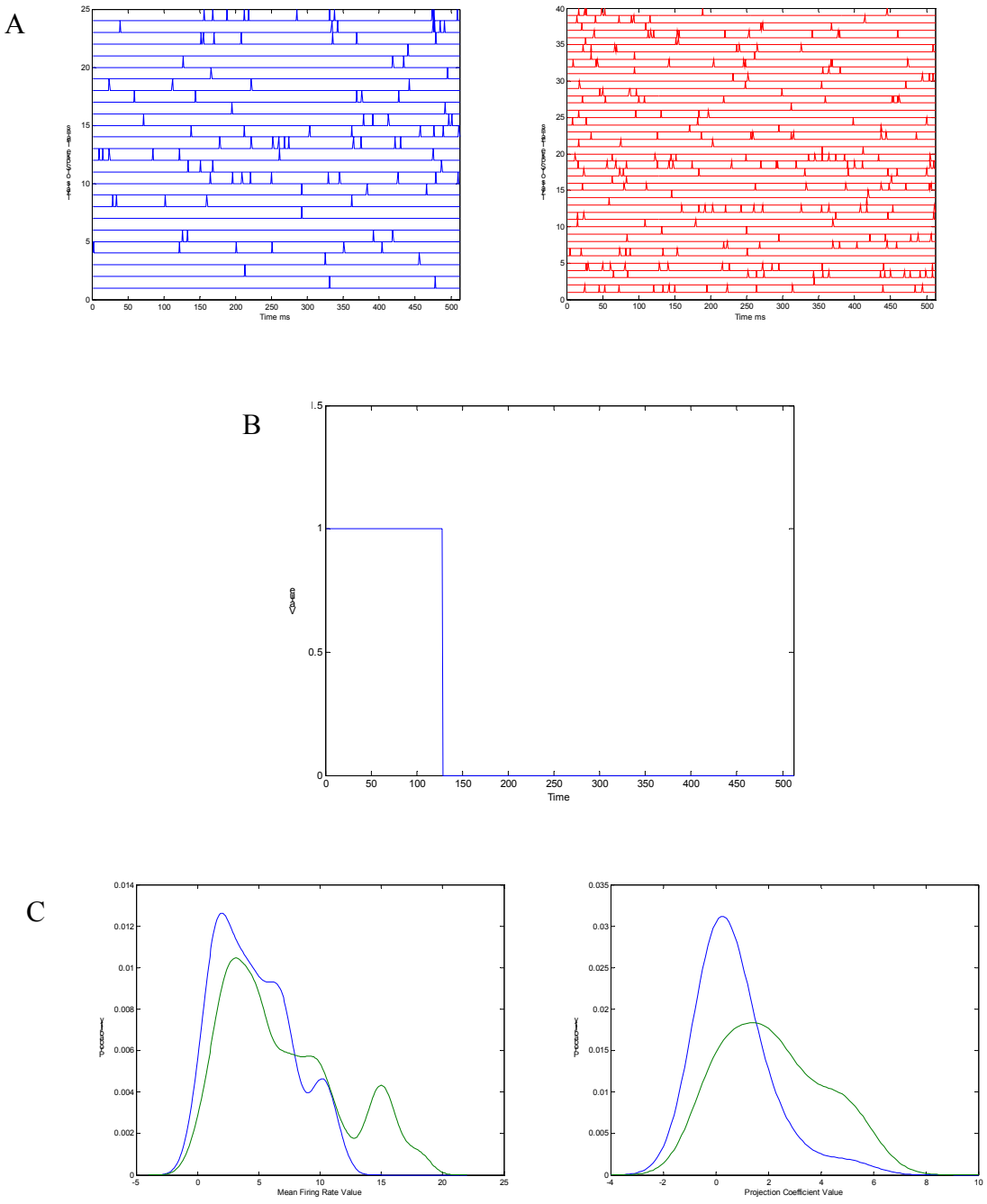

Figure 4-4 Comparison of mean firing rate and optimal wavelet packet feature for a neuron in binary reach task

A) The two panels showcase the neuron's spike trains in two different reach conditions. The x-axis marks the time in millisecond and the y-axis indexes the trial number. B) The optimal wavelet

packet function with a support of 128ms, (*j = 7, k=1*). The x-axis marks the time in milliseconds, and the y-axis is the value of the function. C) The left panel shows the distribution of the mean firing rate given the two different reach directions. Each color represents a reach direction. X-axis is the value of the coefficients and y-axis marks the probabilities. The right panel displays the optimal feature distribution for the same two reach directions.

In the above example, we can visually identify from Figure 4-4A that the neurons fire more frequently in the first 100ms in one direction than the other one. The optimal wavelet packet feature selected in this case is a window function corresponding to the first 128ms. Evidently, the discriminability of the optimal feature surpasses the ones of the mean firing rate because the two conditional distribution functions are further apart, as demonstrated in Figure 4-4C. Fittingly the correct classification rate using the mean firing rate is 36.7%, while the optimal feature approach realizes a 72% correct rate. Note the reason for the sub-50% decoding performance of the mean firing rate case can be contributed to the cross-validation technique. For each cross-validation, the training distribution is rebuilt by taking out the test sample from the whole ensemble. For sparse data sets, this results a large reduction of the prior probability $P(v|X)$; thus numerically, it is possible to achieve sub-50% performance.

Within the wavelet packet feature selection framework, we can also assess the effect of mutual information by replacing the score function with the Fisher linear discriminant measure [Fisher 1936], D_{Fisher}, which is defined as

$$D_{Fisher} = \frac{(m_1 - m_2)^2}{\sigma_1^2 + \sigma_2^2},$$

where m_1 and m_2 are the means of the data points belonging to class 1 and class2; σ_1 and σ_2 are the respective standard deviations. Obviously D_{Fisher} is large when the two clusters

are far apart, meaning the between-cluster distance is significantly larger than the within-cluster distance. We further note that the Fisher linear discriminant measure D_{Fisher} implicitly assumes that the clusters are Gaussianly distributed, in which case the discriminability can be sufficiently described by the mean and standard deviation.

Now we compute the classification performance for each neuron using mean firing rate, the optimal Fisher score feature, and the optimal mutual information feature for the 15 neurons whose number of samples ranges from 25 to 115. The average performance for each neuron is summarized in Figure 4-5.

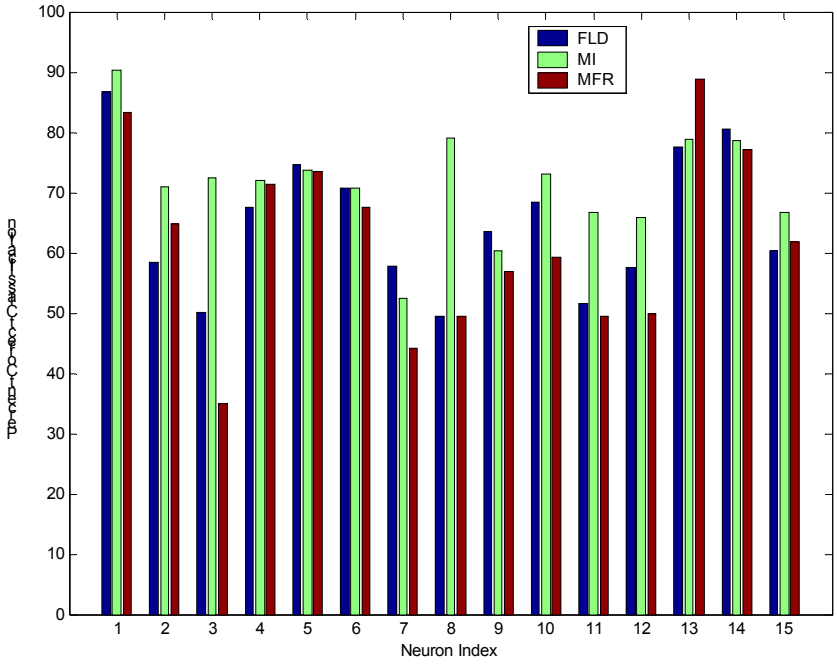

Figure 4-5 Binary single neuron reach direction classification performance

The x-axis indexes the neurons, and the y-axis marks the correct classification in percentage. The blue bar indicates the performance achieved using D_{Fisher}. The green bar indicates the performance achieved using I_Q^{Mod}. And the red bar indicates the performance achieved using the mean firing rate.

Notice the D_{Fisher} based classification returns an average decoding performance of 65.0% for all the neurons while the I_Q^{Mod} based classification returns an average decoding performance of 71.5%. On the other hand, the mean firing rate based classification returns an average decoding performance of 62.2%, the lowest amongst all three. We see that combining mutual information with the wavelet packet selection scheme returns the best decoding performance in this case. This improvement of the decoding performance can be attributed to the assumption-free nature of mutual information against the Gaussianity assumption used in the Fisher linear discriminant score. This improvement of performance also suggests that over-fitting is negligible in this example because otherwise the decoding performance can not rise [Vapnik 1995].

PRR Spike Trains during Reach Task II

Finally we apply the proposed method to spike trains in an 8 directions reach task. Again, we record from PRR with the same experimental paradigm. Instead of only two reach directions, this time the animal is required to reach to 8 different targets. Spike data from 44 neurons are collected in this experiment. For each neuron, the 8 reach locations are labeled as classes $X_1,\ldots,X_8$. First the optimal feature selection technique descried in section 4.1 is applied to each neuron. Note that for the majority of the neurons (40 out of 44), the mean firing rate over the whole 512ms window *is* the most discriminating feature. This result is not surprising because during the experiment, all the neurons are isolated based on their mean firing rate's responsiveness towards the stimulus, i.e. the reach directions. Therefore, we expect most of them display a strong correlation between the mean firing rate and the stimulus.

We thus focus on the ones with the most discriminating feature not being the mean firing rate. In Figure 4-6, we plot the most discriminating Haar wavelet packet function of an *un-tuned* neuron, i.e. the one modulated by the mean firing rate. Also, the distributions of the optimal projection coefficients as well as the mean firing rate are shown.

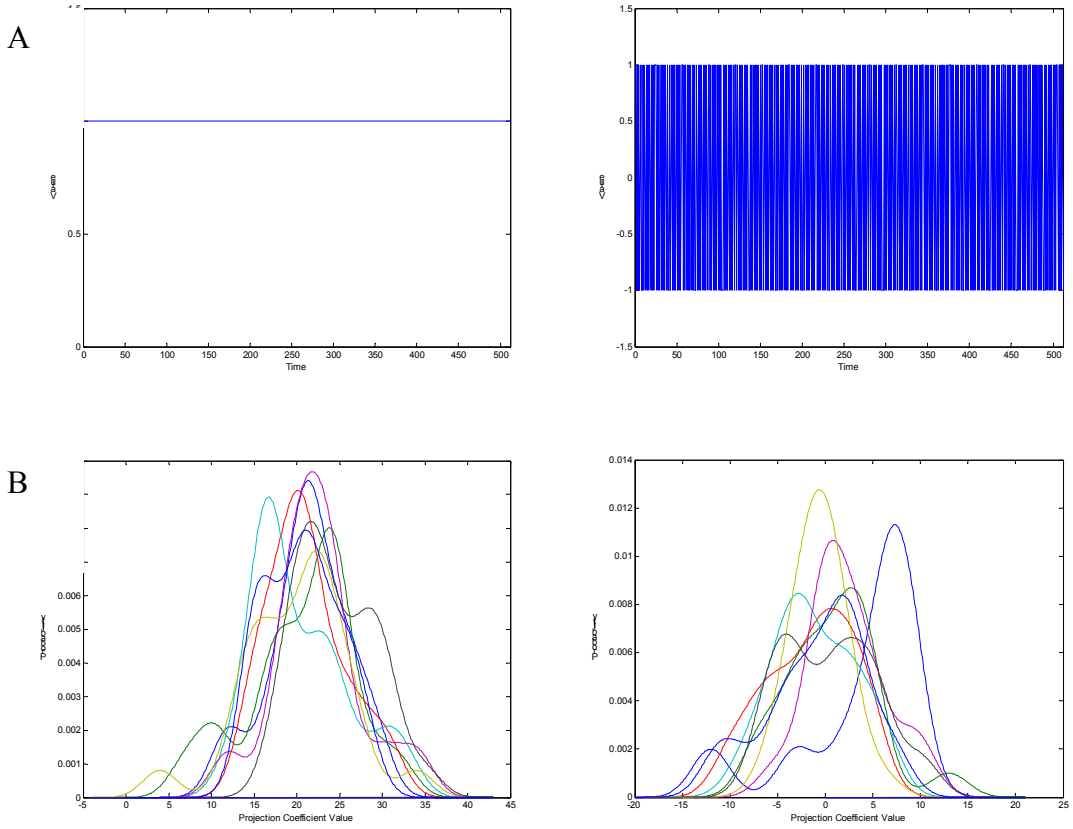

Figure 4-6 Comparison of mean firing rate and optimal wavelet packet feature for a neuron in 8 direction reach task

A) The left panel shows the constant window function over a 512ms window sampled at 1 kHz. The right panel displays the optimal wavelet packet function (*j=1,k=305*) over the same window. B) The left panel shows the distribution of the mean firing rate given 8 different directions. Each color represents a reach direction. X-axis is the value of the mean firing rate and y-axis marks the probabilities. The right panel displays the optimal feature distribution for the same 8 reach directions.

Note in Figure 4-6B that the conditional distributions of the optimal coefficients are more spread out than their mean firing rate counterpart. This validates the argument in Section 4.2.2 that the feature chosen using mutual information corresponds to better discriminability.

Moreover, the average single neuron Bayesian decoding performance of 4 un-tuned neurons and the combined decoding performance of the 4 neurons are shown in Figure 4-7 using the leave-one-out cross-validation method [Cherkassky 1998]. The 4 un-tuned neurons are combined for decoding using the Bayesian classifier,

$$P(X \mid V) = \prod_{i=1}^{4} \frac{P(v_{neuron\ i} \mid X)P(X)}{P(v_{neruon\ i})},$$

where X is the class label, $V=\{v_{neruon\ 1}, \ldots v_{neuron\ 4}\}$ is the feature vector for all 4 neurons, $P(X|V)$ is the posterior probability, $P(X)$ is the prior probability of X, and $P(V|X)$ is the likelihood of V given X, and

$$\tilde{X} = \arg\max_{X} \{P(X \mid V)\}.$$

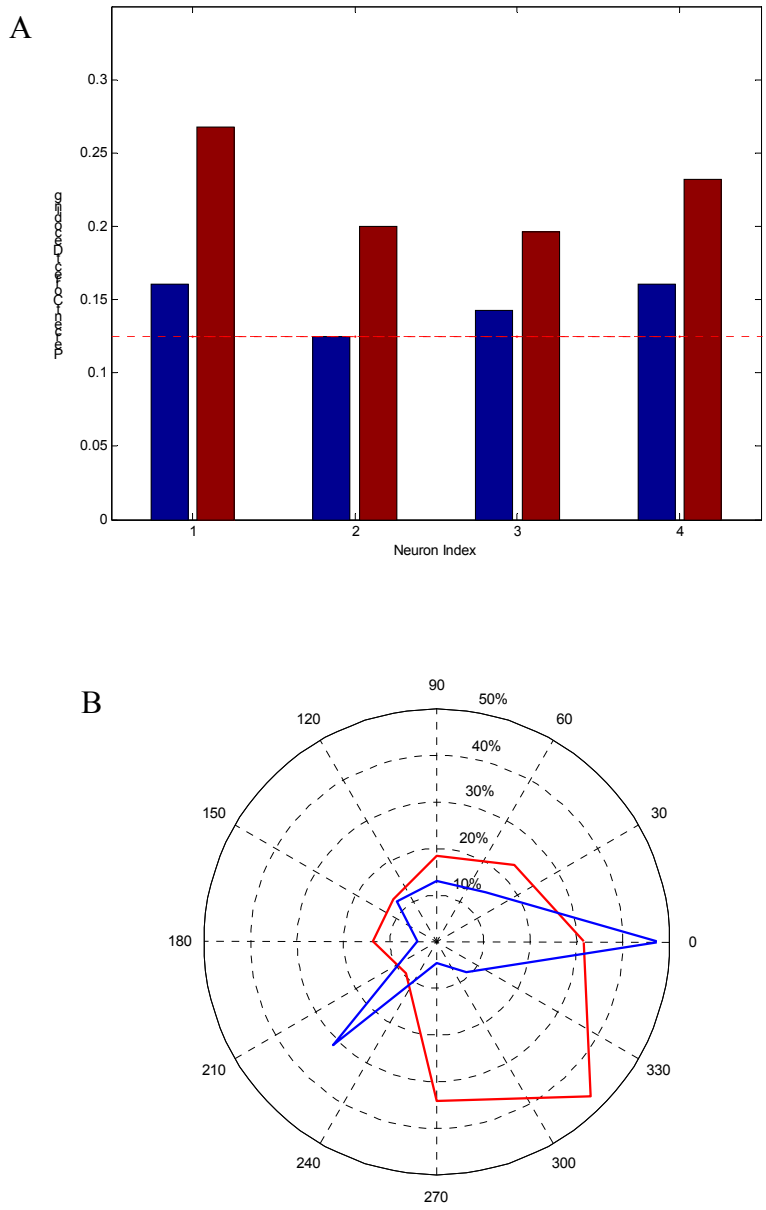

Figure 4-7 Comparison of 8-reach direction decoding performance

A) Single neuron average decoding performance of 8-reach directions.

The x-axis indexes the 4 neurons, and the y-axis marks the correct classification in percentage/100. The blue bar indicates the average correct decoding performance achieved using mean firing rate. The red bar indicates the average decoding performance achieved using the wavelet packet search algorithm with the score function being I_Q^{Mod}. And the red dash-line indicates the chance, which is 12.5%.

B) 4 neurons' combined decoding performance of the 8 reach directions.

Every 45 degree represents a reach direction, and the radius marks the correct decoding percentage. The blue line is the performance achieved using mean firing rate, and the red line is the performance by the optimal feature method.

The above figure demonstrates that the wavelet packet method consistently out-performs the mean firing rate. In Figure 4.7A, the individual neuron's average decoding performance is shown with chance at 12.5%. The feature extraction method improves the decoding performance by 5 to 7 percentage point, which translates to a 20% percent increase over the mean firing rate performance. In Figure 4.7B, the combined decoding performance of the 4 neurons using the Bayesian classifier at each reach direction is displayed. Although mean firing rate out-performs the feature extraction method at two directions, on average the feature extraction method still improves the average performance by 40% over the mean firing rate method. This average performance agrees with the discriminating property of mutual information as it quantifies the average decodability over all classes. This figure confirms that using the optimal wavelet packet feature allows for more accurate decoding performance over mean firing rate.

4.4 Conclusion

Decoding discrete stimulus parameters is an important step towards building practical neural prosthetic systems. In addition, better decoding also potentially enables a better understanding of the underlying neural code. This chapter presents a Haar wavelet packet based feature selection method for decoding. Under the framework of Haar wavelet packets, a set of naïve features, which are the wavelet packet projection coefficients of the spike trains, are first generated. Then this method takes advantage of

the special properties of the Haar wavelet packet functions and the tree hierarchy of the features and subsequently prunes the tree. When coupled with a discriminability score function, the pruning process extracts the most informative features, namely the ones with the highest decodability. The proposed discriminability score is the mutual information between the stimulus parameters and the features. Its relationship to the Bayesian classifier and its statistical properties make it an ideal candidate for the score function. Because this method goes beyond the common practice in the neuroscience community where mean firing rate is treated as the only feature, decoding performances using both mean firing rate and the optimal features are compared on surrogate and actual neural data. We conclude that this method generally improves the decoding performances when the optimal feature is used instead of the mean firing rate when the underlying classification rule is the Bayesian classifier.

Chapter 5 Decoding the Cognitive Control Signals for Prosthetic Systems

5.1 Introduction

Earlier chapters studied a general frame work and a computation methodology for decoding reach directions from neuronal spike trains. However, to be practically successful, an autonomous prosthetic control system requires more than just directional information. High-level cognitive control signals are another important component. Here, the high level cognitive states include, but are not limited to the idling state before reach, as well as the execution of the reach movement. Although the process of including cognitive states in a prosthetic control systems is relatively new, similar ideas have been explored extensively in areas such as speech recognition and discrete control systems where finite state machine and hidden Markov model are the main analytical tools applied [Jelinek 1998, Cassandras 1999, Viterbi 1967, Savage 1989, Rabiner 1989, Alur 1994, Brandin 1994, Allur 1994]. The state transition rule naturally allows for incorporating external states into the driving algorithm for the prosthetic system.

Before extending a formal study of this topic, let us first revisit the brain area of interest, the Parietal Reach Region (PRR). The PRR of the posterior parietal cortex (PPC) is located at an early stage in the sensory-motor pathway. It is closely related to sensory areas, particularly visual areas, and projects to limb movement areas within the frontal lobe [Johnson 1996, Andersen 1997]. Many properties of PRR make it an attractive source of plan activity to derive cognitive control signals. First, PRR plan activity is selective for arm movements and persists until a reach is initiated [Snyder et al., 1997].

This selectivity is critical if a prosthetic limb is to move according to arm movement plans. The persistence of activity during planning does not require an actual movement; thus this area codes the "thoughts" to move. In addition, during sequential reaching to two memorized locations, PRR plan activity codes just the next intended reach [Batista, 2001]. This simplifies the interpretation of activity in this region for prosthetic control since plan activity reflects the upcoming movement, not any or all planned movements. These properties suggest that intended movement activity from PRR may be well suited for generating high-level, cognitive control signals for prosthetic applications. Therefore, the spike signals from PRR are used to harvest the necessary control and cognitive signals that are needed to command a prosthetic device.

In the subsequent sections, we first model the sequence of actions in a reach movement as a finite state machine. Then different transition rules are studied and compared against each other. And finally the chapter concludes by describing how high-level, cognitive control signals can be used to control external devices such as a robot limb or a computer [Wolpaw 2000; Kennedy 2000, Shenoy 2003]. The work presented in this chapter is largely a version of the work found in *Neural prosthetic control signal from plan activity* in *NeuroReport 14: 591:596*.

5.2 Finite State Machine Modeling of Reach Movement

The spike data are analyzed from the experimental setup described in Chapter 2, in which action potentials, eye movements and push-button state are recorded while two monkeys

perform a delayed center-out reaching tasks. Figure 5.1 plots the response of a PRR neuron during repeated reaches to the memorized location of a flashed visual target.

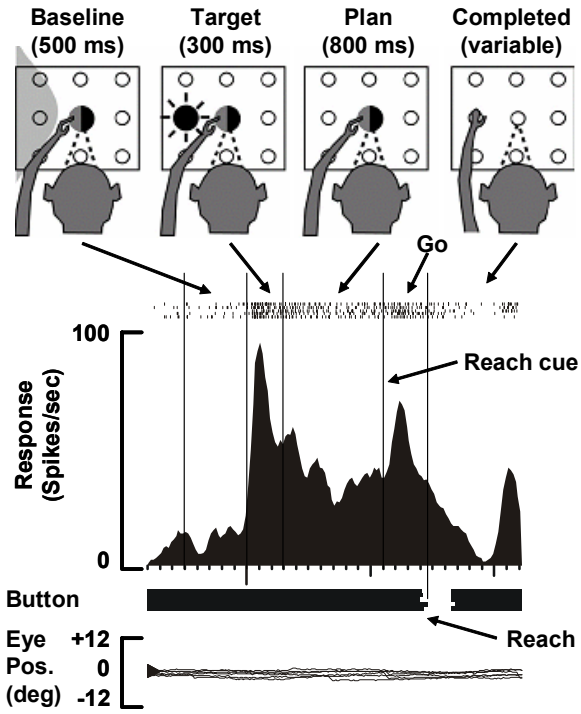

Figure 5-1 Parietal reach region (PRR) neural activity during the delayed, center-out reaching task

Three periods of neural activity are of particular interest: a *baseline* period preceding target presentation, a *plan* period following target presentation but preceding the reach cue, and a pre-movement or *go* period following the reach cue but preceding the onset of the arm movement. *Plan* and *go* period activity levels vary with the location of the flashed visual target, which specifies the goal of the arm movement. Figure 5.2 plots the average plan period response of 41 neurons from PRR of the right hemisphere of one monkey (DNT), recorded sequentially while reaching in eight different directions. Most neurons are tuned for a particular goal direction, with other directions eliciting weaker plan period activity. These three distinctive periods provide the necessary structural

information on the reach movement sequence. This information is especially important for a prosthetic system that relies heavily on the control signals extracted from the neural activities. Proper knowledge of these cognitive states not only provides extra control parameters for practical implementation of the prosthetic devices, but also reveals how PRR prepares and reacts to a reach movement.

In order to construct a robust autonomous prosthetic system, we also define the following objects. The *direction classifier* uses spike data from the past 500 ms to estimate the probability that a reach is being planned to each of the eight directions, and the most probable reach direction is then selected. The *period classifier* uses spike data from the past 250 ms to estimate the probability that PRR is currently in a *baseline*, *plan* or *go* period (see Figure 5.1), and then the most probable class is selected using the Bayesian classifier. Finally the *interpreter* takes in the series of *baseline*, *plan* and *go* classifications, generated by the *period classifier* as time evolves, and determines when a reach should be executed. It must also take in where the reach should be directed from the *direction classifier* and finally issue the high-level control signal stating: reach here, reach now.

Having introduced the concepts of *period*, *period classifier*, and *direction classifier*, we now focus on the function and operation of the *interpreter* (Figure 5.2C).

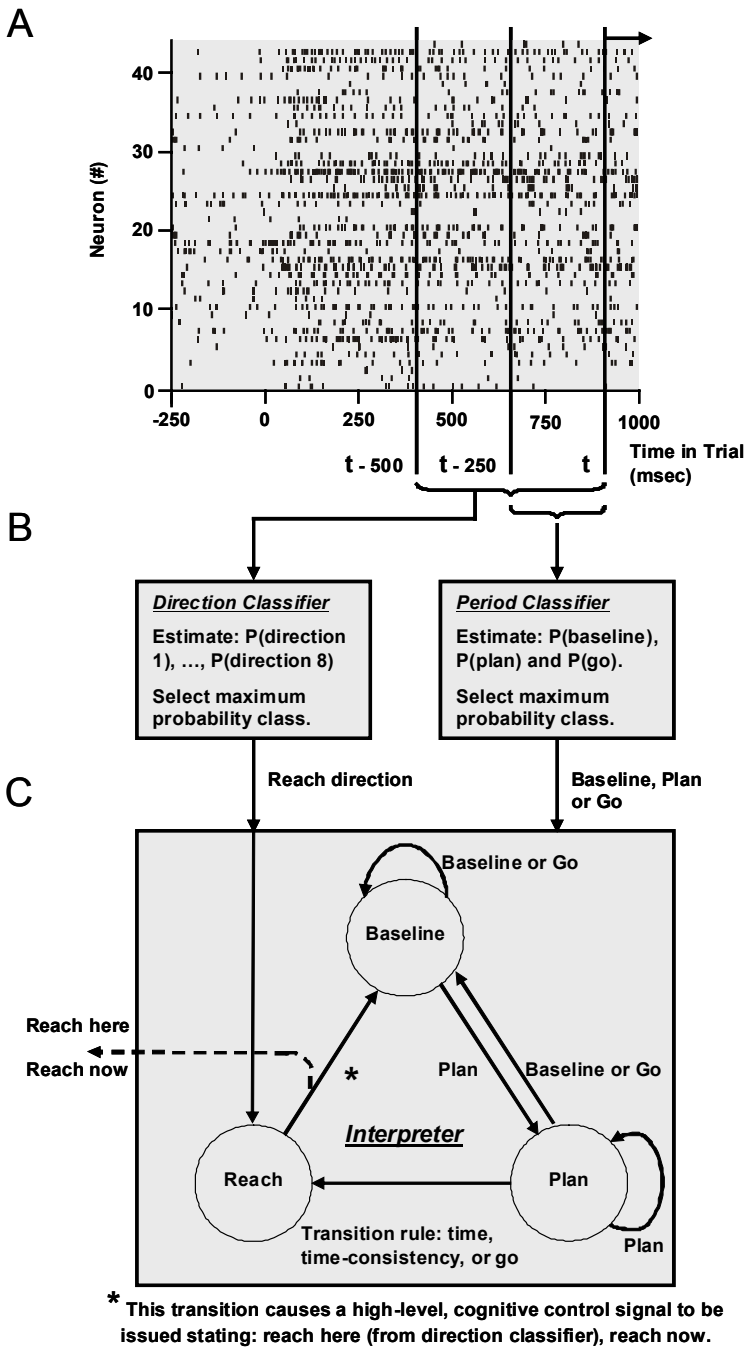

Figure 5-2 Computational architecture for generating high-level, cognitive control signals from PRR pre-movement, plan activity

(A) Spike raster for each PRR neuron contributing to the control of the prosthetic device as a function of time in the delayed, center-out reach task. A single trial is illustrated and the visual target, specifying the eventual reach goal, occurs at 0 ms. The onset of arm movement occurs after 1100 ms (not shown). (B) *Classifiers* use neural activity from finite-duration sliding analysis windows to estimate the direction of arm movement (*direction classifier*) and the current neural/behavioral period (*period classifier*). Both *classifiers* first calculate the probability of each class, and then select the most probable class for subsequent use. (C) The *interpreter* receives the stream of period

classifications (i.e., baseline, plan or go) from the *period classifier* and the stream of real direction classifications (e.g., downward reach) from the *direction classifier*. The *interpreter* consists of a finite state machine that transitions among three states (baseline, plan and reach) according to some transition rules.

Again, the first function the *interpreter* must perform is to determine when a reach should be executed given the series of baseline, plan and go classifications from the *period classifier*. We implemented the *interpreter* with a finite state machine consisting of three states: baseline, plan and reach. Importantly, although these states have similar labels to, and have certain relationships with, the *period classifier* outputs (i.e., baseline, plan and go period classifications) they are distinct. The period classifications govern, in part, the transitions between states.

The *interpreter* starts in the baseline state and, as shown in Figure 5.2C, can transition to the plan state or return to the baseline state each time the *period classifier* issues another period classification. A baseline or go period classification keeps the *interpreter* in the baseline state, while a plan period classification advances the *interpreter* to the plan state. Once in the plan state, a baseline- or go-period classification will return the *interpreter* to the baseline state. The reason for this operating logic will become clear when we discuss below the possible rules for transitioning the *interpreter* from the plan state to the reach state. Once the reach state is achieved the *interpreter* automatically transitions back to the baseline state, and simultaneously issues a high-level, cognitive control signal commanding an immediate reach to the location given by the *goal classifier* (Figure 5.2C, asterisk).

The question of when to transition the *interpreter* from the plan state to the reach state, and subsequently triggering an arm movement, can be answered by considering the behavioral task instructions and go period classifications. We now summarize the logic of three different transition rules, as well as the results we obtained using these rules, to show how increasingly sophisticated rules can potentially improve prosthesis control performance.

1. Time transition rule. If the behavioral task instruction to the subject is simply "plan a reach to a particular location for half a second," then a prosthetic system can safely execute an arm movement after detecting 500 ms of plan activity. In other words, the *interpreter* can transition from the plan state to the reach state when the *period classifier* issues 500 ms of contiguous plan classifications. Importantly, with this strategy the subject could abort an arm movement by ceasing to plan at any time before 500 ms or shift the reach target by simply changing his/her planned reach location before 500 ms has passed. We term this the "time" transition rule. While this is the typical behavior with the time criterion transition rule, particularly with large neuron populations and for reaches to particular locations, this rule can error by failing to transition to the reach state before the end of the trial's experimental data or by executing a reach to the wrong goal location.

The *interpreter* begins in the baseline state and correctly stays in the baseline state during the phasic-response period mentioned previously (~100-400 ms following target presentation). This is because the erroneous go period classification occurs after only a

brief period (less than 500 ms) of plan. The *interpreter* then correctly enters the plan state and remains in this state, as long as the *period classifier* issues plan period classifications, until the minimum length of continuous plan classification (500 ms) is surpassed causing a transition to the reach state.

2. Time-consistency transition rule. A simple extension of the prior transition rule can address these concerns by adopting the conservative view that it is better not to execute a reach at all than to reach in the wrong direction. By adding the constraint that the *period classifier's* plan classifications must also specify a given goal direction throughout the required plan period (500 ms) we effectively impose a plan-stability requirement. We term this the "time-consistency" transition rule. Importantly, the *period classifier*, which employs a 250 ms sliding window, can also estimate goal location using response models and estimation methods analogous to those in the familiar *direction classifier*.

3. Go transition rule. While the previous two transition rules perform well for certain applications, and importantly they do not rely on neural signals associated with movement execution, we would also like to be able to produce a larger absolute number of correct reaches. We can achieve this by replacing the previous stability constraint with a requirement that the *period classifier* issue a go period classification, after plan period classifications have been issued continuously for 500 ms, in order to transition from the plan state to the reach state. We term this the "go" transition rule. Using a neural "go signal" could afford the subject an additional opportunity to abort a planned reach by

withholding the go command, or the possibility of reducing the length of the plan period on some trials.

5.3 Results

In this section, we apply the aforementioned state transition rules as well as the interpreter rules to neural data recorded in PRR. The experimental paradigm and recording technique remain the same [Batista 1999]. We use the Bayesian classifier with a uniform prior probability distribution, to estimate reach parameters. Our assumptions were Poisson spike statistics and statistical independence between cells, but explicit models of tuning to the various parameters were not assumed [Zhang et al., 1998]. To reconstruct the planned reach direction, we defined the scalar $X = (1, 2, \ldots, 8)$ to be the reach direction and the vector $\mathbf{n} = (n_1, n_2, \ldots, n_N)$ to be the spike count from each neuron (n_i) during a time interval (τ). Combining the expression for the conditional probability for the number of spikes **n** to occur given a plan to reach direction x with Bayes' rule yields the following expression for the conditional probability of x given **n**:

Equation 5.1
$$P(X \mid \mathbf{n}) = C(\tau, \mathbf{n})\, P(X) \left(\prod_{i=1}^{N} f_i(X)^{n_i} \right) \exp\left(-\tau \sum_{i=1}^{N} f_i(X) \right)$$

The normalization factor $C(\tau,\mathbf{n})$ ensures that the sum of the probabilities equals one. $P(X)$ is the prior probability for reaches in each direction, and is uniform by experimental design, and the mean firing rate of the i^{th} neuron while planning a reach to direction X is

$f_i(x)$. The estimated reach direction, $\hat{X}$, was taken to be the one with the highest probability.

$$\hat{X} = \underset{X \in \{1,2,...8\}}{\operatorname{argmax}}\left(P\left(X \mid \mathbf{n}\right)\right)$$

A similar procedure was used to estimate the response distributions for the time-course analyses, but with the following variations. After selection of the random subset of cells and the exclusion of a single random trial from each cell, the remaining trials were divided into 3 epochs: baseline, plan period, and pre-execution period (-600 to 0, 300 to 1000, and 1100 to 1350, respectively). The trials from each direction, for each cell, and in each epoch were concatenated, and the data were sampled with 250ms long moving windows with 50ms time steps. The baseline epoch was concatenated across all directions. Additionally the plan epoch was also sampled using 500ms windows rather than 250 ms windows. The mean of each epoch was used as the parameter for the single multidimensional Poisson distribution for the baseline period, and for each of the 8 multidimensional distributions for each direction in the 3 other epochs (the 250ms sampled memory epoch, the 500ms sampled memory epoch and the pre-execution period). Test-data firing rates were measured in 250ms windows, advanced 50 ms at each time step, through the duration of the test trial. The most probable condition (baseline, one of 8 plan directions, or one of 8 execution directions) was estimated independently in each time step as above. The direct results of this classification process are shown in Figure 5.3.

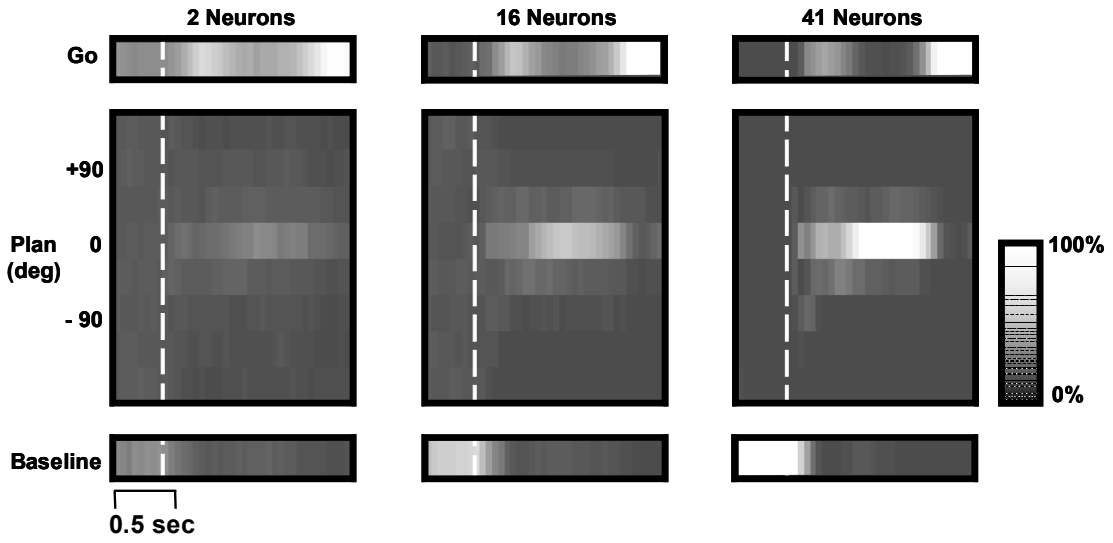

Figure 5-3 Classification time courses, averaged over all reach goal locations, for three different neural population sizes (2, 16 and 41 neurons from monkey DNT)

These time courses reflect, statistically, the output of the *period classifier* in the delayed center-out reach task. Each classification time course has three sections: the lower row corresponds to baseline period classification, the middle region corresponds to the eight possible reach-plan classification locations (the correct goal location is plotted at 0°), and the upper row corresponds to go classification. White indicates a 100% classification rate, black indicates a 0% classification rate, and the dashed-white vertical line indicates the onset of target presentation. Performance decreases as the number of neurons in the population is reduced.

Next we implement the *Interpreter* in order to enforce different rules to the above classifier. The results are summarized in Figure 5.4.

1. Time transition rule. Figure 5.4A shows the percent of trials achieving the reach state, and thus executing a reach, for a range of population sizes. Figure 5.4B indicates the percent of these trials that executed reaches in the correct direction for a range of population sizes. Ideally all trials would execute reaches, as all of our experimental data are from successful reach trials, and all trials would reach in the correct direction. Although this transition rule successfully executes reaches for most trials (Fig. 5.4A),

many of the reaches go in the wrong direction (Fig. 5.4B). These errors are due to *direction classifier* miss-classifications, and are most likely caused by low signal to noise ratios. If errors were caused by drifts in plan or volition then the prediction accuracy would not be expected to increase dramatically by adding more neurons to the estimate.

2. Time-consistency transition rule. Figure 5.4 also summarizes the performance of this transition rule. As expected, fewer trials now execute reaches (Fig. 5.4A) but those that do tend to reach in the correct direction more often (Fig. 5.4B).

3. Go transition rule. Figure 5.4 illustrates the performance. The period of time used by the *direction classifier* to estimate the reach direction, which is the 500 ms directly preceding the go period classification, tends to be slightly later than with the previous two transition rules. This is because the go period classification can occur up to several hundred milliseconds after the plan duration criterion has been met. This accounts for the increased percentage of reaches to the correct location (Fig. 5.4B). This algorithm executes an intermediate number of reaches, as compared to the other two transition rules (Fig. 5.4A), with good performance arising from the readily detected and classified go activity.

A

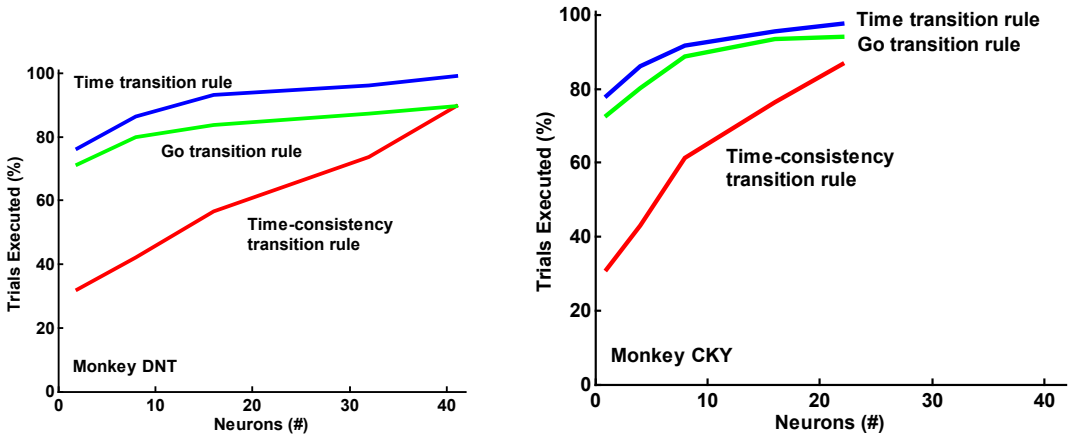

B

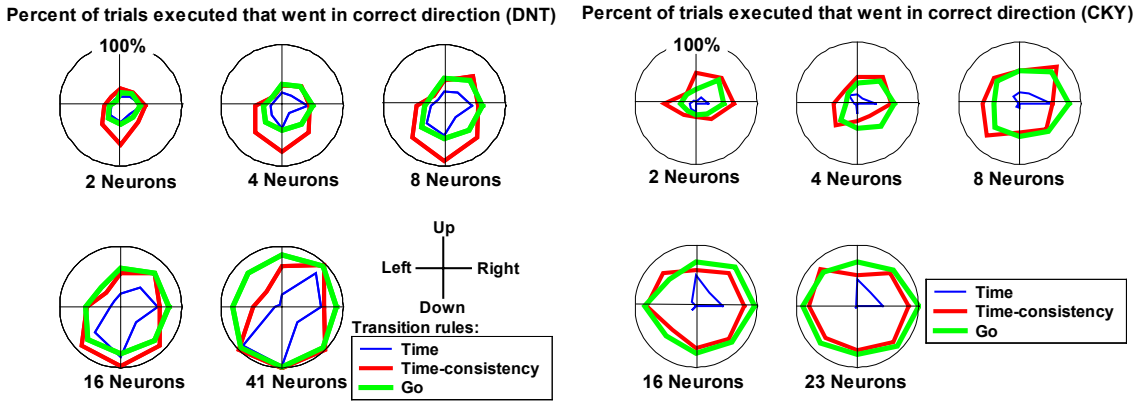

Figure 5-4 *Interpreter* performance characteristics

The *interpreter* was characterized, separately, while using the time, time-consistency, and go transition rules (color coded). (A) Percent of trials achieving the *interpreter's* reach state, thereby triggering a reach, as a function of the number of neurons in the population. Perfect performance (100%) means that all trials executed a reach to some goal location, but not necessarily to the correct goal location. (B) Percent of trials that executed a reach to some goal location that *did* reach to the correct goal location. Perfect performance (100%), meaning that all trials executed went to the proper location, is plotted as a circle in all sub-panels. Each sub-panel shows performance for a different number of neurons in the analysis population. In both panels (A) and (B) neurons from animals DNT and CKY were used to generate the performance curves appearing to the left and right, respectively. Interpreter performance, including the relative performance of the three transition rules, was similar in both monkeys.

5.4 Conclusion

Although decoding stimulus and behavior parameters have been in existence for many years, there does not yet exist a neural-prosthetic architecture that is optimal for all plausible prosthetic applications. To explore the feasibility of using pre-movement neural signals from PRR to generate high-level cognitive control signals, a computational architecture is developed and tested in this chapter. This part of an envisioned neural prosthetic system estimates, from PRR neural activity, when an arm movement is being planned (*period classifier*), the direction of the planned movement (*direction classifier*), and when the arm should move (*interpreter*). The resulting computations issue a cognitive control signal with two parts: reach here and reach now. Thus using the neural signal from PRR, it is sufficient to extract the necessary control signals for operating a neural prosthetic. This structured decoding approach offers a first look at the possibility of building an autonomous prosthetic device based completely on the information in the neural data.

Chapter 6 Conclusion

Inspired by the considerable success of cochlear implants, tremor-control devices and other neural-prosthetic systems aimed at *delivering* signals to the nervous system, research aimed at *reading out* neural signals for prosthetics applications has intensified in recent years. While the concept of *translating* neural activity from the brain into control signals for prosthetic systems has existed for decades, substantial progress toward realizing such systems has been made only relatively recently. This progress has been fueled by advances in our understanding of neural coding, as well as by advances in forming stable electrical interfaces with neurons and computational technologies for processing neural signals in real time.

One interesting application of the neural prosthetic system is a prosthetic arm that is connected directly to motor or pre-motor area of the brain. This allows direct control of the prosthetic arm by mere thoughts of the user. In other words, one can control peripheral devices just by thinking where to reach. Such a system could be especially important for many locked-in patients or severe spinal cord injury sufferers [Katz 1992]. In addition, successful construction of this system should also shed light on the underlying neural coding of the behavior parameters.

As this endeavor spans many different disciplines and research subjects, this thesis in particular focuses on obtaining the necessary control signals for a prosthetic system such as reach directions and cognitive states. In Chapter 3, a novel approach to characterize spike trains is proposed. This approach determines the *Poisson-ness* of a spike train at

different scales while taking advantage of the multi-scale capability of wavelet packets, a relatively new signal processing technique. Under this approach, the spike trains are projected onto wavelet packets and the distributions of the projection coefficients are analyzed. It allows us to assess *Poisson-ness* from different scales. The *Poisson-ness* is an especially important quantity for decoding because if the spike train is indeed Poisson in nature, then the ubiquitous mean firing rate measure is the only relevant feature.

As seen from the examples of Chapter 3, not all neurons exhibit a Poisson nature. Therefore, it is necessary to devise a method that searches for the most discriminating feature(s) towards decoding. Chapter 4 first uses the Haar wavelet packet to construct a naïve feature set. Because of the time domain properties of the Haar wavelet packet functions, these features have intuitive biological interpretations that are appealing to researchers in the neuroscience community. Then of all the features, the most informative ones are selected using an optimal feature search technique. The technique prunes the wavelet packet tree while using mutual information as a score function to rank the decodability of each feature. When combined with the Bayesian classifier, this method returns improved decoding performance versus approaches based on the firing rate. The method was tested on both artificial data and actual neuronal data from PRR, and compared to mean firing rate decoding.

Besides decoding the estimated reach directions from PRR signals, additional *cognitive parameters* are necessary for building an autonomous prosthetic device. For a minimally autonomous robotic device, Chapter 5 defines the behavior states to include a *baseline*

state, reach *planning* states, and the reach execution *go* state. When combined with an *Interpreter* that acts on the classification results of these states, it returns an efficient algorithm that extracts the necessary cognitive control parameters. Experimental data collected from PRR while the animal is performing a sequence of actions are subjected to this method while we compare different state transition rules.

Although the work in this thesis largely focuses on decoding discrete stimulus parameters from spike data, the decoding framework and technique can be extended to other types of signals such as LFP and EEG. In addition, it is possible that more complicated trajectory decoding problem may be cast in the discrete parameter problems as well because studies have shown that PRR encodes the next movement target. Therefore, it is conceivable that one can discretize a trajectory into a set of sequential movement targets though further experiments and studies are necessary to validate this suggested approach.

Bibliography

A

Abbott, L.F., Decoding neuronal firing and modeling neural networks, *Quarterly Review of Biophysics*, 27:291-331 (1994)

Alur, R. and D.L. Dill, A Theory of Timed Automata, *Theoretical Computer Science* No. 126, pp183-235, 1994

Brandin, B. and W.M. Wonham, Supervisory control of timed discrete event systems, *IEEE Transactions on Automatic Control*, Vol. 39, No. 2, pp 329-342, 1994

Abeles, A. and M. Goldstein, Multispike Train Analysis, *Proceedings of the IEEE*, vol. 65, pp 762-773, 1977

Andersen, R.A., L.H. Snyder, D.C. Bradley, and J. Xing, Multimodal representation of space in the posterior parietal cortex and its use in planning movements, *Annual Review of Neuroscience,* 20:303-330, 1997

B

Brown, E.N., L.M. Frank, D. Tang, M.C. Quirk, M.A. Wilson, A statistical paradigm for neural spike train decoding applied to position prediction from ensemble firing patterns of rat hippocampal place cells, *Journal of Neuroscience*, Sept. 15; 18(18): 7411-25, 1998

Batista, A.P., C.A. Buneo, L.H. Snyder and RA Andersen, Reach plans in eye-centered coordinates, *Science*, 285:257-260, 1999

Batista, A.P., and Andersen, R.A., The parietal reach region codes the next planned movement in a sequential reach task, *Journal of Neurophysiology, 85*:539-544, 2001

Brandman, R. and M.E. Nelson, A simple model of long-term spike train regularization, *Neural Computation,* 14:1575-1597, 2002

C

Cherkassky, V. and F. Mulier, *Learning from Data - Concepts, Theory and Methods,* Wiley, New York, 1998

Cover, T. and J. Thomas, *Elements of Information Theory*, Wiley, New York, 1991

Cassandras, C. and S. Lafortune, *Introduction to Discrete Event Systems*, Kluwer Academic Publishers (Norwell, MA), 1999

D

Daubechies, I., *Ten Lectures on Wavelets*, SIAM, Philadelphia, PA, 1992

Devroye, L, L. Gyorfi, and G. Lugosi*, A Probabilistic Theory of Pattern Recognition*, Springer Verlag, 1996.

Donoghue J.P., Connecting cortex to machines: recent advances in brain interfaces. *Nature Neuroscience* 5 Supplement: 1085 – 1088, 2002

Donoho, D.L., & I.M. Johnstone, Ideal denoising in an orthonormal basis chosen from a library of bases. *Compt. Rend. Acad. Sci. Paris Ser. A*, 319, 1317-1322, 1994

E

F

Fisher R.A., The use of multiple measurements in taxonomic problems. *Annals of Eugenics* 7, pages 179-188, 1936

Florence, S.L., H.B. Taub, and J.H. Kaas, Large-scale sprouting of cortical connections after peripheral injury in adult macaque monkeys, *Science*, 282(5391): p. 1117-1121, 1998

G

Georgopoulos, A.P., A. Schwartz, and R.E. Kettner, Neuronal population coding of movement direction, *Science,* 233:1416-1419, 1986

Georgopoulos A.P., R.E. Kettner, and A Schwartz, Primate motor cortex and free arm movements to visual targets in three-dimensional space, II, Coding of the direction of movement by a neuronal population, *Journal of Neuroscience* 8:2928-2937, 1988

Gabbiani, F. and C. Koch, *Principles of Spike Train Analysis Methods in Neuronal Modeling: From Synapses to Networks,* C Koch and I Segev, eds., 2. edition, . MIT Press: Cambridge, MA 0:313-360, 1998

Greenwood, P., *A Guide to Chi-Squared Testing*, Wiley, NY, 1996.

H

Humphrey, D.R., *Electrophysiological Techniques*, Society for Neuroscience, Atlanta, 1979

I

Isaacs, R., D. Weber and A. Schwartz, Work toward real-time control of a cortical prothesis, *IEEE Trans. Rehabil. Eng.* 8:196-198, 2000

J

Jelinek, F., *Statistical Methods for Speech Recognition*, MIT Press, Cambridge MA, 1998

Johnson, D.H. and R.M. Glantz, When does interval coding occur? CNS, 2003

Johnson D.H., C.M. Gruner, K. Baggerly, and C. Seshagiri, Information-theoretic analysis of neural coding, *Journal of Computational Neuroscience*, 10:47-69, 2001

Johnson D.H., Point process models of single-neuron discharges. *Journal of Computational Neuroscience*, 3:275-299, 1996

Johnson, P.B., S. Ferraina, L. Bianchi, and R. Caminiti, Cortical networks for visual reaching: physiological and anatomical organization of frontal and parietal lobe arm regions. *Cerebral Cortex,* 6:102-119, 1996

K

Kralik J.D., D.F. Dimitrov, D.J. Krupa, D.B. Katz, D. Cohen, and A.L. Nicolelis, Techniques for long-term multisite neuronal ensemble recordings in behaving animals, *Methods* 25, 121-150, 2001

Kaas, J.H., Sensory loss and cortical reorganization in mature primates, *Progress in Brain Research*, 138: p. 167-176, 2002

Katz, R.T., Long-Term survival, prognosis, and life-care planning for 29 patients with chronic locked-in syndrome, *Arch. of Physical Medicine and Rehabilitation*, 73(5): p. 403-408, 1992

Kolaczyk, E.D., Non-parametric estimation of Gamma-ray burst intensities using Haar wavelets, *The Astrophysical Journal*, Vol. 483, 340-349, 1997

Kennedy, P.R., R.A.E. Bakay, M.M. Moore, K. Adams, and J. Goldwaithe, Direct control of a computer from the human central nervous system, *IEEE Transactions on Rehabilitation Engineering* 8, 198-202, 2000

L

Learned, R. and A.S. Willsky, A wavelet packet approach to transient signal classification, *Applied and Computational Harmonic Analysis* 2, 265-278, 1995

Lewicki, M.S., A review of methods for spike sorting: the detection and classification of neural action potentials, *Network: Computation in Neural Systems* 9(4): R53-R78, 1998

M

Moran, D.W. and A.B. Schwartz, Motor cortical representation of speed and direction during reaching, *Journal of Neurophysiol* 82(5): 2676-2692, 1999

Mallat, S., *A Wavelet Tour of Signal Processing*, Academic Press; 2nd edition, 1999

Mallat, S., G. Papanicolaou, and Z. Zhang, Adaptive covariance estimation of locally stationary processes, *Annals of Statistics*, vol. 26, no. 1, 1998

Meeker, D., K.V. Shenoy, S. Cao, B. Pesaran, H. Scherberger, M. Jarvis, C.A. Buneo, A.P. Batista, S.A. Kureshi, P.P. Mitra, J.W. Burdick, RA Andersen, Cognitive control signals for prosthetic systems. *Society For Neuroscience* 27, 2001

Meeker D., K.V. Shenoy, S. Kureshi, S. Cao, J. Burdick, B. Pesaran, P. Mitra, A. Batista, C. Buneo, B. Gillikin, D. Dubowitz, R.A. Andersen, Toward adaptive control of neural prosthetics by parietal cortex. *Neural Information and Coding Workshop*, 2000

Meeker, D. and R.A. Andersen, Rapid plasticity in the parietal reach region demonstrated with a brain-computer interface, *Society For Neuroscience.* 29, 2003

N

Nicolelis, M., The amazing adventures of robotrat, *Trends in Cognitive Sciences* 6: 449-450, 2002

Nicolelis, M., Actions from thoughts, *Nature,* 409:403-407, 2001

Nowak, R., Multiscale Hidden Markov Models for Bayesian Image Analysis, *Bayesian Inference in Wavelet Based Models*, Springer-Verlag, 1999

Nenadic Z. and J.W. Burdick, Spike detection using continuous wavelet transform, manuscript in preparation, 2003

O

Oppenheim, A.V. and R.W. Schafer, *Digital Signal Processing*, Prentice-Hall, Englewood Cliffs, NJ, 1975

Oweiss, K.G., *Multiresolution analysis of multichannel neural recordings in the context of signal detection, estimation, classification and noise suppression*, Ph.D. Thesis, University of Michigan, Ann Arbor, May 2002

Oweiss, K.G. and D.J. Anderson, Noise Reduction in Multichannel Neural Recordings using a new array wavelet denoising algorithm, N*eurocomputing*, vol 38-40, pp.1687-1693, 2001

P

Parzen, E., On the estimation of probability density function and the mode, *The Analysis of Mathematical Statistics* 33, 1965

Percival, D.B. and A.T. Walden, *Wavelet Methods for Time Series Analysis*, Cambridge University Press, 2000

Q

R

Ross S.M., *Stochastic Processes*, Wiley, New York, NY, 1994

Ross S.M., *Introduction to Probability and Statistics for Engineers and Scientists*, Wiley, New York, 2000

Reich, D.S., F. Mechler, K.P. Purpura, and J.D. Victor, Interspike intervals, recepive fields and information coding in primary visual cortex, *Journal of Neuroscience*, 20:1964-1975, 2000

Rabiner, L.R., A tutorial on hidden Markov models and selected applications in speech recognition*, Proceedings of the IEEE*, vol. 37 no. 2 pp57-86, 1989

S

Shannon, C.E. and W. Weaver, *The Mathematical Theory of Communication*, University of Illinois Press, Urbana, IL, 1959

Schwartz, A.B. and D.W. Moran, Arm trajectory and representation of movement processing in motor cortical activity, *European Journal of Neuroscience* 12(6):1851-1856, 2000

Schwartz A.B., R.E. Kettner, and A.P. Georgopoulos, Primate motor cortex and free arm movements to visual targets in three-dimensional space I. Relations between single cell discharge and direction of movement, *Neuroscience* 8:2913-2927, 1988

Steveninck, R., G. Lewen, S.P. Strong, R. Koberle, and W.A. Bialek, Reproducibility and variability in neural spike trains, *Science* 275: 1805-1808, 2002

Sanger, T.D., Probability density estimation for the interpretation of neural population codes, *Journal of Neurophysiology*, 76(4):2790--2793. 11, 1996

Savage, J., *Models of Computation*, Addison-Wesley, Reading MA, 1989

Snyder, L.H., A.P. Batista, and R.A. Andersen, Coding of intention in the posterior parietal cortex, *Nature*, 386:167-169, 1997

Shenoy, K.V., D. Meeker, S. Cao, S.A. Kureshi, C.A. Buneo, A.P. Batista, J.W. Burdick, R.A. Andersen, Toward prosthetic systems controlled by parietal cortex. *Neural Information and Coding Workshop*, 2001

Shenoy, K.V., D. Meeker, S. Cao, S.A. Kureshi, B. Pesaran, C.A. Buneo, A.P. Batista, P.P. Mitra, J.W. Burdick, and R.A. Andersen, Neural prosthetic control signals from plan activity, *NeuroReport*, 14:591-596, 2003.

Strong, S.P., R. Koberle, R. Steveninck and W. Bialek, Entropy and Information in Neural Spike Trains, *Physical Review Letters* 80:197-201, 1998

Saito N., R.R. Coifman, F.B. Geshwind, and F. Warner, Discriminant feature extraction using empirical probability density estimation and a local basis library, *Pattern Recognition*, vol. 35, pp.2841-2852, 2002

T

Teich, M.C. and S.M. Khanna, Pluse-number distribution for the neural spike train in the cat's auditory nerve, *Journal of Acoustic Society of America*. 77:1110-1128, 1985

Stirzaker, D., *Elementary Probability*, Cambridge University Press, 1994

U

V

Viterbi, A.J., Error bounds for convolutional codes and an asymmetrically optimum decoding algorithm, *IEEE Transactions on Information Theory*, vol. IT-13 pp.260-67, 1967

Victor, J.D. and K.P. Purpura, Metric-space analysis of spike trains: theory, algorithms and application, *Network: Computation in Neural Systems* **8**: 127—164, 1997

Vapnik, V., *The Nature of Statistical Learning Theory*, Springer, Berlin, 1995

W

Wessberg, J., C. Stambaugh, J. Kralik, P. Beck, M. Laubach, J. Chapin, J. Kim, S. Biggs, M. Srinivasan, and M. Nicolelis, Real-time prediction of hand trajectory by ensembles of cortical neurons in primates, *Nature*, 408(6810):361-5, 2000

Wickerhauser, M.V., *Adapted Wavelet Analysis from Theory to Software*, Wellesley, MA, 1994

Wolpert, D.M. and Z. Ghahramani, Computational principles of movement neuroscience. *Nature Neuroscience*. *3*:1212-1217, 2001

X

Y

Z

Zhang, K., I. Ginzburg, B.L. McNaughton, and TJ Sejnowski, Interpreting Neuronal Population Activity by Reconstruction, *The American Physiological Society*, pp. 1017-1044, 1998.

Appendix 1: Proof of Proposition 3.1

The proof of this proposition proceeds by induction.

Step 1: First consider the scale $j = 1$. The wavelet packet coefficients $v_{01}, v_{02}, ..., v_{0T}$ at scale 0 are independent because of the independent increments property P1. By construction from the Pyramid Algorithm, we know that the child coefficients at scale j=1 are

$$\begin{aligned} v_{1,k} &= v_{0,2k-1} + v_{0,2k} \\ v_{1,k+\frac{T}{2}} &= v_{0,2k-1} - v_{0,2k} \end{aligned}, \text{ for } k = 1,2,...,\frac{T}{2}$$

Thus the joint probability between any coefficients v_{11}, v_{12} can be written as,

$$\begin{aligned} P(v_{11}, v_{12}) &= P(v_{01} + v_{02}, v_{03} + v_{04}) \\ &= P(v_{01} + v_{02} = v \mid v_{03} + v_{04} = v')P(v_{03} + v_{04} = v') \\ &= \sum_x P(v_{01} = x, v_{02} = v - x \mid v_{03} + v_{04} = v')P(v_{03} + v_{04} = v') \\ &= \sum_y \sum_x P(v_{01} = x, v_{02} = v - x \mid v_{03} = y, v_{04} = v' - y)P(v_{03} = y, v_{04} = v' - y) \\ &= \sum_x P(v_{01} = x, v_{02} = v - x) \sum_y P(v_{03} = y, v_{04} = v' - y) \end{aligned}$$

The last equality is due to the independence given by property P2. Here x and y describe the range of the coefficients at scale *j=1*, where Range(v_{1k}) = *{-1 0 1}*. Continuing, we have:

$$\begin{aligned} P(v_{11}, v_{12}) &= P(v_{01} + v_{02} = v)P(v_{03} + v_{04} = v') \\ &= P(v_{11})P(v_{12}) \end{aligned}$$

where the last step is a consequence of the parent-child relationship in the Pyramid algorithm. We can generalize the above result to all the members of the low pass child to

show that all the coefficients $v_{11}, v_{12}, ..., v_{1\frac{T}{2}}$ are mutually independent. Similarly, we can show the independence between all the members of the coefficients related to the high pass child $v_{1(\frac{T}{2}+1)}, v_{1(\frac{T}{2}+2)}, ..., v_{1T}$.

Step 2: To establish the induction, consider the wavelet packets and their coefficients at scale $j = j^*$. Assume all the coefficients

$$\left\{v_{j^*k}\right\}_{k=1+l\frac{T}{2^{j^*}}}^{(l+1)\frac{T}{2^{j^*}}},\ l = 0,1,...,2^{j^*-1}$$

at each node are mutually independent. We know from Step 1 that this is true for $j^*=1$.

Step 3: To proceed with the induction, assume the mutual independence of coefficients at scale j^*. Now consider scale j^*+1. Using the same approach as step 1 of the proof, at scale $j = j^*+1$ the coefficients associated with the low pass child node branched from the parent node at scale j^* have the following joint distribution,

$$\begin{aligned}
&P(v_{(j^*+1)1}, v_{(j^*+1)2}) \\
&\quad = P(v_{j^*1} + v_{j^*2}, v_{j^*3} + v_{j^*4}) \\
&\quad = P(v_{j^*1} + v_{j^*2} = v \mid v_{j^*3} + v_{j^*4} = v')P(v_{j^*3} + v_{j^*4} = v') \\
&\quad = \sum_x P(v_{j^*1} = x, v_{j^*2} = v - x \mid v_{j^*3} + v_{j^*4} = v')P(v_{j^*3} + v_{j^*4} = v') \\
&\quad = \sum_y \sum_x P(v_{j^*1} = x, v_{j^*2} = v - x \mid v_{j^*3} = y, v_{j^*4} = v' - y)P(v_{j^*3} = y, v_{j^*4} = v' - y) \\
&\quad = \sum_x P(v_{j^*1} = x, v_{j^*2} = v - x) \sum_y P(v_{j^*3} = y, v_{j^*4} = v' - y) \\
&\quad = P(v_{j^*1} + v_{j^*2} = v)P(v_{j^*3} + v_{j^*4} = v') \ = \ P(v_{(j^*+1)1})P(v_{(j^*+1)2})
\end{aligned}$$

We can further generalize the above result to all the members of the low pass child so that the set of coefficients $\left\{v_{(j^*+1)k}\right\}_{k=1+l\frac{T}{2^{j^*+1}}}^{(l+1)\frac{T}{2^{j^*+1}}}$, $l = 0,1,...,2^{j^*}$ are all mutually independent.

Similarly, we can show the independence between all the members of the high pass child of the parent node at scale j^*. Therefore, we have proven that the members of any child node, namely the leaf of the wavelet packet tree, are independent. □

Appendix 2

In the Section 4.2, we introduced mutual information as our score function and presented the feature selection strategy. To fully understand its effect, we investigate its associated discriminability in the finite sample setting. For simplicity, the analysis in this section is done specifically for binary classification. However, many of these ideas can be generalized to multiple-class problems.

An important question regarding mutual information as a measure is how it is related to the Bayesian classification error, E^*. Assume we have no prior knowledge about the classes, then the mutual information between the classes and the features are bounded by the following relationship [Devroye 1998],

Equation 2 $$1 + \log(1 - E^*) \geq I(v; X) \geq 1 - [E^* \log \frac{1}{E^*} + (1 - E^*) \log \frac{1}{1 - E^*}].$$

Figure 2 plots the bound on mutual information by the Bayesian classification error.

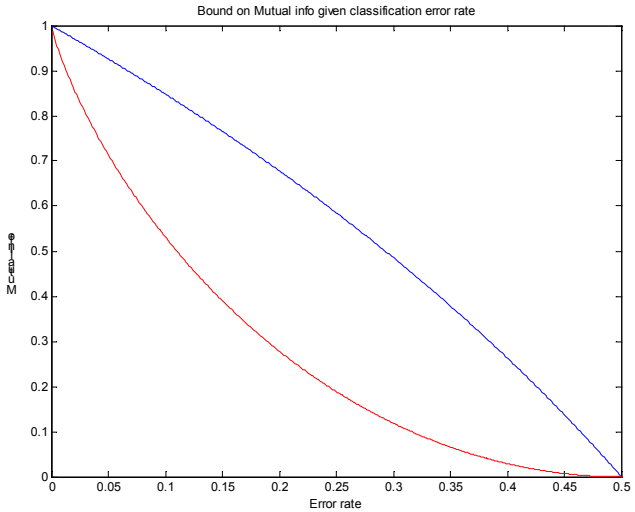

Figure A.0-1 Mutual information bounded by the Bayesian classification error E^*.

The red line corresponds to the lower bound and the blue line corresponds to the upper bound. X-axis is the error rate E^* *and y-axis marks the mutual information*

Evidently, large mutual information corresponds to a smaller classification error. Notice the bound is somewhat loose, i.e. a large range of mutual information can correspond to the same classification error. Then why does mutual information work well as a discriminability measure?

To address this question, E^* is first re-examined. Recall Equation 4, the classification error is defined as

$$\begin{aligned} E^* &= P(\widetilde{X} \neq X) \\ &= \sum_v P(\widetilde{X} \neq X \mid v) P(v) \\ &= \sum_v \min\{P(X=1 \mid v), P(X=0 \mid v)\} P(v) \end{aligned} .$$

Using the Bayes' rule, we can rewrite the above equation as,

$$E^* = \frac{1}{2} \sum_v \min\{P(v \mid X=1), P(v \mid X=0)\},$$

assuming the two classes are equally likely. With some algebraic manipulation, the above equation is re-formulated as

Equation 3

$$\begin{aligned} E^* &= \frac{1}{2} \sum_v [P_1(v) + P_0(v)] - |P_1(v) - P_0(v)| \\ &= 1 - \frac{1}{2} \sum_v |P_1(v) - P_0(v)| \end{aligned} ,$$

where for simplicity of notation, $P_1(v)$ and $P_0(v)$ replaces $P(v|X=1)$ and $P(v|X=0)$ respectively. In addition, the term

Equation 4 $$D_{Ko} = \sum_{v} \left| P_1(v) - P_0(v) \right|$$

is called the Kolmogrov divergence [Devroye 1998]. Further note that the Kolmogrov divergence can be written as,

Equation 5 $$D_{Ko} = \frac{1}{2} \sum_{v} P(v) \cdot 2 \frac{\left| P_1(v) - P_0(v) \right|}{P_1(v) + P_2(v)},$$

which can be interpreted as the expected value over v of the scaled absolute difference between the two conditional probability distributions. Here, the scaling factor is $\frac{2}{P_1(v) + P_2(v)} = \frac{1}{P(v)}$. Its effect will be explained in the following simple example.

Example: Consider two observed coefficients v_1 and v_2 where the absolute difference between the conditional probability distributions is the same,

$$\left| P_1(v_1) - P_2(v_1) \right| = \left| P_1(v_2) - P_2(v_2) \right|.$$

In addition assume

$$P(v_1) > P(v_2).$$

Therefore, we see that

$$\frac{\left| P_1(v_1) - P_2(v_1) \right|}{P(v_1)} < \frac{\left| P_1(v_2) - P_2(v_2) \right|}{P(v_2)}.$$

This result makes practical sense because even the difference between the conditional distributions is the same at v_1 and v_2, the classification error at v_1 is greater than the one at v_2, i.e.

$$E^*(v_1) > E^*(v_2),$$

where

$$E^*(v) = 1 - \frac{|P_1(v) - P_2(v)|}{P(v)}$$

the Bayesian classification error at *v*. Thus, $\frac{1}{P(v)}$ augments the difference between the conditional distributions according to the classification error.

The above assertion assumes the conditional probabilities $P_1(v)$ and $P_2(v)$ are known *a priori*, in which case the Kolmogrov divergence D_{Ko} as well as the classification E^* can be computed exactly. In practice however, one must estimate the conditional probabilities from the observed training data. When the training data samples are limited, the above calculation breaks down considerably. Consider the following simple case in which *v* takes value *1* or *0* only, and the true conditional probabilities are

$$\begin{aligned} P(v=1 \mid X_1) &= \alpha, \quad & P(v=0 \mid X_1) &= 1-\alpha \\ P(v=1 \mid X_2) &= \beta, \quad & P(v=0 \mid X_2) &= 1-\beta \end{aligned}.$$

Therefore, for a training sample of size *N*, the probability of observing n_1 *1*'s given class X_1 is

$$P(S = n_1 \mid X_1) = \binom{N}{n_1} \alpha^{n_1} (1-\alpha)^{N-n_1},$$

and similarly the probability of observing n_2 *1*'s given class X_2 is

$$P(S = n_2 \mid X_2) = \binom{N}{n_2} \beta^{n_2} (1-\beta)^{N-n_2},$$

where S is a random variable such that

$$S = \sum_{i=1}^{N} v_i .$$

In addition, if we estimate the conditional probabilities using the histogram rule, i.e.

$$\begin{aligned} \hat{P}(v=1\,|\,X_1) &= \frac{n_1}{N}, \qquad \hat{P}(v=0\,|\,X_1) = 1-\frac{n_1}{N} \\ \hat{P}(v=1\,|\,X_2) &= \frac{n_2}{N}, \qquad \hat{P}(v=0\,|\,X_2) = 1-\frac{n_2}{N} \end{aligned},$$

then the probability of obtaining these estimation becomes

$$P(\hat{P}_1(1)=\frac{n_1}{N}) = P(\hat{P}_1(0)=1-\frac{n_1}{N}) = \binom{N}{n_1}\alpha^{n_1}(1-\alpha)^{N-n_1}$$

and

$$P(\hat{P}_2(1)=\frac{n_2}{N}) = P(\hat{P}_2(0)=1-\frac{n_2}{N}) = \binom{N}{n_2}\beta^{n_2}(1-\beta)^{N-n_2},$$

where $\hat{P}_1$ and $\hat{P}_0$ are two random variables representing the estimated probability $\hat{P}(v\,|\,X_1)$ and $\hat{P}(v\,|\,X_2)$, respectively. Because the above probabilities are nothing more than binomial distributions, the expected value of the estimated probabilities are

$$\begin{aligned} E\left\{\hat{P}_1(1)\right\} &= \alpha, \qquad E\left\{\hat{P}_1(0)\right\} = 1-\alpha \\ E\left\{\hat{P}_2(1)\right\} &= \beta, \qquad E\left\{\hat{P}_2(0)\right\} = 1-\beta \end{aligned},$$

and the variance of the estimated probabilities are

$$\begin{aligned} V\left\{\hat{P}_1(1)\right\} &= \frac{\alpha(1-\alpha)}{N}, \qquad V\left\{\hat{P}_1(0)\right\} = \frac{\alpha(1-\alpha)}{N} \\ V\left\{\hat{P}_2(1)\right\} &= \frac{\beta(1-\beta)}{N}, \qquad V\left\{\hat{P}_2(0)\right\} = \frac{\beta(1-\beta)}{N} \end{aligned}.$$

Consequently, the variances associated with the sums and differences of the conditional distributions are

$$V\left\{\hat{P}_1(1)-\hat{P}_2(1)\right\}=\frac{\alpha(1-\alpha)}{N}+\frac{\beta(1-\beta)}{N}$$
$$V\left\{\hat{P}_1(0)-\hat{P}_2(0)\right\}=\frac{\alpha(1-\alpha)}{N}+\frac{\beta(1-\beta)}{N},$$

and

$$V\left\{\hat{P}_1(1)+\hat{P}_2(1)\right\}=\frac{\alpha(1-\alpha)}{N}+\frac{\beta(1-\beta)}{N}$$
$$V\left\{\hat{P}_1(0)+\hat{P}_2(0)\right\}=\frac{\alpha(1-\alpha)}{N}+\frac{\beta(1-\beta)}{N}.$$

Hence, the term $\frac{P_1(v)-P_0(v)}{P_1(v)+P_2(v)}$ depends on the estimation of the conditional distributions. And this dependence become substantial when $P_1(v)-P_0(v)$ or $P_1(v)+P_0(v)$ approaches 0. In another word, the Kolmogrov discriminability measure, D_{Ko} is overwhelmed by the uncertainty at v if $P_1(v)-P_0(v)\approx 0$ or $P_1(v)+P_0(v)\approx 0$. Therefore, it is essential to trade off the classification performance for robustness against such a finite sample effect.

In order to suppress the finite sample effect, it is necessary to become conservative when interpreting the weighted difference between the conditional probability distributions, namely $\frac{P_1(v)-P_0(v)}{P_1(v)+P_2(v)}$. First revisit the mutual information and manipulate it into the following,

Equation 6

$$I(X;v) = \frac{1}{2}\sum_{v} P_1(v)\log\frac{P_1(v)}{P(v)} + P_2(v)\log\frac{P_2(v)}{P(v)}$$
$$= \frac{1}{2}\sum_{v} P(v)\left[\frac{P_1(v)}{P(v)}\log\frac{P_1(v)}{P(v)} + \frac{P_2(v)}{P(v)}\log\frac{P_2(v)}{P(v)}\right]$$
$$= \frac{1}{2}\sum_{v} P(v)\left[(1+PF(v))\log(1+PF(v)) + (1-PF(v))\log(1-PF(v))\right]$$

where

$$PF(v) = \frac{P_1(v) - P_2(v)}{P_1(v) + P_2(v)},$$

the same term present in Equation 15. We can further compare the two functionals, $F_1(x) = 2|x|$ and $F_2(x) = (1+x)\log(1+x) + (1-x)\log(1-x)$ that appear in Equation 3 and Equation 4. Figure 2 illustrates the two functionals from *[-1 1]*.

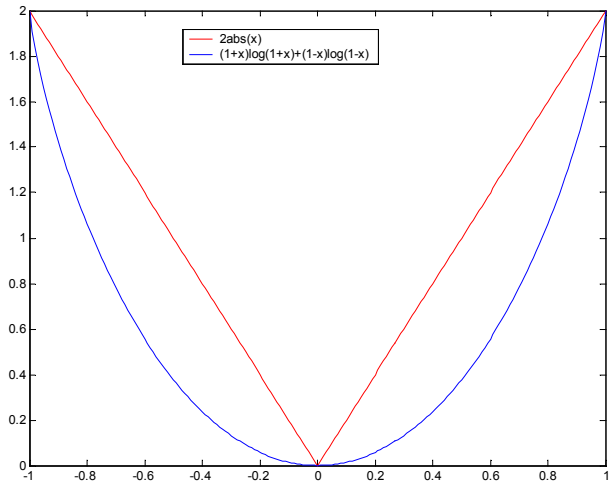

Figure A.0-2 The functionals in Kolmogrov divergence and mutual information

The red curve is F_1 and the blue curve is F_2. Notice the difference between F_1 and F_2 becomes large when approaching *0*. X-axis is the value of *PF* and y-axis marks the value of the Kolmogrov and mutual information functionals.

Compared to F_1, F_2 significantly suppresses the portion of the curve in the vicinity of *0*. Intuitively, this occurs when *PF* is close to 0, where the difference between $P_1(v)$ and

$P_2(v)$ is dominated by the variance of the estimation, an effect of finite training sample. Therefore, using mutual information as the discriminability measure remains conservative when the underlying probability estimation is dominated by uncertainty. By doing so, the finite sample effect is also successfully suppressed. Hence, mutual information effectively trades tightness of the error bound for robustness when dealing with a finite number of samples.